STUDY OF SPIN ORBIT COUPLING IN 2D/3D PEROVSKITES AND ENERGY TRANSFER BETWEEN 3D $MAPbI_3$ PEROVSKITE AND RUBRENE SINGLET FISSION MOLECULES

by

MINH THIEN PHAM

(Under the Direction of THO DUC NGUYEN)

ABSTRACT

Hybrid organic-inorganic perovskites (HOIPs) are rapidly emerging as functional materials for novel optoelectronic and quantum electronic devices. Recently, the power conversion efficiency for a single-junction HOIPs based solar cell having an analog of $MAPbI_3$ (where MA = CH_3NH_3) as the absorber layer exceeded 26%. The high-power conversion efficiency observed for these materials may be related to the degree of spin orbit coupling (SOC) strength present in their crystal structure. It has been hypothesized that the breaking of structural and bulk inversion symmetry in combination with the strong intrinsic spin-orbit coupling (SOC) from heavy Pb atoms in the superlattice gives rise to large Rashba-Dresselhaus SOC, where spin-dependent properties can be manipulated by electric fields.

In this dissertation, I will present my study on Rashba-Dresselhaus SOC in 3D ($MAPbI_3$) and 2D Ruddlesden-Popper perovskite superlattices $(BA)_2MA_{n-1}Pb_nI_{3n+1}$ with n = 1, 2, and 3 (where BA = $CH_3(CH_2)_3NH_3$). I have utilized several experimental techniques to investigate the spin-dependent processes in HOIPs including (i) magnetic field effect

(MFE) in electroluminescence and conductivity of HOIPs-based light emitting diodes (LEDs), where the Rashba-Dresselhaus SOC strengths versus applied electric fields are measured, (ii) circular dichroism (CD) and circularly polarized luminescence (CPL) spectroscopies on HOIP thin films in which the degeneracy lifting of the electronic ground states and excited states by the Rashba-Dresselhaus field can be measured by CD and CPL spectroscopies, respectively. We found that the Rashba-Dresselhaus SOC is very large in 2D Ruddlesden-Popper perovskite $(BA)_2MA_{n-1}Pb_nI_{3n+1}$ when n = 1 and n = 2 and monotonically decreases as n increases. (iii) Finally, I will study and elucidate the energy transfer and energy upconversion processes between the $MAPbI_3$ perovskite and rubrene singlet fission molecules $C_{42}H_{28}$ by the magnetic field effect on photoluminescence (MPL). Our studies may have a significant impact on future development of electrically-controlled spin logic devices via Rashba-Dresselhaus effects and high-performance solar cells.

INDEX WORDS: spin orbit coupling, 2D perovskites, 3D perovskites, light emitting diodes, circular dichroism, circularly polarized dichroism, magnetic circular dichroism, Faraday rotation, energy transfer, singlet fission, solar cell.

STUDY OF SPIN ORBIT COUPLING IN 2D/3D PEROVSKITES AND ENERGY TRANSFER BETWEEN 3D $MAPbI_3$ PEROVSKITE AND RUBRENE SINGLET FISSION MOLECULES

by

MINH THIEN PHAM

BS, Hanoi University of Science and Technology, Vietnam, 2012

MS, Chonnam National University, Republic of Korea, 2015

A Dissertation Submitted to the Graduate Faculty of The University of Georgia in Partial Fulfillment of the Requirements for the Degree

DOCTOR OF PHILOSOPHY

ATHENS, GEORGIA

2021

STUDY OF SPIN ORBIT COUPLING IN 2D/3D PEROVSKITES AND ENERGY TRANSFER BETWEEN 3D $MAPbI_3$ PEROVSKITE AND RUBRENE SINGLET FISSION MOLECULES

by

MINH THIEN PHAM

Major Professor:	Tho Duc Nguyen
Committee:	Susanne Ullrich
	Lawrence Hornak
	Yohannes Abate

Electronic Version Approved:

Ron Walcott
Vice Provost for Graduate Education and Dean of the Graduate School
The University of Georgia
May 2021

This dissertation is dedicated to my grandfather

ACKNOWLEDGEMENTS

First of all, I would like to thank my advisor, Prof. Tho Duc Nguyen for his guidance and continued support throughout my PhD research. Thank you for giving me opportunity to join your research group, and for teaching and mentoring me throughout many challenges and difficulties. There are no words that can fully express my gratitude and admiration.

I would like to thank all members of my thesis defense and dissertation committee, Prof. Susanne Ullrich, Prof. Lawrence Hornak, and Prof. Yohannes Abate, for spending their precious time and effort on my Ph.D. defense and dissertation.

Additionally, I would like to thank my past and present lab-mates and collaborators for their help and for supporting my studies and research. Thank you, Prof. Manh-Huong Phan (University of South Florida), for introducing me to Prof. Tho Nguyen. Thank you Rugang and Hoang for training me in the experimental skills. Thank you, Eric, Kameron and Luisa for providing me the high-quality perovskites materials for the last 4 years. Thank you, Lenny, Prof. Ullrich, and Prof. Thang Hoang, for helping with transient spectroscopy, and Dr. Huan Tran from Georgia Tech and Prof. Tuoc Vu from Hanoi University of Science and Technology for DFT calculations and insightful discussions. And thank you all, Terry Phang, Marshall Liss, Jie Zhan, and Tu Anh for your help.

Finally, I would like to say thank to my parents, my sister, and my friends, who have always supported me unconditionally and encouraged me to follow the career path I chose.

TABLE OF CONTENTS

Page

LIST OF TABLES

Page

LIST OF FIGURES

Page

CHAPTER 1

INTRODUCTION TO PEROVSKITE MATERIALS

In this first chapter, I will present the general information and properties of the 3D $MAPbI_3$ and 2D Ruddlesden-Popper perovskites. Fundamentals of spin-orbit coupling and Rashba-Dresselhaus spin-orbit coupling are also reviewed.

1.1 HYBRID ORGANIC INORGANIC PEROVSKITE

Perovskite is a calcium titanium oxide mineral ($CaTiO_3$), which was discovered by Gustav Rose in 1839. It was named after Russian mineralogist Lev Perovski (1792-1856). After that, the term "perovskite" has also been used for to denote a class of compounds which have the same type of crystal structure as calcium titanium oxide. The perovskite compound has the general chemical formula of ABX_3 where A and B are two cations and X is an anion that bonds to both cations. In hybrid organic inorganic perovskites (HOIPs), A is an organic cation, B is a metal cation and X is halide anion. HOIPs such as $MAPbX_3$ ($MA = CH_3NH_3$, X = Cl, Br, and I) and $MASnBr_xI_{3-x}$ were first synthesized and characterized in the 1980s[5], but they have become a very hot research topic for the last 10 years. A study in Materials journal reported that the number of publications on perovskites in 2018 has reached 8000 papers.[6] This means that there are more than 20 papers on perovskites published every single day! HOIPs have shown that they are great materials for photovoltaic, optoelectronic and electronic applications including solar cell, light emitting diode[7], laser[6] and spintronics devices[8]. However, most of the research on HOIPs focuses on solar cell applications. The first perovskite based solar cells using

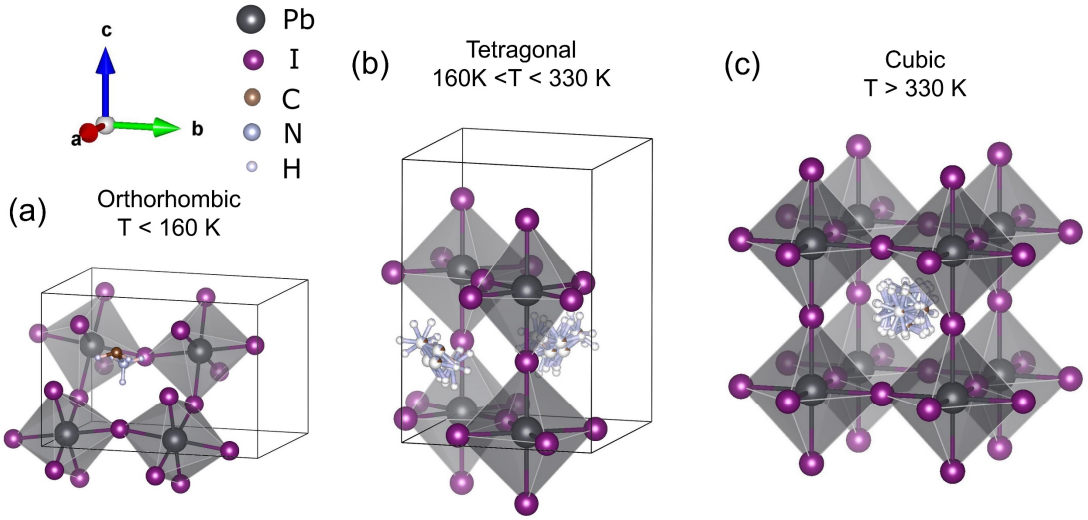

Figure 1.1. Crystal structural phases of $MAPbI_3$. (a) orthorhombic phase when T < 160 K, (b) tetragonal phase when 160K < T < 330 K, and (c) cubic phase when T > 330 K.

$CH_3NH_3PbBr_3$ and $CH_3NH_3PbI_3$ were fabricated in 2009 with a power conversion efficiency of 3.8%[9], but it quickly passed other kinds of solar cells in the race for high power conversion efficiency (PCE). In 2015 the PCE of perovskite solar cell reached 20% and the PCE of 26% was reported in 2021[10]. For a comparison, the amorphous silicon based solar cell has a theoretical limit of efficiency of 15%.[11] The commercial amorphous silicon based solar cell has an efficiency of 6 to 7%. HOIPs such as $CH_3NH_3PbBr_3$ and $CH_3NH_3PbI_3$ possess desired properties as excellent candidates for solar cells due to the following reasons. First, they have large absorption coefficient, and the absorption spectrum of perovskite is very broad, from 350 nm up to 800 nm.[12] Second, perovskite is easily fabricated; one can simply fabricate a perovskite thin film by solution processes. The solution can be readily prepared by mixing the precursors in an appropriate solvent. This leads to another reason that perovskites are well-suited to solar cells: the perovskite based solar cell is cheap, and any technology which is cost-efficient would be attractive and

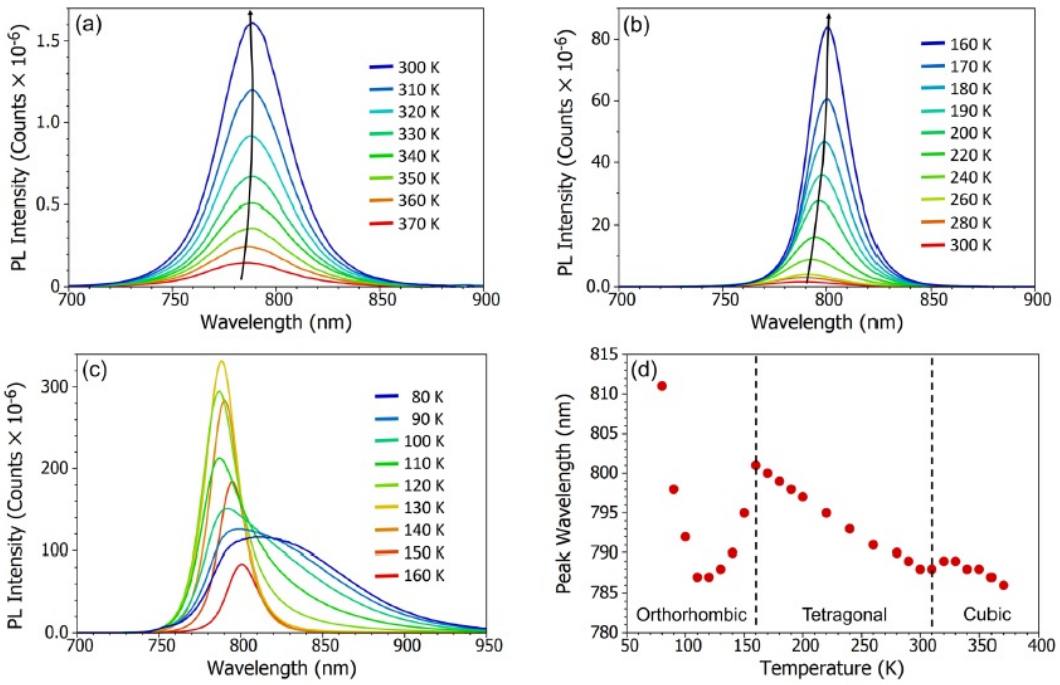

Figure 1.2. Photoluminescence (PL) spectrum of $MAPbI_3$ with temperature (a) PL spectrum over 370 to 300K, (b) PL spectrum over 300K to 160K, (c) PL spectrum over 160K to 80K and (d) the variation of peak wavelength of the PL emission with temperature (λ_{ex} = 400 nm). The black arrow in (a) and (b) illustrate the shift in peak wavelength with temperature. Graph is adopted from ref.[1]

promising. The most interesting property of perovskite is that the carrier lifetime[13] and diffusion length[14] are very long . In single crystal perovskite, the lifetime of a carrier can be up to ten microseconds, and the diffusion length can be up to 175 μm under full light illumination and 3 mm under low light illumination.[15] Thanks to this extremely long diffusion length, a thicker layer of perovskite material, up to 500 nm, can be utilized. Therefore, the sun light is more efficiently absorbed. HOIPs also has strong spin-orbit coupling (SOC) due to the heavy atoms in its chemical formula, for example, lead (Pb). The high power conversion efficiency observed for HOIPs may be related to the degree of

SOC strength.[16] One of the most studied hybrid perovskite materials is $CH_3NH_3PbI_3$ ($MAPbI_3$, or MAPI) where the organic cation is methylammonium (CH_3NH_3 - MA), the metal cation is lead (Pb) and the anion is Iodine (I). MAPI has three crystal structural phases, including cubic structure with a space group of *Pm-3m* when temperature is from 330 K or higher, a tetragonal *I4/mcm* phase when the temperature is from 160 K to 330 K, and an orthorhombic *Pnma* phase when temperature is below 160 K.[16-17] All the crystal structures and photoluminescence spectra of MAPI corresponding to different phases are illustrated in **Figure 1.1** and **Figure 1.2**, respectively.

1.2 2D RUDDLESDEN-POPPER HYBRID LEAD IODIDE PEROVSKITE

Recently, a new class of HOIPs, which is 2-dimensional (2D) Ruddlesden-Popper perovskite has emerged and attracted attention from research community.[18-21] 2D Ruddlesden-Popper perovskites are considered as excellent materials for optoelectronics devices thanks to desired properties such as: large exciton binding energy, strong quantum confinement effect, and superior stability to moisture compared to 3D perovskites[20, 22]. 2D Ruddlesden-Popper perovskites are formed by splitting along lattice orientation <001> and <110> from 3D perovskite. The general chemical formula of Ruddlesden-Popper perovskites is $(A')_2(A)_{n-1}B_nX_{3n+1}$ where A' is R-NH_3 or H_3N-R-NH_3. R is a large aliphatic alkyl chain or an aromatic ligand and is the organic layer that isolate the inorganic layers that composed of metal halide octahedral units.[23] A is small cation, can be MA (CH_3NH_3), B is divalent metal cation, and X is referred to halides. The number of perovskite layers that are sandwiched between organic chains n can be adjusted by the ratio between precursors in synthesis process. Due to the different of refractive index between the organic chain (~1.5) and the perovskite layers (~2.3)[22], these materials are indeed hybrid quantum

well systems, where the width of the quantum well can be changed by changing the number of perovskite layers n.[22] Therefore, the value of n, especially when n is small, determines the crystal structure and optical properties of 2D Ruddlesden-Popper perovskites, such as bandgap tunability and broadband emission wavelength. In this dissertation, the 2D Ruddlesden-Popper perovskite studied is $(BA)_2(MA)_{n-1}Pb_nI_{3n+1}$ where A' is butylammonium BA $CH_3(CH_2)_3NH_3$, A is methylammonium CH_3NH_3. (**Figure 1.3**)

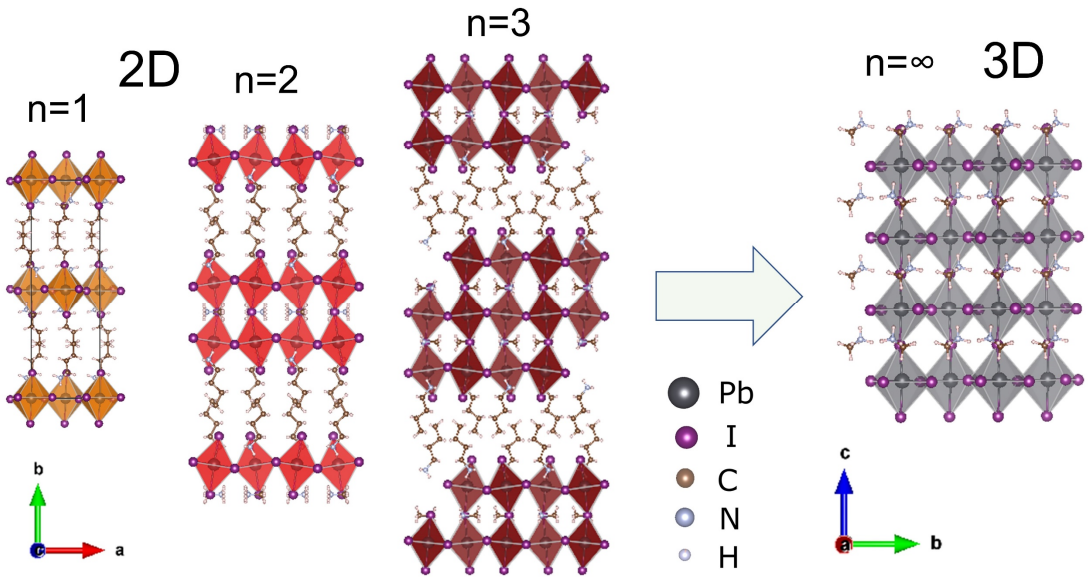

Figure 1.3. Representation of the crystal structure at room temperature of 2D Ruddlesden-Popper perovskites $(BA)_2MAPb_nI_{3n+1}$ and 3D perovskite $MAPbI_3$.

The 2D Ruddlesden-Popper perovskites are also an excellent material for solar cell applications. Even though the efficiency is lower than that of the 3D perovskite, it is attracting a lot of attention from research community due to its excellent stability in humidity. Tsai et. al' s work on Nature is one of the earliest works on 2D Ruddlesden-Popper perovskite solar cell.[18] The authors have shown that using the 2D Ruddlesden-Popper perovskite $(BA)_2(MA)_{n-1}Pb_nI_{3n+1}$ with n = 3 and n = 4, they could achieve a solar

cell with PCE up to 12.52%, and the cells showed a significant improvement in stability when subjected to light, humidity and heat in comparison to 3D perovskite solar cells.[18] Very recently, Liang and co-workers presents another improvement when they use the 2D Ruddlesden-Popper phase-pure quantum wells (QWs) instead of the multi quantum wells perovskite. The cell using pure phase QWs show a PCE greater than 16%, a high open circuit voltage of 1.31 V. The cell showed less than 10% efficiency degradation after being kept under humidity of 65 ± 10%, or after working at 85° C for 558 hours, or under continuous light illumination for 1100 hours.[24]

The 3D MAPI and 2D Ruddlesden-Popper $(BA)_2(MA)_{n-1}Pb_nI_{3n+1}$ perovskites were fabricated by my collaborator, Dr. Eric Amerling (Department of Chemistry, the University of Utah). The perovskite crystals were then kept inside nitrogen gas-filled vials to prevent material degradation. X-ray diffraction (XRD), absorption and photoluminescence spectroscopies were taken and compared between the films fabricated in 2 laboratories to make sure the quality of materials are the same. Details of the 3D MAPI and 2D Ruddlesden-Popper perovskites fabrication processes and characterization are described in **Appendix A**.

1.3 RASHBA-DRESSELHAUS SPIN-ORBIT COUPLING

1.3.1 SPIN-ORBIT COUPLING

An interesting and fundamental question that has puzzled perovskite's researchers is why HOIPs (both 3D and 2D Ruddlesden-Popper perovskites) are excellent materials for solar cell. More specifically, why do HOIPs have large absorption range and a small recombination rate, and why are the diffusion length and lifetime of carriers so long?

There is a leading hypothesis for the answer: the Rashba effect makes the band gap indirect and slows down carrier recombination rate.[25-26] There are many studies of Rashba SOC in 3D perovskites suggesting that strong Rashba SOC exists in 3D perovskite and 2D Ruddlesden-Popper perovskites.[25, 27-28] We will talk in more detail about this in the next section. Now, let me first provide some essential knowledge of spin-orbit coupling.

Spin is an intrinsic angular momentum of elementary particles. An electron has spin $\vec{S}$ that has a value of either 1/2 or -1/2, and a magnetic moment $\overrightarrow{\mu_S}$ = $-g.\mu_B.\vec{S}/\hbar$ where g is electron g factor, μ_B is the Bohr Magneton, and $\hbar$ is the Planck constant.

When an electron orbits around the nucleus of an atom one can consider that electron is stationary and the nucleus is orbiting around it from a relativistic perspective, as depicted in **Figure 1.4**. The nucleus includes Z protons, so it has electric charge $+Ze$ and creates an effective magnetic field at the electron's location. Under a magnetic field, the

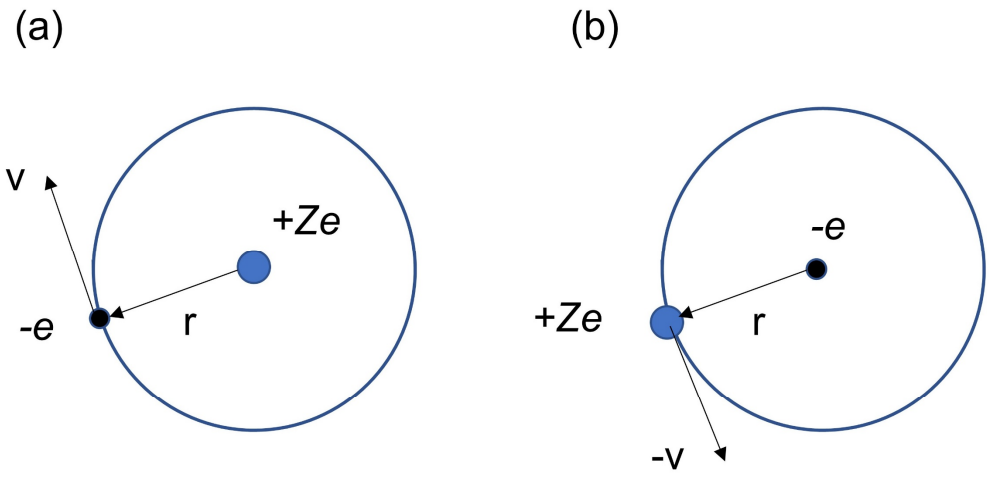

Figure 1.4. Representation of spin-orbit coupling. (a) electron is orbiting around atom's nucleus with the velocity v in the lab frame. (b) in the electron frame, the nucleus is orbiting around electron with the velocity -v.

electron spin has potential energy, which is the energy of the interaction. The interaction can be described by the Hamiltonian:

$$H_{SOC} = b\vec{L} \cdot \vec{S} \qquad (1.1)$$

Where $\vec{L}$ is the orbital angular momentum operator, $\vec{S}$ is the electron spin operator, and b is the coupling constant. This phenomenon is detectable as a splitting of spectral lines, which can be thought as a Zeeman effect when considering electron spin angular momentum $\vec{S}$ under the effective magnetic field B. Indeed, the existence of electron spin actually was postulated by Goudsmit and Uhlenbeck in 1925 based on the observation of splitting of spectral lines in the alkali elements (fine structure).[29]

Equation (1.1) can be simply derived from semi-classical electrodynamics. Details can be found from modern physics textbook, e.g. Fundamental of Modern Physics by Robert Eisberg (1961).

The charged nucleus moving with velocity $-\vec{\mathbf{v}}$ constitutes a current element:

$$\vec{\mathbf{j}} = -Ze\vec{\mathbf{v}}/c$$

This current produces a magnetic field, at the position of the electron, which is given by:

$$\vec{\mathbf{H}} = \frac{\vec{\mathbf{j}} \times \vec{\mathbf{r}}}{r^3} = -\frac{Ze}{c}\frac{\vec{\mathbf{v}} \times \vec{\mathbf{r}}}{r^3}$$

According to Coulomb's law:

$$\vec{\mathbf{E}} = +Ze\frac{\vec{r}}{r^3}$$

From these two equations, we have:

$$\vec{\mathbf{H}} = \frac{-1}{c}\vec{\mathbf{v}} \times \vec{\mathbf{E}}$$

And the magnetic field will cause a Larmor precession of the spin magnetic moment with angular frequency:

$$\overrightarrow{\boldsymbol{\omega}_{\mathbf{L}}} = \frac{g_s \mu_B}{\hbar} \overrightarrow{\mathbf{H}}$$

The magnetic field will produce a potential energy:

$$\Delta E = -\overrightarrow{\boldsymbol{\mu}_{\mathbf{s}}} \cdot \overrightarrow{\mathbf{H}} = \frac{g_s \mu_B}{\hbar} \vec{\mathbf{S}} \cdot \overrightarrow{\mathbf{H}}$$

Both of these quantities are evaluated in a frame of reference in which the electron is at rest, but what we are really interested in is these values in the normal frame in which the nucleus is at rest. When transforming back to the normal frame, these values change due to the kinematic effect from relativity theory. The change of the precession frequency was first discovered by Thomas in 1926, and is called Thomas precession[30].

$$\overrightarrow{\boldsymbol{\omega}_{\mathbf{T}}} = \frac{e}{2mc^2} \vec{\mathbf{v}} \times \vec{\mathbf{E}}$$

The precession frequency in the normal frame is:

$$\overrightarrow{\boldsymbol{\omega}} = -\frac{e}{mc^2} \vec{\mathbf{v}} \times \vec{\mathbf{E}} + \frac{e}{2mc^2} \vec{\mathbf{v}} \times \vec{\mathbf{E}} = -\frac{e}{2mc^2} \vec{\mathbf{v}} \times \vec{\mathbf{E}}$$

We see that the spin precession frequency is reduced by a factor of 2 when transforming from the frame in which the electron is at rest to the normal frame in which the nucleus is at rest. The potential energy, when transformed back to normal frame is also reduced by a factor of 2:

$$\Delta E_{S \cdot L} = \frac{1}{2} \frac{g_s \mu_B}{\hbar} \vec{\mathbf{S}} \cdot \overrightarrow{\mathbf{H}}$$

We can express this term of the quantity $\vec{\mathbf{S}} \cdot \vec{\mathbf{L}}$. Since

$$\overrightarrow{\mathbf{H}} = \frac{-1}{c} \vec{\mathbf{v}} \times \vec{\mathbf{E}}$$

$$-e\vec{\mathbf{E}} = \vec{\mathbf{F}}$$

Where $\vec{\mathbf{F}}$ is the force acting on the electron:

$$\vec{\mathbf{F}} = -\frac{dV(r)}{dr} \frac{\vec{\mathbf{r}}}{r}$$

Putting the equations together, we have:

$$\vec{\mathbf{H}} = -\frac{1}{ec}\frac{1}{r}\frac{dV(r)}{dr}\vec{\mathbf{v}} \times \vec{\mathbf{r}}$$

Then

$$\vec{\mathbf{H}} = \frac{1}{emc}\frac{1}{r}\frac{dV(r)}{dr}\vec{\mathbf{L}}$$

Thus, the potential energy is:

$$\Delta E_{\mathbf{S}\cdot\mathbf{L}} = \frac{g_s \mu_B}{2emc\hbar}\frac{1}{r}\frac{dV(r)}{dr}\vec{\mathbf{S}} \cdot \vec{\mathbf{L}}$$

Or,

$$\Delta E_{\mathbf{S}\cdot\mathbf{L}} = \frac{1}{2m^2c^2}\frac{1}{r}\frac{dV(r)}{dr}\vec{\mathbf{S}} \cdot \vec{\mathbf{L}}$$

Although this derivation of the spin-orbit energy is based on the Bohr theory, the result is exact in agreement with the result from relativistic quantum mechanical treatment.

In the absence of spin-orbit coupling and magnetic field, the magnitudes and z component of the spin and the orbital angular momentum $\vec{\mathbf{S}}$ and $\vec{\mathbf{L}}$ would have fixed values, determined by the quantum numbers l, m_l, and m_s. However, there is a strong magnetic field $\vec{\mathbf{H}}$ whose orientation is determined by $\vec{\mathbf{L}}$ that produces a torque on the electron spin $\vec{\mathbf{S}}$. Torque does not change the magnitude of $\vec{\mathbf{S}}$ and $\vec{\mathbf{L}}$ but it provides a coupling between them, which makes the orientation of each vector dependent on the orientation of the other. Both of the vectors $\vec{\mathbf{S}}$ and $\vec{\mathbf{L}}$ will precess about the *total angular momentum vector* $\vec{\mathbf{J}} = \vec{\mathbf{L}} + \vec{\mathbf{S}}$. Let us evaluate the spin-orbit coupling energy $\Delta E_{\mathbf{S}\cdot\mathbf{L}}$

The expectation value of $\Delta E_{\mathbf{S}\cdot\mathbf{L}}$ can be calculated from the equation:

$$< \Delta E_{\mathbf{S}\cdot\mathbf{L}} >= \iiint \psi^*_{nljm_j}\, \widehat{\Delta E_{\mathbf{S}\cdot\mathbf{L}}}\, \psi_{nljm_j}\, r^2\, sin\theta dr d\theta d\varphi$$

Or

$$< \Delta E_{\mathbf{S\cdot L}} >= \iiint \psi^*_{nljm_j} \left(\frac{1}{2m^2c^2} \frac{1}{r} \frac{dV(r)}{dr} \vec{\mathbf{S}} \cdot \vec{\mathbf{L}} \right) \psi_{nljm_j} r^2 \sin\theta dr d\theta d\varphi$$

For Coulomb potential $V(r) = -Ze^2/r$, so $dV(r)/dr = Ze^2/r^2$ and the equation becomes:

$$< \Delta E_{\mathbf{S\cdot L}} >= \frac{Ze^2}{2m^2c^2} \iiint \psi^*_{nljm_j} \frac{1}{r^3} (\vec{\mathbf{S}} \cdot \vec{\mathbf{L}}) \psi_{nljm_j} r^2 \sin\theta dr d\theta d\varphi$$

We have: $\vec{\mathbf{J}} = \vec{\mathbf{L}} + \vec{\mathbf{S}}$

$$\vec{\mathbf{J}} \cdot \vec{\mathbf{J}} = (\vec{\mathbf{L}} + \vec{\mathbf{S}}) \cdot (\vec{\mathbf{L}} + \vec{\mathbf{S}})$$

So

$$\vec{\mathbf{J}} \cdot \vec{\mathbf{J}} = (\vec{\mathbf{L}} \cdot \vec{\mathbf{L}} + \vec{\mathbf{S}} \cdot \vec{\mathbf{S}} + \mathbf{2}\vec{\mathbf{S}} \cdot \mathbf{L})$$

Therefore,

$$\vec{\mathbf{S}} \cdot \vec{\mathbf{L}} = \frac{1}{2} (\vec{\mathbf{J}} \cdot \vec{\mathbf{J}} - \vec{\mathbf{L}} \cdot \vec{\mathbf{L}} - \vec{\mathbf{S}} \cdot \vec{\mathbf{S}})$$

Or

$$\vec{\mathbf{S}} \cdot \vec{\mathbf{L}} = \tfrac{1}{2} (\boldsymbol{J^2} - \boldsymbol{L^2} - \boldsymbol{S^2}) \qquad (1.2)$$

Putting $\vec{\mathbf{S}} \cdot \vec{\mathbf{L}}$ back into equation (1.2), then we obtain:

$$< \Delta E_{\mathbf{S\cdot L}} >= \frac{Ze^2}{4m^2c^2} \iiint \psi^*_{nljm_j} \frac{1}{r^3} (\boldsymbol{J^2} - \boldsymbol{L^2} - \boldsymbol{S^2}) \psi_{nljm_j} r^2 \sin\theta dr d\theta d\varphi \qquad (1.3)$$

$\psi^*_{nljm_j}$ is an eigenfunction of $\boldsymbol{J^2}$, $\boldsymbol{L^2}$, and $\boldsymbol{S^2}$ operators, with the eigenvalues $j(j+1)\hbar^2$, $l(l+1)\hbar^2$ and $\frac{1}{2}(\frac{1}{2}+1)\hbar^2$.

We have

$$(\boldsymbol{J^2} - \boldsymbol{L^2} - \boldsymbol{S^2}) \psi_{nljm_j} = [j(j+1) - l(l+1) - ¾\,]\, \hbar^2 \psi_{nljm_j}$$

Then we only have to evaluate the integral

$$\iiint \psi^*_{nljm_j} \frac{1}{r^3} \psi_{nljm_j} r^2 \sin\theta dr d\theta d\varphi$$

The integral over θ and φ both give unity because of the normalization property of the eigenvalue ψ_{nljm_j}. The integral over *r* can be evaluated:

$$\int R_{nl}^{*}(r)\frac{1}{r^3}R_{nl}(r)r^2dr \; = <\frac{1}{r^3}> = \frac{Z^3}{a_0^3 n^3 l(l+\frac{1}{2})(l+1)}$$

Plugging the result back into equation (1.3), we obtain the expectation value of spin-orbit coupling energy:

$$< \Delta E_{\mathbf{S}\cdot\mathbf{L}} > = \frac{Z^4 e^2 \hbar^2}{4m^2c^2a_0^3}\frac{[j(j+1) \; - \; l(l+1) - \frac{3}{4}]}{n^3 l(l+\frac{1}{2})(l+1)}$$

The strength of spin-orbit coupling is theoretically proportional to Z^4. However, in reality, due to shielding effect in atom, the experimental results prove the exponent is from 2-4[31]. Spin orbit coupling becomes large and is an important interaction when the atomic number Z becomes large. SOC energy also can be written in terms of the fine structure constant $\alpha \equiv e^2/\hbar c \approx 1/137$ and the unperturbed energy of the states $E_n = \frac{-mZ^2e^4}{2\hbar^2 n^2}$

$$< \Delta E_{\mathbf{S}\cdot\mathbf{L}} > = \frac{Z^2|E_n|\alpha^2}{2n}\frac{[j(j+1) \; - \; l(l+1) - \frac{3}{4}]}{l(l+\frac{1}{2})(l+1)}$$

There is another important interaction in the atom, which is Hyperfine Interaction (HFI). Hyperfine interaction is the dipole-dipole interaction between magnetic moments of nucleus and electron's magnetic moment, or simply the interaction between electron spin and the nuclear spin. Since the electron can interact with more than one nucleus, the HFI can be described by the Hamiltonian:

$$H_{HFI} = \sum_{i}^{N} A_i \vec{I}_i \cdot \vec{S}$$

Where I is the nucleus spin operator, S is the electron spin operator, and A_i is the coupling constant. When an electron interacts with N nuclei spins, the effective HFI strength can be rewritten as $H_{HFI} = a\vec{I} \cdot \vec{S}$, where a is the effective coupling constant describes by $a \sim A/\sqrt{N}$. The more nuclei the electron interacts with, or the more delocalization of electron's wavefunction, the weaker the HFI is.[32-33]

The fine structure splitting in atom spectrum is corresponding to spin orbit coupling, can be larger up to hundreds of milli electron volts, whereas the hyperfine structure splitting corresponding to HFI is 1 to 2 orders smaller.

1.3.2 RASHBA-DRESSELHAUS SPIN-ORBIT COUPLING

Note that in the intrinsic SOC that we just discussed above, the electric field originates from the gradient of potential energy from the nucleus. But the electric field that induces the effective magnetic field can come from other sources.

Dresselhaus was the first to propose the hypothesis that, in zinc-blende III–V semiconductor compounds such as GaAs or InSb, there is a crystal electric field.[34] This electric field is induced from *Bulk Inversion Asymmetry* (BIA) in the compounds whose crystals lack a center of inversion. Later, Bychkov and Rashba found that the interfacial electric field at the surface or interface of heterostructure also resulted in a SOC[35] induced from *Structure Inversion Asymmetry* (SIA). In bulk semiconductor, the Rashba-Dresselhaus SOC removes the electron spin degeneracy and splits each of the valence and conduction band edge, resulting in an indirect bandgap.[36-37]

Let us study the effect of Rashba-Dresselhaus SOC on the energy band diagram of semiconductor.

The spin degeneracy of electron and hole states in semiconductors is the combined effect from inversion symmetry in space and time. Both symmetry operators change the wave vector $\vec{\boldsymbol{k}}$ into $-\vec{\boldsymbol{k}}$, but time inversion also flips the spin. This results in a twofold degeneracy $E_+(\vec{\boldsymbol{k}}) = E_-(\vec{\boldsymbol{k}})$. When an electron or hole moves under an inversion-asymmetric potential, the spin degeneracy is removed. Therefore, the energy dispersion is split into two branches $E_+(\vec{\boldsymbol{k}})$ and $E_-(\vec{\boldsymbol{k}})$. In quasi-2D quantum wells and heterostructures, the spin splitting can be the results of a BIA, or of a structure inversion asymmetry (SIA). For simplicity, let us consider the effect of Rashba SOC:

The Rashba Hamiltonian is given by[35] :

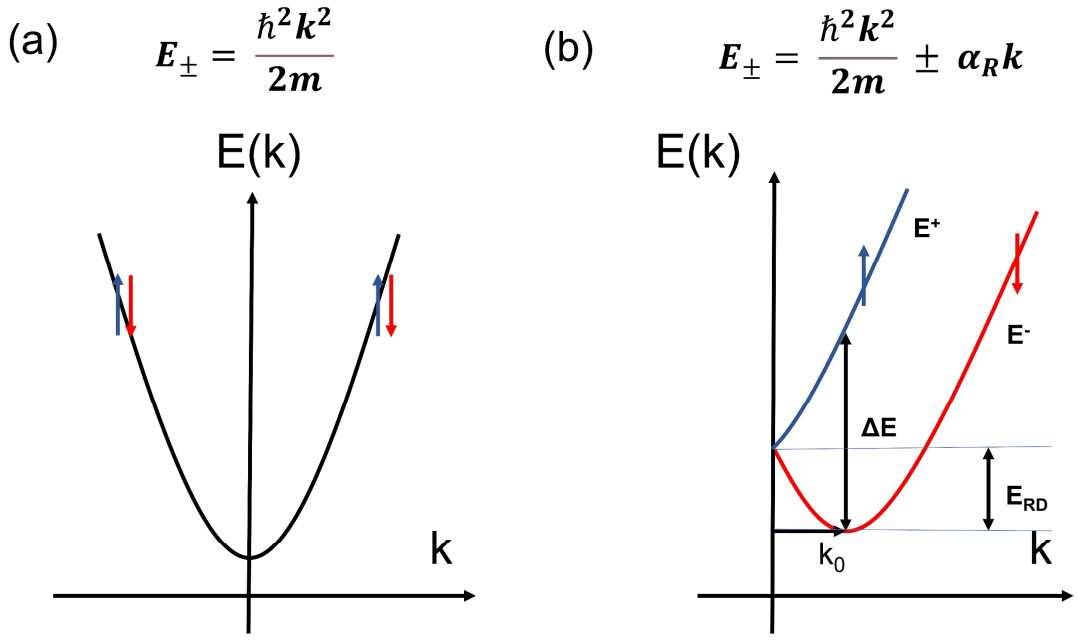

Figure 1.5. (a) schematic representation of two-fold spin degeneration electronic band in semiconductor. (b) spin-polarized sub-bands separated in k-space due to Rashba-Dressealhaus SOC. ΔE denotes the energy difference between 2 branches at the characteristic momentum k0 and ERD is the Rashba-Dresselhaus energy.

$$\widehat{H}_{SOC} = \alpha_R \, \vec{\boldsymbol{n}} \cdot (\widehat{\boldsymbol{\sigma}} \times \widehat{\boldsymbol{k}}) = \alpha_R (k_y \sigma_x - k_x \sigma_y)$$

Where $\vec{\boldsymbol{n}}$ is the unit vector along the *z*-axis.

The Pauli matrices:

$$\sigma_x = \begin{pmatrix} 0 & 1 \\ 1 & 0 \end{pmatrix}, \sigma_y = \begin{pmatrix} 0 & -i \\ i & 0 \end{pmatrix}, \sigma_z = \begin{pmatrix} 1 & 0 \\ 0 & -1 \end{pmatrix}$$

Then $\widehat{H}_{SOC}$ can be expressed as:

$$\widehat{H}_{SOC} = \alpha_R \begin{pmatrix} 0 & -i(k_x + ik_y) \\ i(k_x - ik_y) & 0 \end{pmatrix}$$

$k_x = k cos\theta$, $k_y = k sin\theta$

So

$$k_x + ik_y = k(cos\theta + isin\theta) = ke^{i\theta}$$

$$k_x - ik_y = k(cos\theta - isin\theta) = ke^{-i\theta}$$

It leads to: $\widehat{H}_{SOC} = \alpha_R k \begin{pmatrix} 0 & -ie^{i\theta} \\ ie^{-i\theta} & 0 \end{pmatrix}$

Let $|\psi_1\rangle$ and $|\psi_2\rangle$ be the eigenkets of $\widehat{H}_{SOC}$

Solving the problem, we have the eigenkets:

$|\psi_1\rangle = \frac{1}{\sqrt{2}} \begin{pmatrix} 1 \\ ie^{-i\theta} \end{pmatrix}$ with eigenvalue $\alpha_R k$ and $|\psi_2\rangle = \frac{1}{\sqrt{2}} \begin{pmatrix} 1 \\ -ie^{-i\theta} \end{pmatrix}$ with eigenvalue -$\alpha_R k$.

$$\widehat{H}_{SOC}|\psi_1\rangle = \alpha_R k \begin{pmatrix} 0 & -ie^{i\theta} \\ ie^{-i\theta} & 0 \end{pmatrix} |\psi_1\rangle = \alpha_R k \begin{pmatrix} 0 & -ie^{i\theta} \\ ie^{-i\theta} & 0 \end{pmatrix} \frac{1}{\sqrt{2}} \begin{pmatrix} 1 \\ ie^{-i\theta} \end{pmatrix}$$

$\widehat{H}_{SOC}|\psi_1\rangle = \frac{\alpha_R k}{\sqrt{2}} \begin{pmatrix} -i^2 \\ ie^{-i\theta} \end{pmatrix} = \frac{\alpha_R k}{\sqrt{2}} \begin{pmatrix} 1 \\ ie^{-i\theta} \end{pmatrix} = \alpha_R k|\psi_1\rangle$

Similarly, $\widehat{H}_{SOC}|\psi_2\rangle = -\alpha_R k|\psi_2\rangle$

$\widehat{H}_0$ is the Hamiltonian of free electron:

$$\widehat{H}_0 = \frac{\hbar^2 k^2}{2m} \begin{pmatrix} 1 & 0 \\ 0 & 1 \end{pmatrix}$$

We see that $|\psi_1\rangle$ and $|\psi_2\rangle$ are also the eigenkets of $\hat{H}_0$:

$$\hat{H}_0|\psi_1\rangle = \frac{\hbar^2k^2}{2m}\begin{pmatrix}1 & 0\\ 0 & 1\end{pmatrix}|\psi_1\rangle = \frac{\hbar^2k^2}{2m}|\psi_1\rangle$$

And

$$\hat{H}_0|\psi_2\rangle = \frac{\hbar^2k^2}{2m}\begin{pmatrix}1 & 0\\ 0 & 1\end{pmatrix}|\psi_2\rangle = \frac{\hbar^2k^2}{2m}|\psi_2\rangle$$

Note that $[\hat{H}_0, \hat{H}_{SOC}] = 0$, so $|\psi_1\rangle$ and $|\psi_2\rangle$ are eigenkets of $\hat{H} = \hat{H}_0 + \hat{H}_{SOC}$

$$\hat{H}|\psi_1\rangle = (\hat{H}_0 + \hat{H}_{SOC})|\psi_1\rangle = (\frac{\hbar^2k^2}{2m}|\psi_1\rangle + \alpha_R k|\psi_1\rangle) = (\frac{\hbar^2k^2}{2m} + \alpha_R k)|\psi_1\rangle$$

$$\hat{H}|\psi_2\rangle = (\hat{H}_0 + \hat{H}_{SOC})|\psi_2\rangle = (\frac{\hbar^2k^2}{2m}|\psi_2\rangle + \alpha_R k|\psi_2\rangle) = (\frac{\hbar^2k^2}{2m} - \alpha_R k)|\psi_2\rangle$$

From these equations, we see that the eigenvalues are $E_\pm = \frac{\hbar^2k^2}{2m} \pm \alpha_R k$

The effect of the Rashba SOC is illustrated in **Figure 1.5**. Around the minimum of the conduction band, the energy dispersion can be approximated as a parabola, with twofold spin degeneration (**Figure 1.5a**). When Rashba SOC is present **(Figure 1.5b**), the energy dispersion is split into two branches with energy $E_\pm = \frac{\hbar^2k^2}{2m} \pm \alpha_R k$ where α_R is Rashba coefficient.

1.3.3 RASHBA-DRESSELHAUS SPIN-ORBIT COUPLING IN HYBRID ORGANIC-INORGANIC PEROVSKITES

In recent years, several publications have reported the strong Rashba-Desselhaus effects in HOIPs.[35, 38-40] As a consequence, the spin degeneracy in k-space is lifted and the valence band maxima and/or conduction band minima of up- and down-spin states are shifted away from the symmetry points in the Brillouin zone triggering an indirect bandgap transition in the materials.[37, 39-42] Indirect bandgap transitions due to Rashba effects have been experimentally characterized by time-resolved photoconductivity measurements[43]

and polarization- and angle-resolved photoemission spectroscopy (ARPES)[44], and have been further supported by recent observations of a circular photogalvanic effect.[45] Opto-electronically, the indirect energy-band structure in a material demonstrating Rashba effects leads to a forbidden indirect transition that suppresses electron-hole pair recombination rates, which is beneficial for high solar cell performance. Large Rashba coefficients on the order of several eV·Å have been measured by ARPES in 3D HOIPs[44] and by electroabsorption spectroscopy in 2D HOIPs.[27] These results are very promising for spin-logic device applications[42] such as spin field-effect transistors, in which a spin current is manipulated by an applied electric field.[46-48]

CHAPTER 2

MAGNETIC FIELD EFFECT IN PEROVSKITE LIGHT EMITTING DIODES

In this chapter, we explore the possibility of manipulating the spin dynamics of charge carriers in the superlattice-like Ruddlesden-Popper hybrid lead iodide perovskite semiconductors, 2D $(BA)_2(MA)Pb_2I_7$ (with $MA = CH_3NH_3$, and $BA = CH_3(CH_2)_3NH_3$), and 3D $MAPbI_3$ by applied electric field. Magnetic field effect (MFE) on conductivity and electroluminescence in their light emitting diodes (LEDs) at cryogenic temperatures will be used to probe the Rashba-type spin orbit coupling (SOC) strength.. The sign and magnitude of the magneto-conductance (MC) and magneto-electroluminescence (MEL) responses will be quantitatively explained in the framework of the Δg-based excitonic model using rate equations. the Rashba coefficient in $(BA)_2(MA)Pb_2I_7$ with approximately 7 times larger than that in $MAPbI_3$ will be shown. First, I will introduce light emitting diodes (LEDs) and the MFE in LEDs. Second, I will present our results of studying the Rashba-Dresselhaus spin orbit coupling by the MFE on 2D/3D perovskite -based LEDs.

2.1 LIGHT EMITTING DIODES

A light emitting diode (LED) is a semiconductor device that emits light when charge current flows through it. Electrons recombine with holes in the semiconductor, releasing energy in the form of photons. The first LED, a near-infrared LED based GaAs, was invented in 1962 by James R. “Bob” Biard and Gary Pittman.[49] Twenty five years later, Tang and Van Slyke introduced the first organic light emitting diode (OLED).[50] Comparedto LEDs, OLEDs have many advantages, including environmental friendliness,

lower energy consumption, better light quality, faster response time, wider viewing angle, higher flexibility, lower cost, and ease of fabrication. Since 2013, OLEDs have been commercialized and have been used in various electronics devices such as cell phone, computer screen, television, and sensors.[51-54]

The structure of a typical OLED is shown in **Figure 2.1**. The OLED device is usually fabricated on a glass substrate or clear plastic with transparent electrodes. An

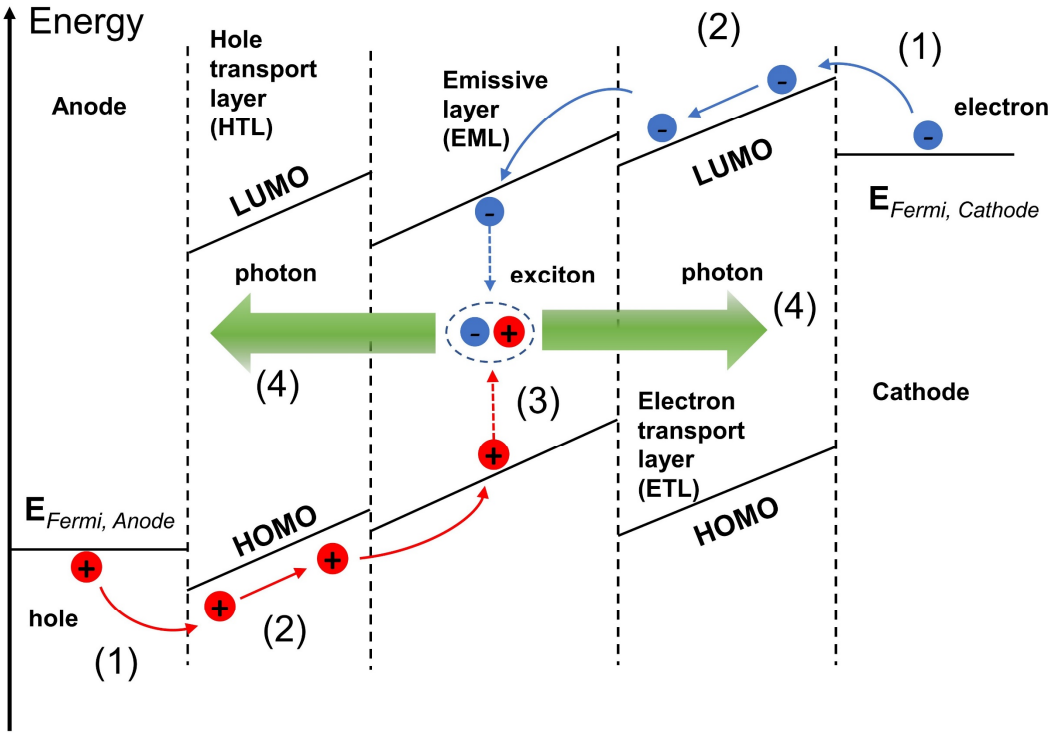

Figure 2.1. OLED working mechanism. The HUMO and LUMO energy levels of hole transport layer, emissive layer and electron transport layer are drawn tilted due to the influence of external applied voltage. Relevant processes are assigned: (1) charge carriers (electrons and holes) are injected from cathode and anode, respectively. (2) charge carriers transport in electron and hole transport layers. (3) exciton formation in emissive layer. (4) exciton decay or e/h recombination process to emit a photon.

organic semiconductor layer (emissive layer), where electrons and holes recombine and emit photons, is sandwiched between cathode and anode.[55-56] To help improve the injection of electrons and holes to emitter from cathode and anode, electrons and hole transport layers (ETL and HTL, respectively) are introduced. An anode is a transparent electrode which injects holes into the organic semiconductor layer. An anode material requires a high work function and low roughness to reduce light internal reflection. A typical anode material is indium tin oxide (ITO). Hole transport layers are materials with high hole mobility and electron blocking capacity. Commonly used HTL materials in OLEDs include 4,4',4"-Tris[phenyl(m-tolyl)amino]triphenylamine (m-MTDATA), N,N′-Di(1-naphthyl)-N,N′-diphenyl-(1,1′-biphenyl)-4,4′-diamine (NPB or NPD), copper phthalocyanine (CuPc), and poly(3,4-ethylenedioxythiophene) polystyrene sulfonate (PEDOT:PSS). Electron transport layers are materials with high electron mobility and has hole blocking ability. Tris(8-hydroxyquinoline)aluminum(III) (Alq_3), Bathocuproine (BCP), and 1,2,4-triazole-based 3-(biphenyl-4-yl)-5-(4-tertbutylphenyl)-4-phenyl-4H-1,2,4-triazole (TAZ) are usually used for ETL. The emissive layer is placed between the HTL and ETL. It should be a good emitter of visible photons and have a high photoluminescence efficiency. Emissive layer materials can be small organic molecules (Alq_3, tris(2-phenylpyridine)iridium(III) ($Ir(ppy)_3$)) or polymers ((Poly[2-methoxy-5-(2-ethylhexyloxy)-1,4-phenylenevinylene] (MeHPPV), Poly(3-hexylthiophene-2,5-diyl) (P_3HT)) . Cathode materials are often metals with low work function such as calcium (Ca), magnesium (Mg) or aluminum (Al) for a high efficiency of electron injection.[57]

The LED working mechanism is depicted in **Figure 2.1**. There are 4 important processes: (1) electrons and holes are injected from cathode and anode due to the external

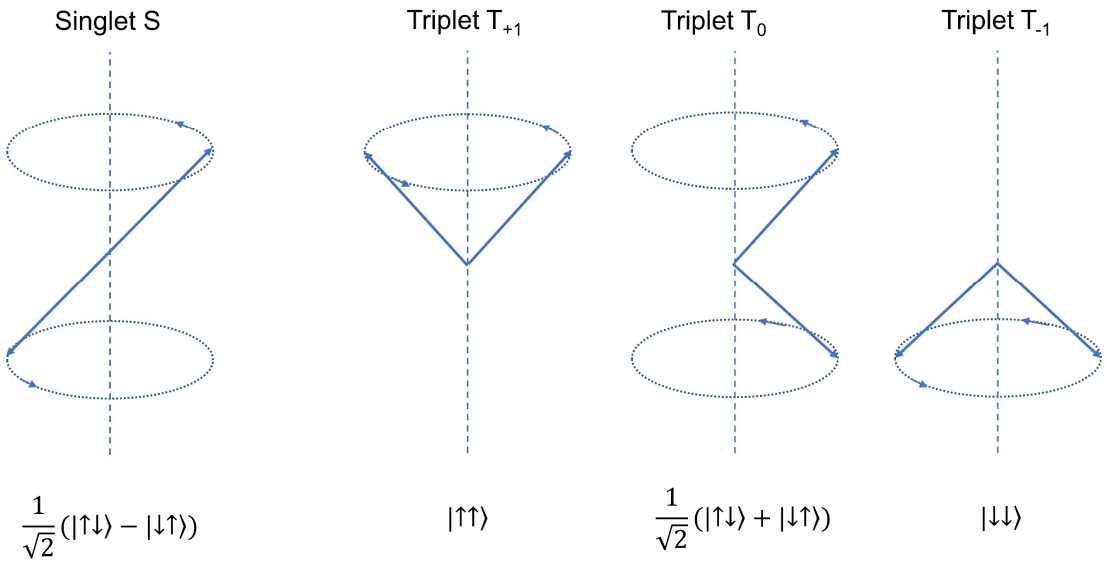

Figure 2.2. Electron hole pair spin states and corresponding wavefunctions

applied voltage. (2) The electrons and holes transport through ETL and HTL. In these layers, electrons and holes form negative and positive polarons. A polaron is a bound state of electrons (holes) with atoms/ions in crystal. Due to interaction to atoms, polarons havelower energy, lower mobility, and higher effective mass in comparison to the free charge carrier. An understanding of polarons is important for designing highly-efficient optoelectronics and photovoltaic devices. (3) positive and negative polarons form excitons, which can be either singlet excitons or triplet excitons that can (4) emit photon through fluorescence or phosphorescence, respectively. Singlet and triplet excitons are electron-hole pairs with the spin multiplicity (2S+1, where S is exciton's total spin angular momentum) of 1 and 3, respectively. Spin-allowed radiative emission (fluorescence) arises from the singlet exciton only, whereas phosphorescence is from triplet exciton. However, the phosphorescence process is very weak, because the transition is quantum mechanically spin-forbidden.[58]

When opposite charge polarons meet in the emissive layer, they first form neutral electron-hole pairs, or polaron pairs which are the precursor states of excitons. The necessary condition for the formation of a pair is that the distance between polarons (electron and hole) becomes smaller than the Coulomb capture radius. Even though the carriers in the polaron pairs are coulombically bound, they can have a large separation distance and can be located on different molecules.[56, 59-60] They still can still dissociate back into polarons and free carriers. **Figure 2.2** illustrates the spin states of an electron-hole pair and their corresponding wavefunctions. The spins of electrons and holes precess around a common quantization axis and are either upward (indicating a spin-up state) or downward (indicating a spin-down state). If the total spin of an electron-hole pair is 0, the electron-hole pair is in singlet state (S). If the total spin is 1, the pair is in the triplet states. There are 3 configurations of the triplet states: T_{+1} when the total spin is parallel, T_0 when the total spin is perpendicular and T_{-1} when it is antiparallel to the quantization axis. When the charge carriers with random spin configuration form electron-hole pairs, it follows from statistics that 25% of the formed pairs are singlet and 75% of the formed pairs are triplet. When the separation distance between electron and hole in a pair becomes small enough for their wavefunctions to overlap, the pair evolves into an exciton, a bound state of electron and hole. In semiconductors, there are two kinds of excitons: Frenkel excitons and Wannier-Mott excitons. Frenkel excitons appear in materials with a relatively small dielectric constant. For example, in organic semiconductors, the Coulomb interaction between an electron and a hole may be strong while the exciton size is small (on the same order of the unit cell). Due to the strong interaction of electrons and holes, the binding energy in Frenkel excitons is large, on the order of 0.1 to 1 eV. Molecular excitons can

even be entirely located on the same molecules, as in fullerenes.[61] In inorganic semiconductors such as perovskites, the dielectric constant is generally large. Therefore, electric field screening tends to reduce the Coulomb interaction between electrons and holes. Consequently, the exciton, termed a Wannier-Mott exciton, has larger radius in comparison to the crystal's lattice. The binding energy of Wannier- Mott exciton is much smaller than that of Frenkel excitons, and is typically on the order of 0.01 eV. A Wannier-Mott exciton has an energy and radius associated with it, called the exciton Rydberg energy and exciton Bohr radius, respectively.[62] The energy is:

$$E(n) = \frac{\left(\frac{\mu}{m_0\,\varepsilon_r^2} R_y\right)}{n^2} \equiv -\frac{R_X}{n^2}$$

Where R_y is the Rydberg constant, ε_r is the static relative permittivity, $\mu = (m_e^* m_h^*)/(m_e^* + m_h^*)$ is the reduced mass of the electron and hole, m_e^* and m_h^* are electron and hole effective mass, respectively. whereas m_0 is the electron mass.

The radius of a Wannier-Mott exciton is:

$$r_n = \left(\frac{m_0\,\varepsilon_r\,a_H}{\mu}\right) n^2 \equiv a_X\,n^2$$

Where a_H is the Bohr radius. For example, in GaAs, the relative permittivity is 12.8 and effective mass of electron and hole are 0.067 m_0 and 0.2 m_0, giving an exciton binding energy of 4.2 meV and exciton radius of 13 nm. In 3D perovskites, recent investigation showed direct observation of 1s and 2s exciton states at low temperature in $MAPbI_3$ and $MAPbBr_3$ single crystal. The binding energy and Bohr radius in $MAPbI_3$ are 16 meV and 4.6 nm, and 14 meV and 3.8 nm, respectively.[63-65]

In the 2D Ruddlesden-Popper perovskite materials, exciton luminescence contributes significantly to the photoluminescence spectra, and the exciton Rydberg states

were observed.[19, 22] Due to the confinement effect in quantum well structure, the binding energy in 2D Ruddlesden-Popper is much larger compared to their 3D counterparts. With 2D n = 1 perovskite $(BA)_2PbI_4$, the exciton binding energy is 470 meV, and the Bohr radius ~ 0.6 nm. When n increases, the binding energy decreases and the Bohr radius increases. With n =5 $(BA)_2MA_4Pb_5I_{16}$, the binding energy is 125 meV and the Bohr radius is ~1.2 nm.[22]

The spins of electrons and holes in an electron-hole pair and exciton interact with each other via a spin-spin interaction with a Hamiltonian:[66]

$$H_{spin-spin} = -\hbar J(r)(\frac{1}{2} - 2\overrightarrow{S_e}\overrightarrow{S_h})$$

Where $J(r) \sim exp(-r)$ is an exchange parameter, $\overrightarrow{S_e}$ and $\overrightarrow{S_h}$ are spin of electron and hole, respectively. Because of this interaction, the energy levels of a singlet state S and triplet state T_0 are separated with a value of ΔE_{ST}. ΔE_{ST} in polaron pairs is small, and may be negligible if the distance between electron and hole are large (loose-bound pair).[56, 60] ΔE_{ST} in exciton state, because the distance between electron and hole in exciton is small, is much larger than that of polaron pair.

Intersystem Crossing (ISC)

Because the energy difference between singlet and triplet polaron pairs is small, a process called "Intersystem Crossing", in which a singlet state becomes a triplet state, or a triplet state becomes a singlet state, can occur. The compensated energy can come from HFI or SOC, depending on which mechanism is dominant in the material. A singlet state can transform into all triplet state configurations. However, when polaron pairs are placed under applied magnetic field, triplet state energy levels are split due to the Zeeman effect. The large difference between singlet state S and triplet states T_{+1} and T_{-1} will prevent ISC.[60]

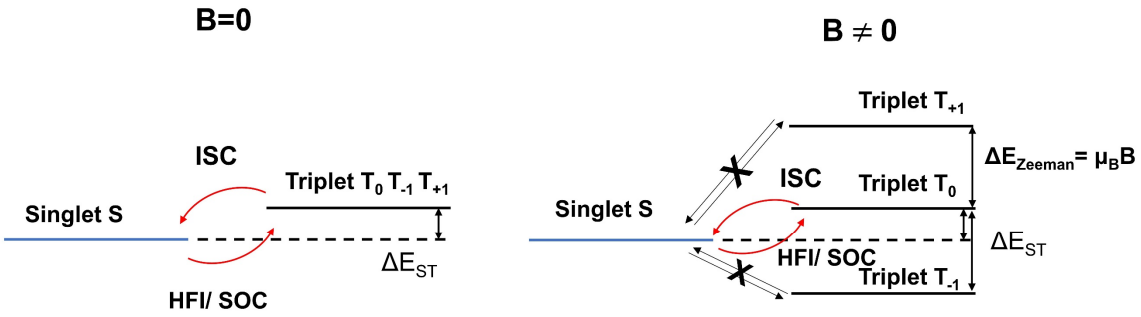

Figure 2.3. Scheme representation of intersystem crossing (ISC) between singlet and triplet electron-hole pairs. In the case there is no magnetic field, the energy difference between singlet and all triplet states is ΔE_{ST}, which is small and HFI or SOC can be the mechanism for the transition. If there is an external magnetic field B, the energy level of triplet states with difference spin configurations are split due to Zeeman effect. Because energy splitting is proportional to magnitude of B, large enough B can prevent all the ISC between singlet states and triplet states T_{+1} and T_{-1}.

This explains the reason why "Magnetic field effect" happens, which we will discuss in more detail in the next part. In short, the magnetic field effect is a tool for evaluating the strength of the HFI or SOC field. More useful details of MFE on OLEDs can be found in the dissertation of Dr. Ulrich.[67]

Internal and External Quantum Efficiency of Light Emitting Diodes

The internal quantum efficiency, η_{int}, is defined as the ratio of the number of photons produced within the device to the number of electrons flowing in the external circuit:[58]

$$\eta_{int} = \gamma r_{st} q$$

Where γ is the ratio of the number of exciton formation events within the device to the number of electrons flowing in the external circuit. r_{st} is the fraction of excitons which are

formed as singlets, and q is the efficiency of radiative decay of these singlet excitons. To achieve high-efficiency electroluminescence, it is necessary to have a good balance of electrons and hole current, effective formation of excitons in the emissive layer, and high radiative transition probability of singlet excitons.

The external quantum efficiency (EQE), η_{ext}, is defined as:

$$\eta_{ext} = \eta_{int}\,\eta_{ph}$$

Where η_{ph} is the light-out coupling, $\eta_{ph} \approx \frac{1}{2n^2} \approx 20\%$ for a glass substrate with index of refraction of 1.5. Therefore, without using light output coupling strategy, the theoretical limit of η_{ext} is ~5% when η_{int} reaches its maximum value, 25%, when all ratios, γ , q ,and r_{st} reach their maximum values, which are 1, 1, and 0.25.

Hybrid organic inorganic perovskites-based light emitting diodes

Hybrid perovskites are also promising materials for LEDs, thanks to their facile solution processing, high color purity and tunable bandgap.[68-69] A lot of effort has been made to obtain stable and high-efficiency perovskite LEDs. A few excellent works that demonstrated a device with EQE of larger than 20% can be listed here.[70-72] By applying a new strategy for managing the compositional distribution in the device to boost the luminescence and balance charge injection, Lin et al. reported 20.3% of external quantum efficiency of Perovskite $CsPbI_3$/MABr LED.[70] Another strategy to obtain highly efficient Perovskite LEDs is maximizing the light output coupling. Cao et al. reported that by simply introducing amino-acid additives into the perovskite precursor solutions, submicrometer-scale perovskite structure can be formed, which helps extract light and passivate perovskite surface defects and reduce nonradiative recombination. The peak EQE from his work reacheded 20.7%.[71] Another noteworthy report is by Zhao et. al. To enhance radiative

emission processes in LED, they prepared a heterostructure from a combination of quasi 2D/3D perovskites and a wide optical gap polymer. Thanks to efficient energy transfer process between 2D and 3D perovskites, a nearly 100% internal quantum efficiency was achieved, and the hybrid perovskite LED reached an EQE of 20.1%.[72]

2.2 MAGNETIC FIELD EFFECT ON LIGHT EMITTING DIODES

Magnetic field effect (MFE) is the general term used for several effects including:

1. Magnetoresistance (MR) or Magnetoconductance (MC): resistance of a device (light emitting diode, spin valve, or solar cell) changes under an applied magnetic field.
2. Magnetoelectroluminescence (MEL): electroluminescence of light emitting diodes changes under an applied magnetic field.
3. Magnetophotocurrent (MPC): photocurrent intensity of solar cells changes under an applied magnetic field.
4. Magnetophotoluminescene (MPL): photoluminescence intensity of semiconductor materials changes under an applied magnetic field.

In this chapter, only the MFE on light emitting diodes (MC and MEL) is studied. In chapter 4, MPL will be used for investigating the energy transfer between perovskite and singlet fission materials.

The first report on magnetic field effect on light emitting diode was given by Kalinowski et al. in 2003.[73] The MC and MEL of an Alq_3-based OLED are observed and up to 3% under an applied magnetic field of 500mT. This observation received increasing the attention from research community and after that, a lot of excellent work and effort have been dedicated to investigate the phenomenon.[74-76]

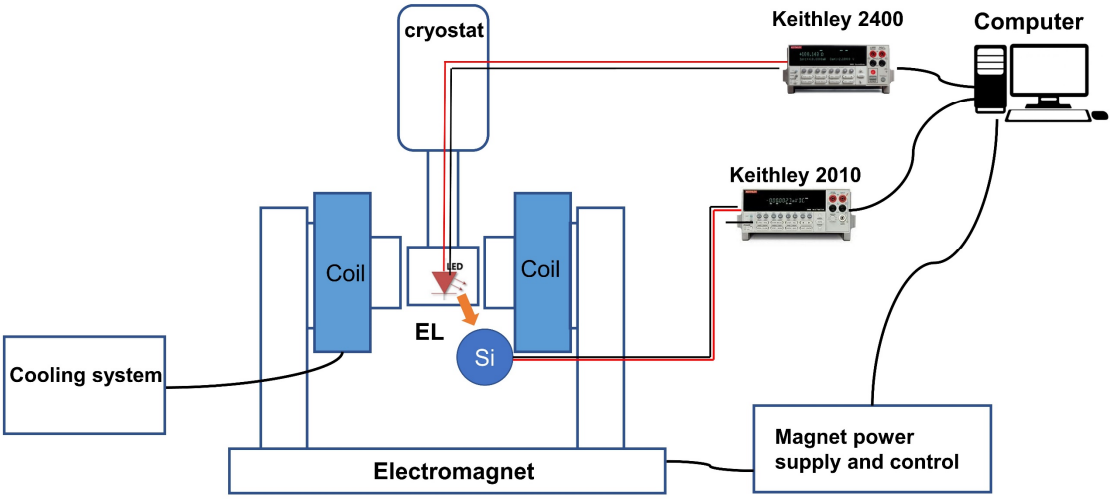

Figure 2.4. Magnetic field effect (MFE) measurement setup. The sample (OLED) is mounted on the cold finger of a closed-cycle helium cryostat purchased from Advanced Research System. The cryostat is placed between two poles of an electromagnet that can produce a magnetic field up to 300mT with a one-Gauss resolution. The devices were driven at constant voltage using a Keithley 2400 source-meter unit and the EL intensity was simultaneously measured by a Si photo-detector, while sweeping B.

Figure 2.4 depicts a schematic of the MFE measurement setup. The sample (OLED) is mounted on the cold finger of a closed-cycle helium cryostat purchased from Advanced Research Systems. The cryostat is placed between two poles of an electromagnet that can produce a magnetic field up to 300mT with a one-Gauss resolution. The devices were driven at constant voltage using a Keithley 2400 source-meter unit and the EL intensity was simultaneously measured by a Si photo-detector, while sweeping B. The MC is defined as follows:

$$MC(\%) = \frac{I(B) - I(0)}{I(0)} 100\%$$

Where *I(B)* and *I(0)* are the current flowing through the device with and without an applied magnetic field B. Similarly, MEL is defined as:

$$MEL(\%) = \frac{EL(B) - EL(0)}{EL(0)} 100\%$$

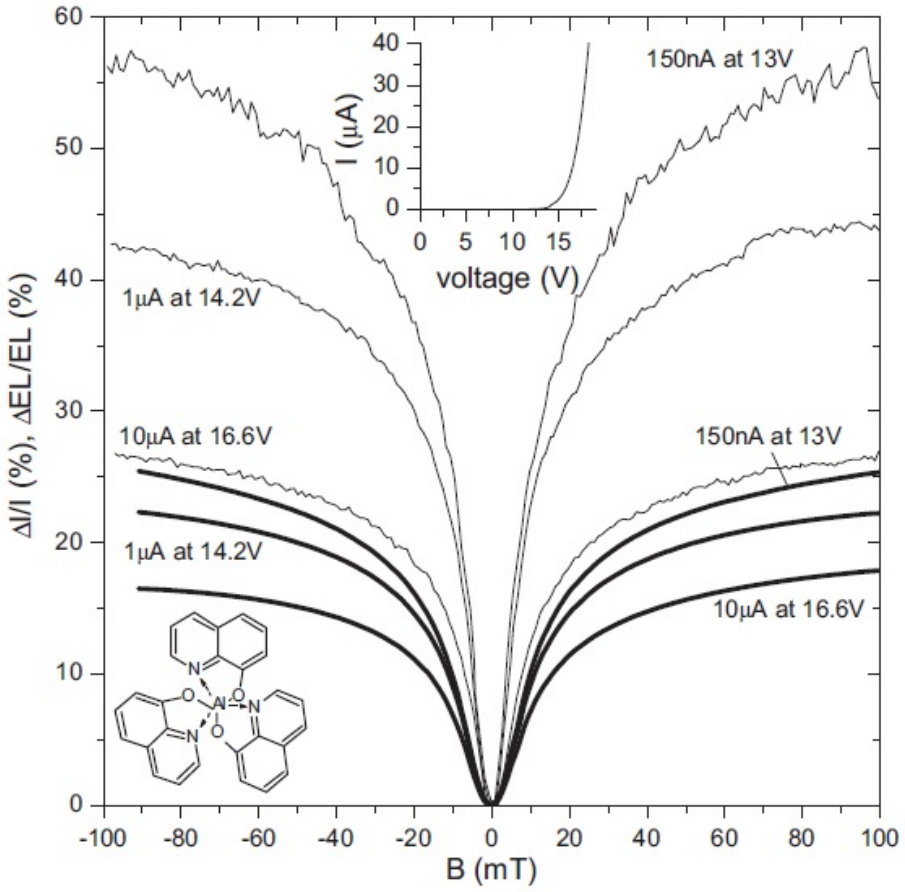

Figure 6 Magnetic field effect (MFE) on conductance (bold lines) and EL (thin lines) in a PEDOT/Alq3 (~150nm)/Ca device measured at several different constant voltages at room temperature. The current-voltage characteristics of the device and the chemical structure of Alq3 are shown as inset. Adapted from reference[3]

Where *EL(B)* and *EL(0)* are the device's electroluminescence intensity with and without an applied magnetic field B.

The typical results of MC and MEL from OLED is illustrated in **Figure 2.5**, which shows the MC and MEL from an Alq_3-based OLED[3]. The MC and MEL curves obey the empirical laws $\frac{\Delta I}{I} \sim \frac{B^2}{(B^2+B_0^2)}$ or $\frac{\Delta I}{I} \sim \frac{B^2}{(|B|+B_0)^2}$, depend on material. The constant B_0 is ~ 5mT for most organic materials.[77]

Magnetic field effect's mechanism

There are a few mechanisms have been proposed to account for magnetic field effects in OLED. The main mechanisms, which are widely accepted from the spintronics research community, are the bipolaron mechanism, loosely-bound polaron pair mechanism, triplet-exciton polaron quenching mechanism and Δg mechanism.[33, 56, 74, 78-81] Each of these mechanisms tries to explain how the transition (ISC) rate between singlet and triplet states in the material change under the applied magnetic field. Details of the models' explanation can be found in an excellent review from Geng et al.[56] However, it is noteworthy that there are two interactions which decide the mechanisms. In organic materials, HFI is dominant and is the reason for spin mixing (HFI-based ISC). A lot of experimental results and theoretical works have proved the role of HFI in MFE on OLEDs[33, 74, 78, 82]. In materials with heavy Z number atoms, SOC is the dominant interaction and is the reason for ISC through Δg mechanism. The Δg mechanism relies on the difference in gyromagnetic g factor between electron (negative polaron, g^-) and hole (positive polaron, g^+). Since electron and hole's spins precess with different Larmor frequencies, the ISC rate (or mixing rate between singlet and triplet states) is proportional to $(g^+ - g^-).B = \Delta g.B$.[83]

Magnetic field effect on Perovskite thin films and devices

Besides our report on magnetic field effect on perovskites-based LEDs,[84] up to this point in time, (March 2021) there have been only 4 papers on this interesting topic. The first two reports of MFE on perovskite are both on 3D $CH_3NH_3PbI_{3-x}Cl_x$ perovskite-based solar cell.[81, 85] In 2019, Wang et. al. presented Giant magnetoresistance (GMR) in $MAPbBr_3$-based spin valve.[86] In 2020, Pan et. al. observed MEL from 3D-$MAPbI_3$ and 2D-$(PEA)_2PbI_4$ (PEA = $C_6H_5(CH_2)_2NH_3)_2$).[87] In these report, the magnetic field effect on perovskite thin films and devices are observed with a much smaller magnitudes comparing to those from organic light emitting diode. In details, Zhang et. al. reported MC in 3D perovskite-based solar cell from 0.03% to 2.4%, depending on the perovskite film's morphology and power conversion efficiency.[81] MEL from the corresponding perovskite's films also observed, with extremely small magnitudes, in the range of 0.03% to 0.12%. Hsiao et. al. showed a magnetic field effect on photocurrent in the same perovskite solar cell (based $CH_3NH_3PbI_{3-x}Cl_x$) with the magnitude depending on the excitation intensity. The maximum MPC observed were ~ 0.5% whereas the magnitude of MPL from the corresponding perovskites films, also depends on excitation intensity, and can be large up to 1.2% at room temperature.[88] In perovskite thin films, the large SOC significantly decreases the spin lifetime τ of electrons and holes. Therefore, to observe MFE, the Δg in perovskite should be much larger than that of organic semiconductors, where the Δg value is on the order of 10^{-3}. Using field induced circularly polarized photoluminescence and electron-hole pair lifetime measurements by picosecond pump-probe spectroscopy techniques, Zhang et. al. found that the Δg value in 3D $CH_3NH_3PbI_{3-x}Cl_x$ perovskite is ~0.65, which makes the Δg mechanism viable for MFE generation. Δg mechanism were

also used to explain the observation of MEL in 2D-$(PEA)_2PbI_4$-based LED. The spin lifetime in 2D and 3D perovskites were estimated by MEL results and validated by picosecond transient polarized photoinduced absorption technique (TPPA). The results reveal that the spin lifetime in 2D-$(PEA)_2PbI_4$ is ~80 ps, which is 5 times smaller than that of the 3D $MAPbI_3$. This indicates the SOC in 2D-$(PEA)_2PbI_4$ is much larger than that of the 3D.

2.3 MAGNETIC FIELD EFFECT IN PEROVSKITE LIGHT EMITTING DIODES

In this part, I will present our results from studying the SOC in 2D and 3D HOIPs by using MFE on perovskite-based LEDs. The Rashba-Dresselhaus SOC is expected to larger in 2D perovskites due to the non-centrosymmetric property and quantum confinement effect of the 2D materials. Although there are some reports in literature on the study of SOC of 2D Ruddlesden-Popper and 3D MAPI, for example, large Rashba coefficients on the order of several eV·Å have been measured by angle resolved photo electron spectroscopy (ARPES) in 3D HOIPs[44] and by electroabsorption spectroscopy in 2D HOIPs,[27] there has been no direct comparison of SOC strength in 2D and 3D perovskites. Moreover, they are all based on optical methods, and no one has tried to manipulate or control the SOC by external electric field. It is our motivation to conduct an experiment that can directly compare the SOC in 2D and 3D perovskites, and we would like to see how an external electric field can manipulate the SOC strength in perovskites. Therefore, MFE in perovskite-based LEDs is an ideal experimental tool for this study.

The perovskite-based LED architecture is depicted in **Figure 2.6a**. The fabrication of the organic sandwich devices started with patterning 40 nm of indium-tin-oxide (ITO) on a glass substrate using photolithography and chemical etching. Then, the ITO-coated

glass substrate was thoroughly cleaned with soap, distilled water, acetone, and isopropanol in an ultrasonic bath. The conducting polymer poly(3,4-ethylenedioxythiophene)-poly (styrenesulfonate) (PEDOT) from Ossila was spin coated at 4000 rpm for 60 s on top of the ITO-coated glass substrate yielding a thin PEDOT layer of ≈ 20 nm thick to provide an efficient hole injecting electrode. All other fabrication steps were carried out in a nitrogen filled glovebox. Inside the glovebox, the perovskite solutions and glass substrates were preheated to 80°C for 30 min. Then, the perovskite solution was spin coated onto the substrate at 5000 rpm for 30 s resulting in films with thicknesses of ≈ 50 nm and ≈ 130 nm

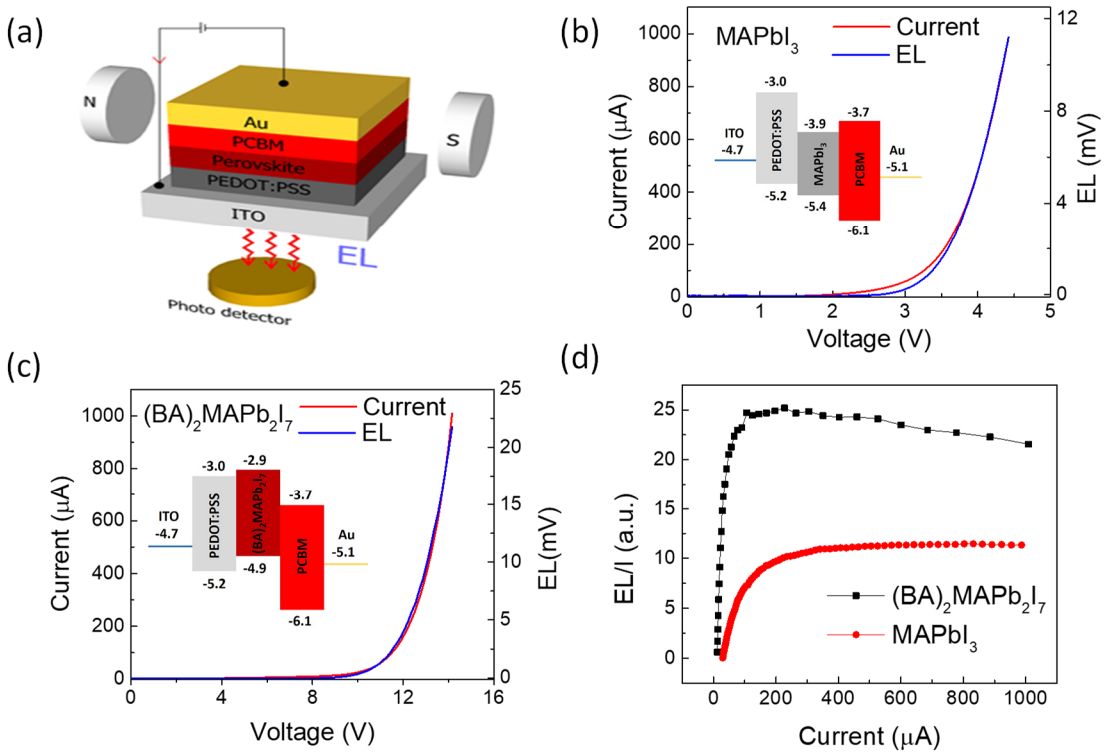

Figure 2.6. (a) Light emitting diodes (LED) based on 3D and 2D HOIPs. The current-voltage (I-V) and electroluminescence-voltage (EL-V) characteristics for 3D and 2D HOIP based LEDs are shown in (b) and (c) at 10 K. The insets in (b) and (c) show the energy diagram of devices. (d) EL quantum efficiency of the LEDs.

for $MAPbI_3$ and $(BA)_2(MA)Pb_2I_7$, respectively. Next, a phenyl-C61-butyric acid methyl ester (PCBM) solution with a concentration of 20 mg/ml in toluene was spin coated directly on the perovskite film to form a thin electron transport layer of ≈ 20 nm-thick. Finally, a 50 nm-thick Au top electrode was deposited through a shadow mask using an electron beam evaporator at a rate of 0.5A/s in a base pressure of $\approx 1 \times 10^{-6}$ mbar. The LED active area is ≈ 1 mm^2. We note that we used the Au electrode as an electron-injector in order to maximize the applied electric field on the devices.[89] But such a structure commonly yields a low EL quantum efficiency. The band diagrams of the devices are shown in the insets of **Figure 2.6b** and **2.6c**.

Figure 2.6b and **Figure 2.6c** respectively show the current-voltage (I-V) and electroluminescence-voltage (EL-V) for $MAPbI_3$ and $(BA)_2(MA)Pb_2I_7$ based LEDs as described in **Figure 2.6a**. The spin dynamics of phase-pure HOIPs were investigated at 10 K because the luminescence response is much stronger at low temperatures than at room temperature. The turn-on voltage for the EL (at ≈ 2.3 V and ≈ 10 μA) in 3D $MAPbI_3$ LED is lower than that observed in 2D $(BA)_2(MA)Pb_2I_7$ LED (at ≈ 8.6 V and ≈ 12 μA) mainly because the $(BA)_2(MA)Pb_2I_7$ LED has a thicker emissive layer (≈ 130 nm) than that in $MAPbI_3$ LED (≈ 50 nm).[90] In addition, the larger band-gap in $(BA)_2(MA)Pb_2I_7$ HOIP (≈ 2.0 eV in comparison to ≈1.5 eV in the $MAPbI_3$ HOIP) also results in the higher EL turn-on voltage. Finally, the low out-of-plane conductivity of $(BA)_2(MA)Pb_2I_7$ LED may also play a detrimental role in charge transport across the highly oriented organic sheets which have low hoping/tunneling charge mobility. We note that the devices have Ohmic contacts with hole-only transport at the voltage below the EL-turn on voltages. However, the electron-hole recombination is quite strong at higher applied voltages.

The EL quantum efficiency (ELQE), which is proportional to the ratio of the EL intensity over the current density, is plotted in **Figure 2.6d**. The ELQE in both devices monotonically increases from zero and saturates at a current density of ≈ 200 μA/mm^2. However, the ELQE in 2D $(BA)_2(MA)Pb_2I_7$ continues to decrease at higher current densities. This slight ELQE reduction may be associated with exciton loss due to strong exciton-exciton annihilation when the dense excitons at high current densities are confined

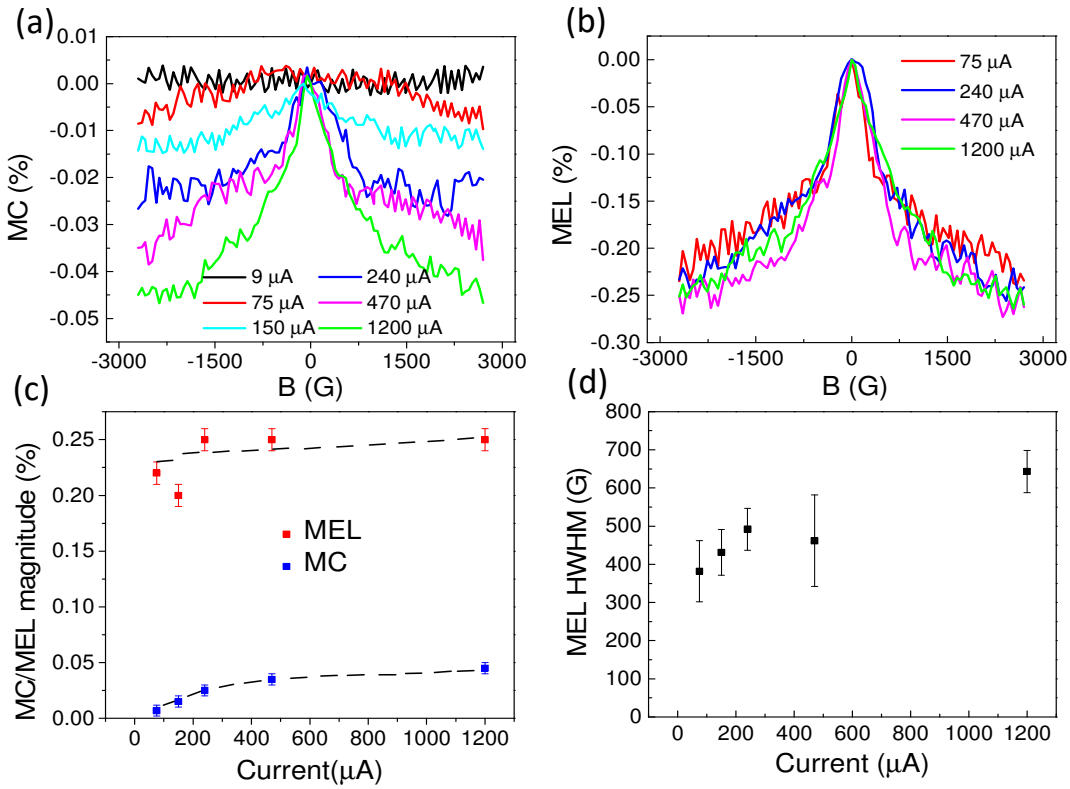

Figure 2.7. (a) Magneto-conductance (MC), and (b) magneto-electroluminescence (MEL) of a typical 3D MAPbI3 based LED at several device currents. (c) Extracted MC and MEL magnitudes versus device current. The lines are guides for the eyes. (d) The haft width at half maximum (HWHM) of MEL response extracted directly from (b) versus device currents.

in a 2D well. Next, we will show MFE studies on the devices' conductivity and EL intensity at different current densities in the Ohmic and exciton recombination regimes.

Figure 2.7a shows the typical MC responses up to 3 kG at six different current densities for a 3D $MAPbI_3$ LED, where the MC magnitude is found to increase with increasing current density and saturate at ≈ 200 μA. At a current of 75 μA, the MC is about (0.01 ± 0.005) % while at a current of 1200 μA, the MC reaches (0.05 ± 0.005) % at an applied field of 3 kG. We do not observe any MC response within 0.005% noise when the current density is below the turn-on current density for the EL (see MC at ≈ 9 $\mu A/mm^2$ in **Figure 2.7a**). It is also important to note that the MC current noise level may distort the shape of the MC at low current densities. For example, the MC at 75 μA is less than 0.01%, which is only about 2 times larger than the noise level. **Figure 2.7b** shows the corresponding MEL responses at several current densities. In contrast to the MC response, the MEL response remains the same magnitude of ≈ (0.22 ± 0.03) % at all current densities. The magnitude of MC and MEL versus the device current extracted directly from **Figure 2.7a** and **Figure 2.7b** are plotted in **Figure 2.7c** where the MC magnitude monotonically increases from zero and saturates at ≈ 200 μA, in agreement with studies of the magneto-photocurrent trend reported in Zhang *et al*.[81] Interestingly, the MC magnitude trend is the same as the ELQE response as shown in **Figure 2.7d**. In general, the MEL and MC responses are similar with an exception observed at low current density of 75 $\mu A/mm^2$. This suggests that the MEL and MC share the same physical interpretation. Since the MFE is not observed when the EL is absent and the MEL magnitude is much larger than the MC magnitude, the magnetic field must primarily act on the EL, and MC is just a secondary effect, e.g. from electron-hole pair dissociation. This indicates that the MC response must

have an excitonic origin where the intersystem crossing between singlet and triplet electron-hole pairs[81] or triplet-charge interaction (or trion)[91] may take place. We note that both mechanisms require the existence of trapped charges, and long exciton lifetimes to have sizable magnetic field effect.[81] Nevertheless, the triplet-charge interaction requires a long-lived triplet exciton in the ms range, typically found in organic semiconductors. This long-lived triplet exciton is unlikely to occur in HOIPs due to the exceptionally strong

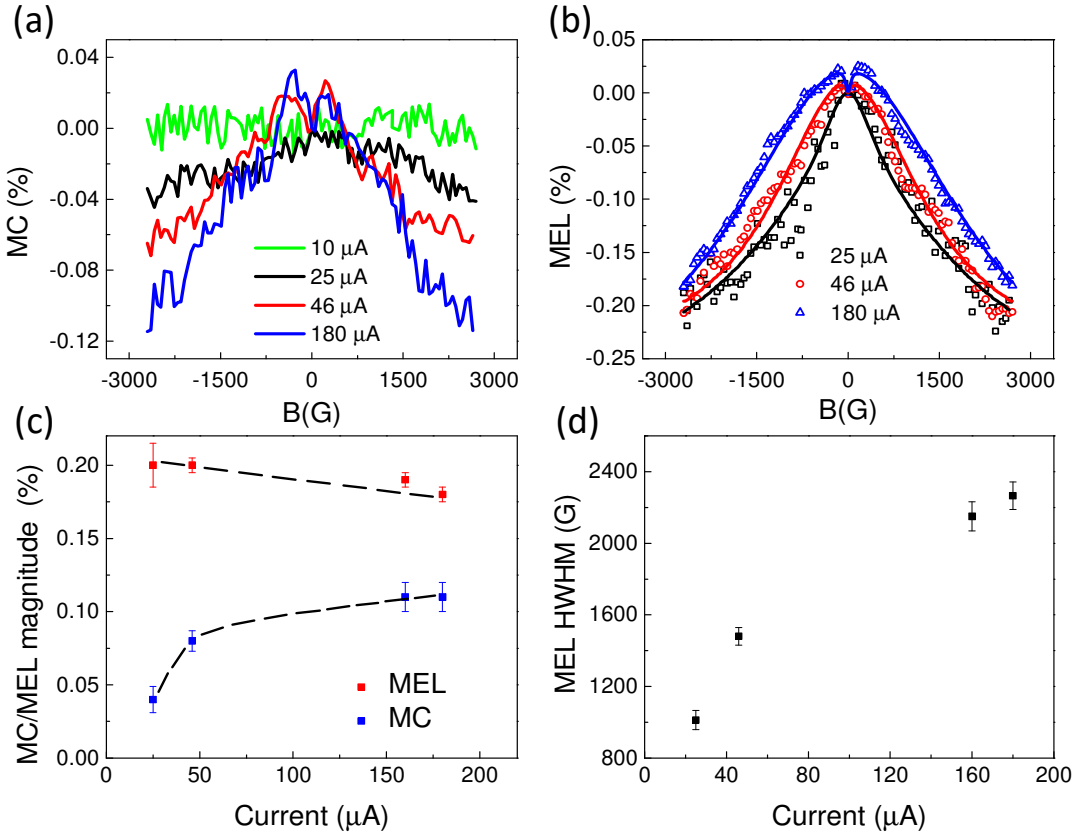

Figure 2.8. (a) Magneto-conductance (MC), and (b) magneto-electroluminescence (MEL) of a typical 2D $(BA)_2(MA)Pb_2I_7$ based LED at 10, 25, 46, and 180 μA device currents. The lines show best fits with a double-Lorentzian function. (c) MC magnitude and MEL magnitude versus device currents. The lines are guides for the eyes. (d) The half at half maximum (HWHM) of the MEL response obtained from the Lorentzian fitting versus device currents.

SOC. In fact, to the best of our knowledge, the trion formation has not been reported in HOIP thin films. Zhang *et al*. showed that electron-hole lifetimes of HOIP films is in the ps range and increases with trapped charges.[81] The authors found that the magneto-photocurrent is associated with the intersystem crossing rate between singlet-triplet excitons, which is not affected by the hyperfine interaction, but the so-called Δg mechanism. Remarkably, the half width at half maximum (HWHM) of the MEL response or effective local magnetic field in Figure 15d slightly increases with increasing the current density. This implies that the applied electric field might influence the spin mixing processes among the spin sublevels or the intersystem crossing rate between singlet and triplet electron-hole pairs via the Rashba effect.[56, 92-93]

Figure 2.8a and **Figure 2.8b** show the MC and MEL responses for a 2D $(BA)_2(MA)Pb_2I_7$ LED. Similar to the response for $MAPbI_3$, the MC magnitude increases monotonically and saturates at ≈ (0.11 ± 0.02)% while the MEL magnitude is larger and remains essentially the same at ≈ (0.20 ± 0.02)% with increasing current density (see **Figure 2.8c**). The MC response is not detectable within 0.01% noise when the current density is smaller than 10 μA/mm^2. Both MC and MEL contain two components at small field and high field, which are usually observed in organic semiconductors with strong intrinsic SOC.[93-94] Since the MC magnitude versus the LED current follows the same trend as the ELQE trend shown in **Figure 2.8d**, we conclude that MC in 2D $(BA)_2(MA)Pb_2I_7$ LED device must have the same excitonic origin as the MC in the 3D $MAPbI_3$ LED device. Since the MEL response of 2D $(BA)_2(MA)Pb_2I_7$ is noisy and very broad, we are not able to saturate the response at an applied field of 3 kG. Instead, we fitted the data with a double-

Lorentzian function ($MEL_1*B^2/(B^2+B_1^2)$ + $MEL_2*B^2/(B^2+B_2^2)$), where MEL_1, MEL_2, B_1, B_2 are fitting parameters. All fitting parameters are presented in **Table 1.**

Table 1. Fitting parameter of the 2D perovskite LED's MEL responses with a double-Lorentzian function.

Current (μA)	MEL_1	MEL_2	B_1 (G)	B_2 (G)	B_2 error (G)
25	0	-0.00223	0	1030.4	53.2
46	0.0001	-0.00269	0.10	1480.4	49.7
160	0.00015	-0.0021	0.17	2150.3	81.9
180	0.00022	-0.00342	0.11	2278.1	77.7

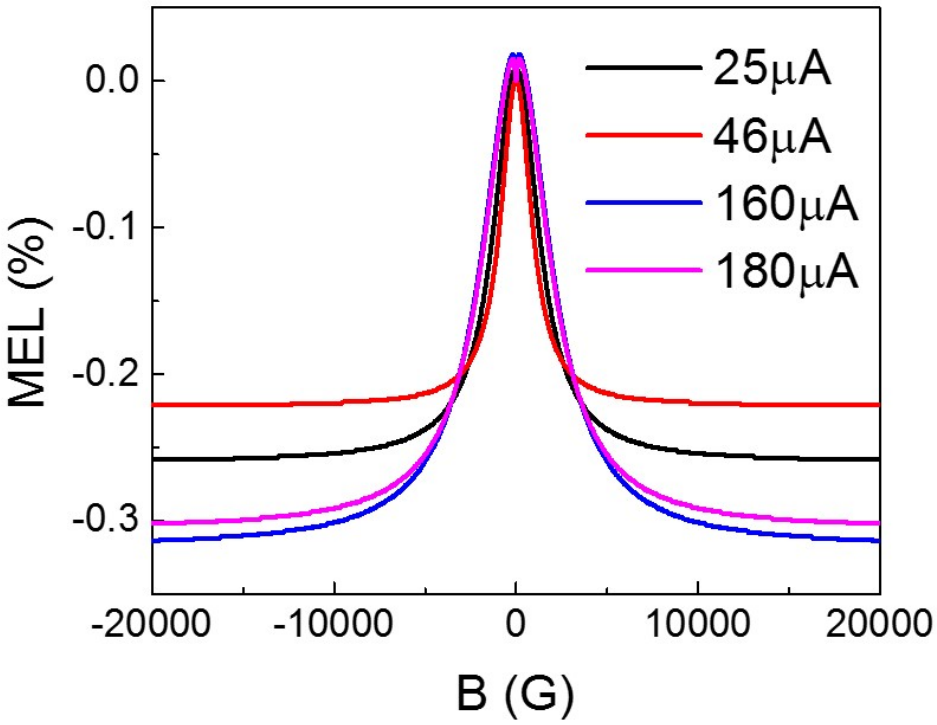

Figure 2.9. MEL responses getting from the fits of the experimental MEL responses as such in Figure 16b. The data is plotted up to 20kG.

The lines in **Figure 2.8b** shows the fit result up to 3 kG while **Figure 2.9** shows the fit lines up to 20 kG. The HWHM of the MEL response extracted from the fitting in **Figure 2.9** (B_2 values in Table 1) versus the LED current is plotted in **Figure 2.8d**. The width nonlinearly increases with increasing current density. Clearly, the spin dynamics in 2D and 3D materials follow the same mechanism.

It has been extensively studied in organic semiconductors that strong SOC suppresses the MFE magnitude while broadening the HWHM.[93-94] The MFE studies in 2D and 3D HOIPs based LEDs agree very well with those in organic semiconductors. In contrast, the MFE in HOIPs is insensitive to hyperfine interaction due to ultra-short exciton lifetime.[81]

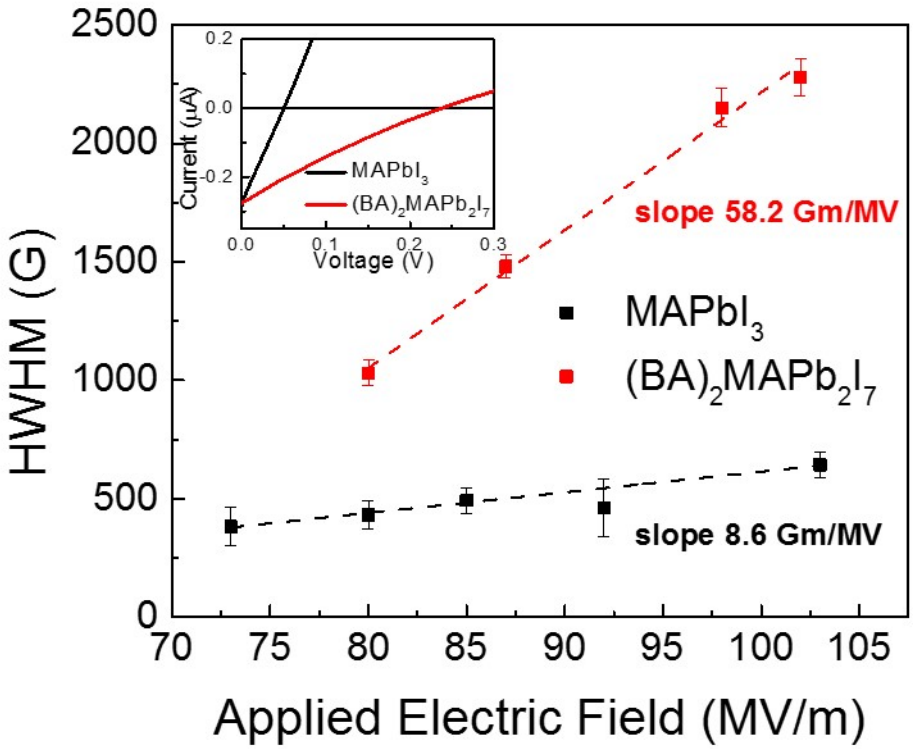

Figure 2.10. The HWHM of MEL response for 2D and 3D OIHP based LEDs versus applied electric field. The dashed lines show linear fits. The inset shows the photocurrent response of the devices.

In addition to the intrinsic SOC, HOIPs may exhibit strong Rashba type SOC with exceptionally large Rashba coefficients due to the bulk and structural symmetry breaking as discussed in the introduction. Such properties allow the control the Rashba SOC strength, and hence spin dynamics, by an applied electric field.[47-48, 95] **Figure 2.7d** and **2.8d** clearly show that the spin response becomes stronger at larger current density or larger applied voltage.

To investigate the effect of Rashba SOC on the MEL response, we replotted the results presented in **Figures 2.7d** and **2.8d** as a function of applied electric field rather than the current density. It is reasonable to assume that the electric field drops are negligible across the PEDOT:PSS hole transport layer and PCBM electron transport thin layers.[89] Therefore the applied electric field, E, can be estimated by $E = (V-V_{OC})/d$, where V is the applied voltage, V_{OC} is the open circuit voltage which can be extracted from the photocurrent (see **Figure 2.10,** inset) in which the I-V characteristics were taken under 450 nm laser illumination at 100 mW/cm^2, and d is the thickness of the HOIP thin film. Interestingly, for both 3D and 2D HOIPs, the MEL HWHM increases linearly with the applied electric field. We fit the data with a linear function. We found that the effective SOC energy ($\boldsymbol{B_{Rashba}}$) in the $(BA)_2(MA)Pb_2I_7$ HOIP increases at a large rate of 58.2 G·m /MV in comparison with 8.6 G·m /MV for the $MAPbI_3$ HOIP (**Figure 2.10**). The applied electric field along the 2D wells in the $(BA)_2(MA)Pb_2I_7$ HOIP causes significant manipulation of local electric field, **E** and hence $\boldsymbol{B_{Rashba}}$. Our results are consistent with the experimental results reported by Wang *et al.* who observed the linear dependence of Rashba SOC energy on the applied electric field in GaAs quantum wells.[48] In the first approximation, this suggests that the Rashba coefficient in $(BA)_2(MA)Pb_2I_7$ HOIP is about 7 times larger than

the coefficient in $MAPbI_3$ HOIP. These results are in agreement with recent calculation of Rashba SOC coefficients on those materials using the second harmonic generation experimental data, where the ratio of the Rashba coefficient in the $(BA)_2(MA)Pb_2I_7$ HOIP over the $MAPbI_3$ HOIP is about 8 times.[96] Clearly, the $(BA)_2(MA)Pb_2I_7$ HOIP is more suitable for the electrically controlled spin logic device. Interestingly, the effect of electric field on the MC line shape in $(BA)_2(MA)Pb_2I_7$ HOIP is essentially the same as the effect reported by Takase *et al.* who studied the highly gate-tunable Rashba spin-orbit interaction in InAs nanowire metal-oxide-semiconductor field-effect transistor.[47]

There are several mechanisms for the spin mixing event from the spin sublevels causing intersystem crossing between singlet and triplet electron-hole pairs. These include HFI, SOC, exchange, and Δg mechanism. Since the spin relaxation time in HOIPs is very fast due to strong SOC, much slower spin precession caused by the hyperfine field cannot cause the spin mixing between the singlet and triplet electron-hole pairs.[97] We note that the magnetic field from the SOC including the Rashba-type SOC is significantly larger than the hyperfine field of ≈ 50 G[77, 82]. The large SOC field might result in a fast spin precession time that is comparable to the exciton lifetime causing the MEL and MC. For the Δg mechanism, the large spin mixing rate, $\Delta\omega_p \propto B\Delta g$, is possible at large applied magnetic field, B, and different g factors between the electron and hole in the spin pair. A Δg value of ≈ 1.0 in the HOIPs was found to be significantly larger than that in organic semiconductors (≈ 10^{-3}).[22, 81] Therefore, the Δg spin mixing is more likely a dominant mechanism in HOIPs. Because the Δg in 2D $(BA)_2(MA)Pb_2I_7$ HOIP ($\Delta g \approx 1.2$) is found to be smaller than that in 3D $MAPbI_3$ HOIP ($\Delta g \approx 1.7$),[22] the spin mixing in $(BA)_2(MA)Pb_2I_7$ HOIP would be slower than that in $MAPbI_3$ HOIP. Therefore, we would

expect to have a broader MFE response in $(BA)_2(MA)Pb_2I_7$ based LEDs. The Rahsba energy increases with increasing applied electric field in our experimental results in **Figure 2.10** implies that the Δg value must be smaller under a larger applied electric field or larger $\boldsymbol{B_{Rashba}}$. We note that such a model has been used to explain the MFE in photocurrent, which is a different concept[81]. Next, we will examine MFE using the excitonic electron-hole pair model that has been successfully applied to explain the MFE in organic LEDs. It is therefore natural to ask whether this model can explain the sign and the magnitude of MC and MEL responses in HOIPs. The electron-hole pair dynamics can be described as following: When electrons and holes are injected from the cathode and anode into the

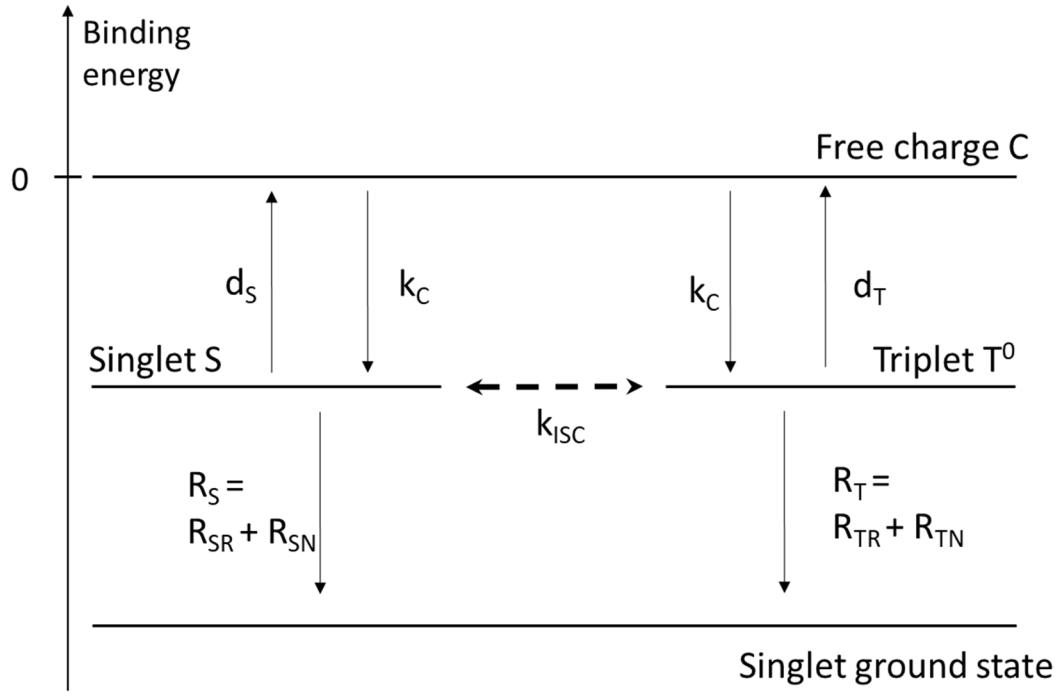

Figure 2.11. The schematic energy level diagram illustrates the simplest possible pair mechanism model, which includes three different species: free charges with population C, singlet electron-hole pairs with population S, and triplet electron-hole pairs with population T_0. Various transition rates are indicated.

organic layer, they form negative and positive charges, respectively. When the separation between an electron and a hole is less than the Coulomb capture radius, the carriers are organized in loosely bound electron-hole pairs with the rate k_C, statistically 25% spin singlet pair *S with zero spin*, 75% spin triplet pairs T^0, T^1, and T^{-1} where 0, 1 and -1 is the spin triplet multiplicity. Since the electrons and holes in HOIPs are highly delocalized due to the dielectric screening, electrons and holes in the excitonic form are loosely bound with an excitonic binding energy of a few meV [98-99]. In the first approximation, the exchange interaction energy between singlet and triplet electron-hole pair is negligible. Finally, the singlet and triplet electron-hole pairs can recombine with the rate R_S and R_T or dissociate to form free charges (C) with the rate d_S and d_T, respectively. The rate R_S (R_T) might include radiative recombination with the rate R_{SR} (R_{TR}) or non-radiative recombination with the rate R_{SN} (R_{TN}). We now formulate the appropriate rate equations. The relevant levels and transition rates are shown in **Figure 2.11**.

The basic idea of the exitonic model is that the multiplicity of the singlet and triplet electron-hole pairs changes with time due to spin dynamics induced by either the Δg mechanism or SOC. While the SOC can mix all triplet excitons with singlet excitons, the non-zero difference in the g-factor of electrons and holes, Δg, leads to the spin mixing rate, k_{ISC} between the isoenergetic S and T^0. Since Δg is significantly larger in HOIPs, the Δg effect is more likely to play a crucial role in the observed Rashba effect. Therefore, the schematic energy diagram in **Figure 2.11** based on the Δg mechanism is examined. Several rate equations can be written from the diagram in **Figure 2.11**:

$$-k_C C + d_S S + d_T T^0 = G_C \qquad (2.1)$$

$$k_C C - (d_S + R_S + k_{ISC})S + k_{ISC} T^0 = 0 \qquad (2.2)$$

$$k_C C + k_{ISC} S - (d_T + R_T + k_{ISC}) T^0 = 0 \qquad (2.3)$$

where G_C is the generation rate for C, which is equal to the rate of carrier injection minus the rate of emission of carriers at the electrodes. At zero applied magnetic field, it is obvious that $k_{ISC} = 0$. At large applied magnetic fields, we supposed that the k_{ISC} is much larger than other transition rates. We suppose $d_S = d_T$, the LED current $\approx C$, and $EL \approx R_{SR} S + R_{TR} T \approx R_{SR} S \sim R_S S$ for most HOIPs[100]. We obtain the following solutions from the rate equations (2.1-2.3):

$$MEL = \frac{(1 - R_S/R_T)}{\left(1 + \frac{R_S}{R_T}\right)(d_S/R_T + 1)} \qquad (2.4)$$

$$MC = \eta \frac{-(1 - R_S/R_T)^2}{2(1 + R_S/R_T)(1 + R_S/ds)(d_S/R_T + 1)} \qquad (2.5)$$

where η is the fraction of the injected carriers that form electron-hole pairs. In general, MEL and MC are non-zero if the recombination rate of singlet and triplet are different. Now, the MC and MEL responses in **Figures 2.7** and **2.8** can be examined using equation (4) and (5). The magnitude of MC is significantly smaller than MEL because of the following reasons. First, MC is a second order effect, while MEL appears in first order in ($1-R_S/R_T$). If $R_S \approx R_T$, MEL magnitude is generally larger than MC magnitude. Next, because the applied magnetic field does not act on the non-emissive excitons, T^1 and T^{-1}, free charge carriers dissociated from these states do not contribute to increasing the MC effect. In fact, the MC effect is about 50% smaller than that in equation (5), while MEL in the first order approximation is unaffected by the dissociation/recombination of these dark exciton states. Finally, η in our device structures is small due to the imbalance of positive/negative injected carriers and the small Coulomb binding energy. The small value of η may lead to a significantly small MC. Considering the sign of the MC and MEL effect,

the model predicts that MC is always negative while MEL is more likely to be negative since R_S is usually large than R_T for most HOIPs[100].

2.4 CONCLUSION

We studied the Rashba-type SOC in 2D $(BA)_2(MA)Pb_2I_7$ and 3D $MAPbI_3$ HOIPs using the MFE on the conductivity and the EL. We found that the MC magnitude in LEDs constructed with these HOIPs increases monotonically and saturates at a large current density. The MC follows the same trend as the ELQE of the device, while the MEL response remains almost unchanged and has similar shapes as the MC response, but with a significantly larger magnitude. This implies that the underlying mechanism of the MFE in the materials is excitonic. Notably, we found that the width of the MEL, or $\boldsymbol{B_{Rashba}}$, in these materials linearly increases with increasing the applied electric field. The Rashba coefficient in $(BA)_2(MA)Pb_2I_7$ HOIP is estimated to be about 7 times larger than that in $MAPbI_3$ HOIP. An excitonic model was developed to evaluate the MFE mechanism. We found that both sign and magnitude of MEL and MC responses can be explained through this model. An important prediction of our experimental results is that the Δg must be smaller under the effect of an applied electric field. Our studies may have a significant impact on future development of electrically-controlled spin logic devices via Rashba-like effects.

CHAPTER 3

OPTICAL STUDIES OF SPIN ORBIT COUPLING IN PEROVSKITE THIN FILMS

In this chapter, optical and magnetooptical complementary methods will be utilized to study the energy degeneracy splitting in 2D Ruddlesden-Popper and 3D $MAPbI_3$ HOIPs due to Rashba-Dresselhaus SOC magnetic field. First, complementary techniques, including circular dichroism (CD), circularly polarized luminescence (CPL), magnetic circular dichroism (MCD), and Faraday Rotation (FR) spectroscopies will be introduced. Then, our experimental results of CD, CPL, MCD and FR on HOIPs films will be discussed in detail. Finally, density functional theory (DFT) calculations will be used tosupport the experimental results.

3.1 CIRCULAR DICHROISM, CIRCULARLY POLARIZED LUMINESCENCE, MAGNETIC CIRCULAR DICHROISM, AND FARADAY ROTATION

Circular dichroism (CD) and circularly polarized luminescence (CPL) measure the difference in absorption and photoluminescence between the left and right circular light. CD and CPL are initially the methods of probing the molecule's ground and excited chiral electronic states, respectively.[101]

Figure 3.1 describes the setup for CPL measurement. The perovskite thin films were kept inside a cryostat at the desired temperatures (from 10K to room temperature) and were excited by a linearly polarized laser source at ~ 3.06 eV energy (405nm wavelength). The photoluminescence spectrum was focused into a spectrometer by using a concave mirror

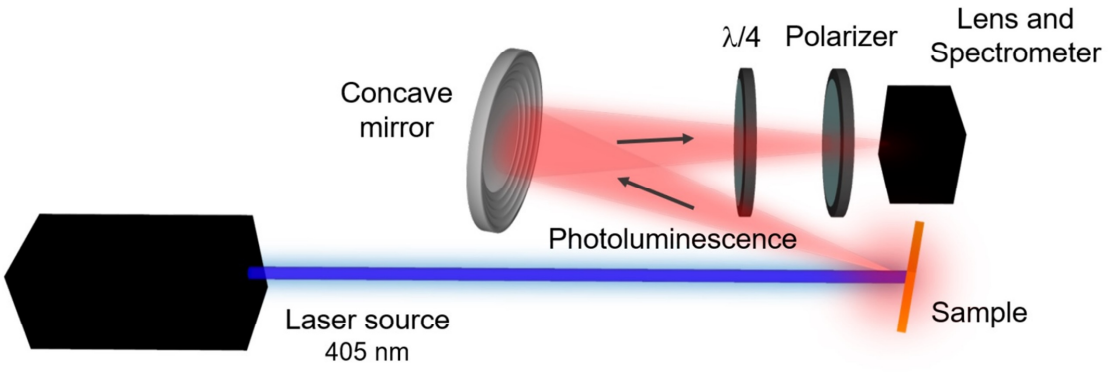

Figure 3.1. Circularly Polarized Luminescence (CPL) set-up

after passing through a quarter wave plate and a polarizer. The degree of CPL polarization (or emission dissymmetry factor) is defined as[102] :

$$P(\%) = \frac{I(\sigma^-) - I(\sigma^+)}{I(\sigma^-) + I(\sigma^+)} \quad (3.1)$$

where $I(\sigma^-)$ and $I(\sigma^+)$ is the photoluminescence intensity of the left circular light (LCL, σ^-) and right circular light (RCL, σ^+), respectively. PL intensities were calculated by integrating the PL curves in the PL-wavelength graph, i. e. $I = \int PL(\lambda)d\lambda$.

The circular dichroism (CD) and magnetic circular dichroism (MCD) of the perovskites thin films were measured by a home-built setup using a photo-elastic modulator (PEM) combined with a noise-reduction lock-in amplifier technique, which is illustrated in **Figure 3.2**. A Xenon lamp and monochromator provided a monochromatic and collimated light to the thin films at a normal incident angle. A polarizer was placed before the PEM to generate the left and right circular light. For MCD measurement, an out-of-plane applied magnetic

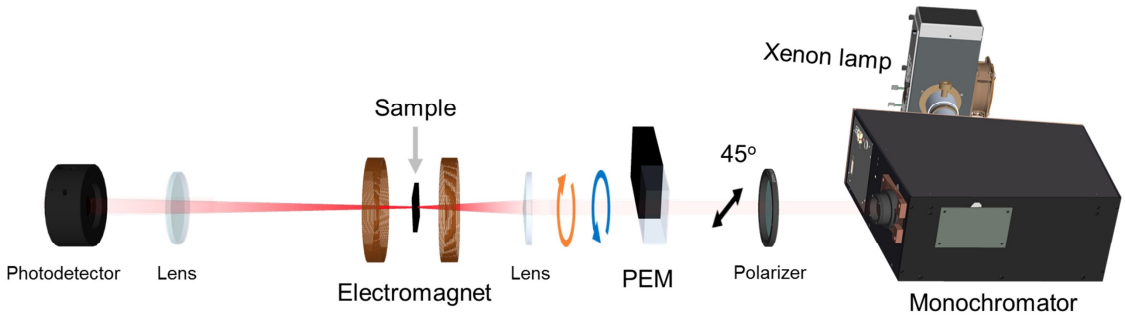

Figure 3.2. Circular dichroism and magnetic circular dichroism setup

field of 1.8T was created by an electromagnet. More details of the set up and measurement can be found in our works.[103-104]

CD and MCD can be represented in terms of ellipticity or anisotropy g factor.[105-106] Here, we present our results in ellipticity (milli degree, or mdeg). The ellipticity, in mdeg, is calculated from the equation:

$$\theta(mdeg) = \Delta A \left(\frac{ln10}{4}\right)\left(\frac{180000}{\pi}\right) \quad (3.2)$$

Where ΔA is the difference in absorption between left and right circular light.

FARADAY ROTATION

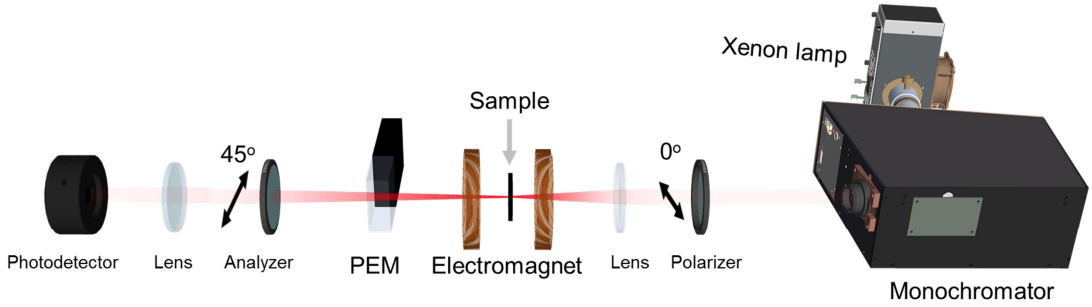

Figure 3.3. Faraday rotation measurement setup

Figure 3.3 presents the Faraday rotation setup, which is similar to the MCD setup. The difference is the addition of an analyzer and the PEM was placed after the electromagnet. The perovskite thin films' refractive indices were taken using a spectroscopic ellipsometer (M-2000, J. A. Woollam Co., Inc.) at incident angles of 65°, 70°, 75°, and 80°, respectively, over a wavelength range of 370 – 1000 nm.[107]

3.2 CIRCULAR DICHROISM, AND CIRCULARLY POLARIZED LUMINESCENCE OF HOIPS

Over the last decade, hybrid organic-inorganic perovskites (HOIPs) have emerged as excellent materials for applications in photovoltaic, optoelectronics, and spintronics owing to their superb properties including simple thin-film preparation from solution processing,[108] long carrier diffusion length[14], long carrier lifetime[13], large absorption coefficient[12], and strong spin-orbit coupling (SOC).[8, 109] Massive research efforts have been put forward to understand the material's properties.[14, 41, 110-111] Recently, the chiral 2D HOIPs have garnered attention from the spintronic research community because they potentially possess an extra degree of spin control by an applied electric field that enables chiral 2D HOIPs as promising materials for spin-logic devices such as spin transistor.[84, 102, 112-118] Optically, the spintronic properties of these chiral 2D HOIPs are usually studied by two complementary methods: circular dichroism (CD) and circularly polarized luminescence (CPL). The CD process originates with the structure in their thermally equilibrated electronic ground state, while the CPL process originates from the vibrationally relaxed electronic excited states.[101] Numerous interesting observation of CD and CPL in chiral 2D HOIPs has been reported. Long *et al*. observed a CPL of 3% in 2D chiral R- and S- methylbenzylammonium lead bromide ((R-MBA)$_2$Pb$_2$Br$_7$ and (S-

MBA)$_2$Pb$_2$Br$_7$) even in the absence of applied magnetic field.[113] Ma *et al*. reported a large CD of more than 100 mdeg and CPL of nearly 20% from the chiral 2D perovskites (R-MBA)$_2$PbI$_4$ and (S-MBA)$_2$PbI$_4$ at 77K.[114] In those chiral 2D HOIPs, large CD and CPL are attributed to the manifestation of "chirality transfer" from the chiral organic chains to the octahedral layer $[PbX_6]^{4-}$ where X is halide elements (Br or I).[36, 112, 117] Although "chirality transfer" is widely accepted and used to explained CD and CPL in others chiral organic-inorganic system e.g. chiral molecules- Quantum Dot (QD)[119], chiral molecules – colloidal perovskite nanoplatelets[120] and chiral perovskites[36, 112, 117], there remain some open questions. In the work from Ma. *et al*.[114], a large degree of polarization from CPL measurement was observed in chiral perovskites (R-MBA)$_2$PbI$_4$ and (S-MBA)$_2$PbI$_4$ by using the 473 nm laser excitation. This excitation energy is not enough to excite the chiral molecules to excited states. Therefore, there is absolutely no polarized electron or hole transferred from chiral molecules to the excitonic transition of perovskites octahedral layer $[PbI_6]^{4-}$.[114] Moreover, CD and CPL were also observed in monolayer,[121] 2D heterostructure of transition metal dichalcogenides,[122] and non-chiral quantum dots and nanorods.[123] Therefore, whether "chirality transfer" is the only reason for the large CD and CPL is not known. Recently, Sercel *et al*.[124] theoretically demonstrated that non-chiral orthorhombic perovskite lead layers can exhibit large extrinsic circular dichroism (CD) in the absence of an applied magnetic field. In this work, non-chiral materials might exhibit extrinsic chiral behavior when interacting with light. The circularly polarized dependent absorption is caused by the combined effect of strong Rashba-Dresselhaus splitting (Zeeman splitting caused by Rashba-Dresselhaus magnetic field in the order of 10 T), in-plane symmetry breaking, and the effect of the exciton momentum on its fine structure. However, circularly

polarized spectroscopies that are used to establish the relationship between the inversion asymmetric structures, Rashba-Dresselhaus SOC, and circularly polarized response in non-chiral HOIPs has not been reported in the literature.

In this chapter, we systematically study the CD and CPL of non-chiral 2D Ruddlesden-Popper Perovskites $(BA)_2MA_{n-1}Pb_nI_{3n+1}$ with n = 1, 2, and 3 and 3D $CH_3NH_3PbI_3$ ($MAPbI_3$) (n = ∞). Remarkably, we observe a giant CD ~ 100 mdeg at room temperature and CPL ~ 4.8% at 10 K and ~2.8% at 293 K from the 2D Ruddlesden-Popper (RP) perovskite thin film with n = 1 in the absence of an applied magnetic field. However, the measured CD and CPL signals are an order of magnitude smaller in the RP perovskite thin film with n = 2 and are not detectable for the perovskite thin films with n = 3, and n = ∞. Our observation indicates that there is a mechanism other than "chirality transfer" that causes the giant CD and CPL in these 2D HOIPs.[124] We hypothesize that the strong observed CD and CPL are associated with the strong Rashba-Dresselhaus splitting in the 2D RP perovskite superlattices due to strong lattice distortions at the organic/inorganic interface: more interfaces leads to more distortions, and thus, larger Rashba-Dresselhaus splitting.[124] This hypothesis is confirmed by density functional theory (DFT) calculations where the inter-layer distortions of the superlattices leads to the major Rashba-Dresselhaus splitting. To quantify to magnitude of the Rashba-Dresselhaus effect, we conduct magnetic circular measurement and estimate the Rashba-Dresselhaus effective magnetic field in 2D RP perovskites with n = 1 ~ 500mT. From our perspective, these results establish CD, MCD and CPL as new methods to evaluate the Rashba-Dresselhaus SOC strength.

3.3 RESULTS OF CIRCULAR DICHROISM, AND CIRCULARLY POLARIZED LUMINESCENCE OF 2D RUDDLESDENCE POPPER HOIPS

Morphology characterizations

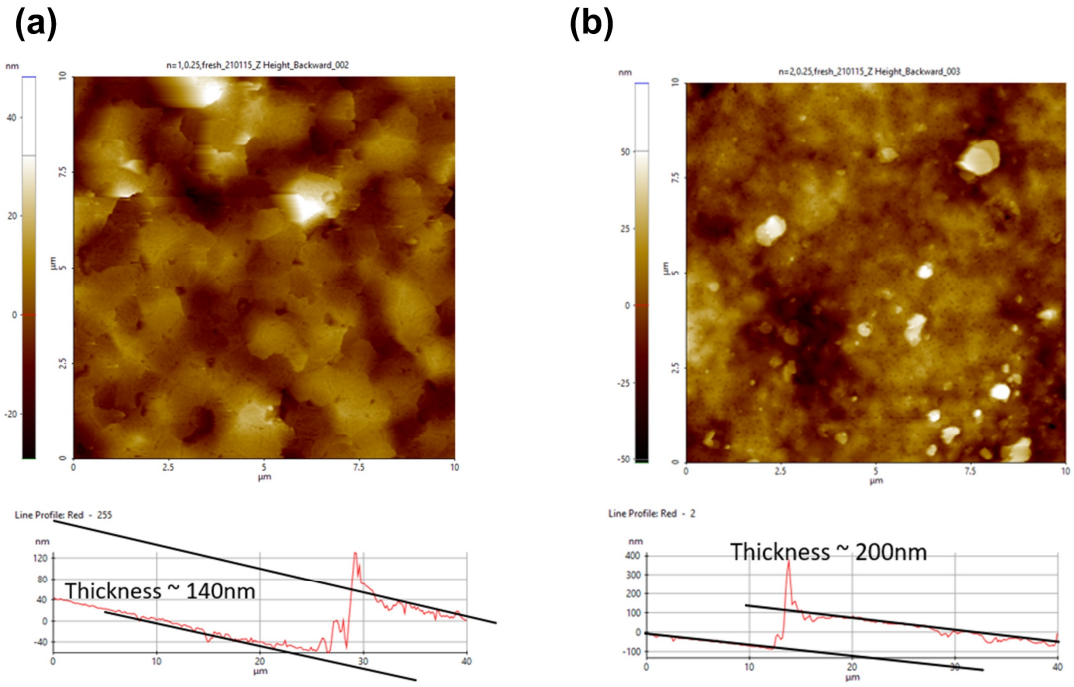

Figure 3.4. Atomic Force Microscope images of 2D RP HOIPs thin films with n = 1 (a) and n = 2 (b). The thicknesses of the films were extracted are 140 nm and 200 nm for n = 1 and n = 2 thin films, respectively.

The structure of the 3D $MAPbI_3$ perovskite and 2D RP perovskites are shown in **Figure 1.1** and **Figure 1.3**, respectively. At room temperature, the $MAPbI_3$ crystal presents the tetragonal phase with a space group of *I4/mcm*[16], while the 2D RP perovskites have orthorhombic structure with C_{2v} symmetry.[21] Such crystallographic structure can be characterized by the X-Ray Diffraction (XRD), and the results are shown in **Figure A1**, **Appendix A** confirm a successful fabrication process that yields the same crystal structure

as reported.[20-21] It is noteworthy to mention that for the 2D RP n = 1 thin film, the XRD pattern demonstrates well-defined diffraction peaks corresponding to the {00*l*} family of planes, indicating the formation of a highly oriented inorganic layer parallel to the substrate. From n = 2 and 2D RP thin films of larger n, the present of MA^+ cation leads to a dramatic change in the crystal structure. With n = 2, the XRD pattern shows diffraction peaks with the {0*k*0} family of planes that reveal the vertical growth of the compound with respect to the substrate plane.[20] Both 2D RP HOIP thin films with n = 1 and n = 2 are phase pure. However, with n = 3, the XRD pattern shows the presence of two different families of planes, that is, {0*k*0} and {111}. This indicates that the 2D RP n = 3 thin film is composed of quantum wells with n = 2 and n = 3.[125] **Figure 3.4** shows the AFM images of 2D RP perovskites with n = 1 and n = 2. The domain area in the n = 1 thin film is quite large, up to 1 μm^2. The thickness of the 2D RP perovskite thin films from AFM measurement are 140 and 200 nm for n = 1 and n = 2, respectively.

Circularly Polarized Luminescence Studies

Figure 3.5 shows the PL spectra from LCL (σ^-) and RCL (σ^+) of the 2D RP perovskite with n=1 at 10K. PL spectra recorded with various temperatures from 10 – 293 K (room temperature) (**Figure 3.6**) were consistent with those reported by literature[19, 21]. Blancon *et al.*[22] reported that in 2D RP perovskites, due to the strong dielectric confinement, excitons exists in the Rydberg states series of the Wannier-Mott exciton. At 10 K, the largest peak in the PL spectrum of 2D RP perovskites n = 1, which is located at 2.52 eV (491 nm), is attributed to the lowest energy 1s Rydberg state.[22] The second PL peak which appears at 2.39 eV (518 nm) is indeed the room temperature phase feature which still exists at low temperature. In our previous report, the optical absorption taken at

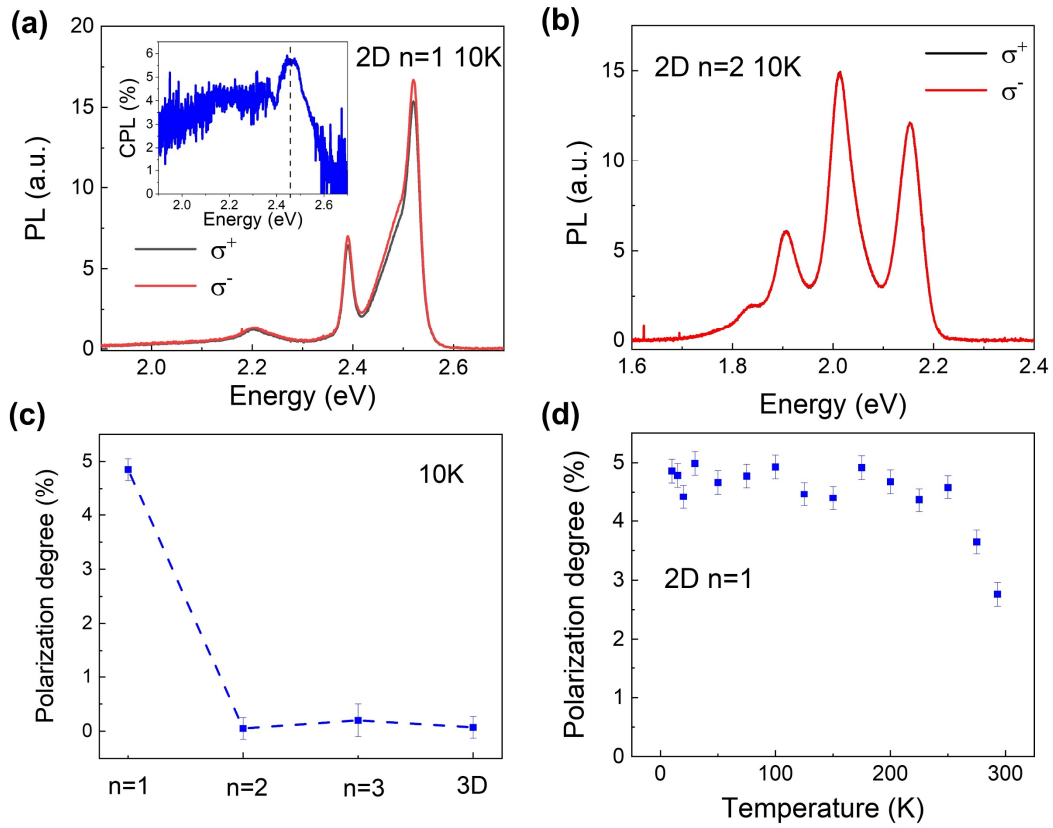

Figure 3.5. Circular Polarization Luminescence (CPL) of 2D RP perovskite with n=1 (a) and n=2 (b) at 10 K. (c) Polarization degree (%) of all 2D and 3D perovskites at 10K. (d) Polarization degree (%) of 2D Perovskite n=1 at various temperatures.

various temperatures indicated the coexistence of two distinctive phases in the 2D RP n = 1 thin film which were attributed to the sudden reduction of the inter-layer spacing at approximately 250 K.[126] The long tail in PL spectrum at ~2.2 eV which shows up only at temperature less than 100 K is attributed to the self-trapped exciton or in-gap states.[127] At room temperature, there is only the PL peak which appears at 2.37 eV and corresponds to exciton resonance identified from absorption measurement with a slight Stokes shift of 0.05 eV.[125] (see absorption spectra, **Figure A2**, **Appendix A**) The difference of PL intensity between the two circularly polarized light is obvious and is largest, ~5.6 %, at the

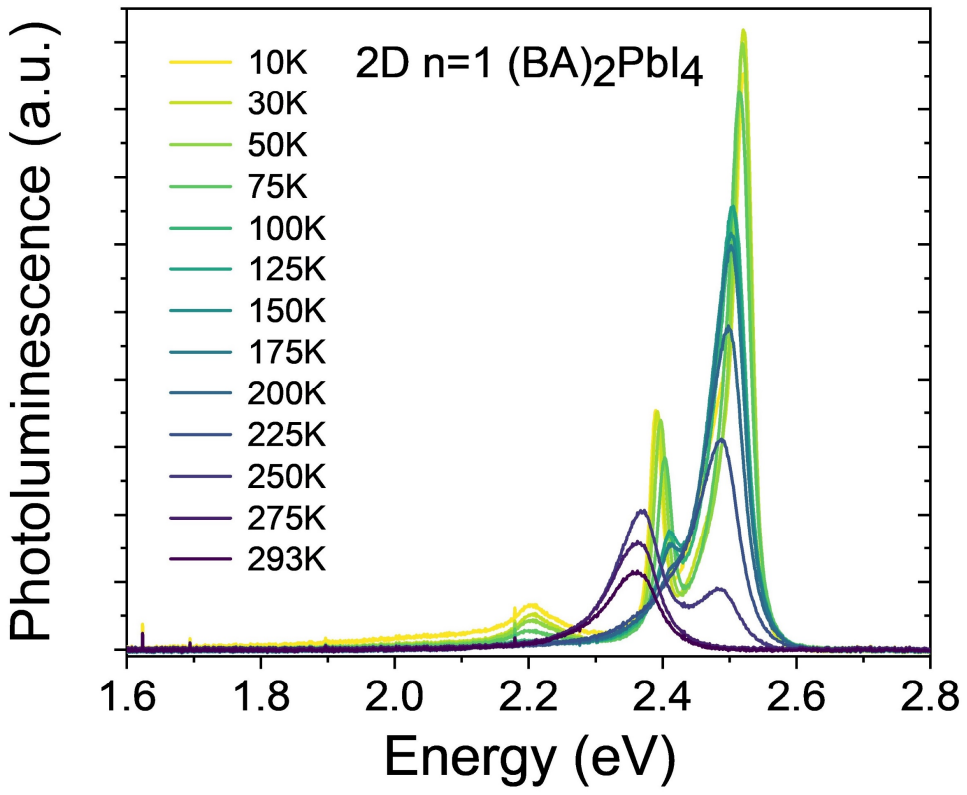

Figure 3.6. PL of 2D RP n = 1 thin film at various temperature in the range 10 - 293 K.

PL shoulder ~2.46 eV(**Figure 3.5a**, inset), where the degree of polarization at a certain wavelength λ is calculated in **Equation 3.1**. The degree of polarization of whole spectrum, observed in the absence of applied magnetic field, is ~4.8%, which is ~1.6 times larger than that from the reduced-dimensional chiral perovskite at 2K[113]. More recently, Ma *et al.* reported a huge CPL up to 17% from chiral $(S\text{-}MBA)_2PbI_4$ at 77K.[114] When the number of lead halide octahedral layer $[PbX_6]^{4-}$ in the wells of RP perovskites increases, the degree of polarization is again substantially quenched. From **Figure 3.5b**, the degree of polarization of the 2D RP perovskite with n = 2 and n = 3 is ~0.05% and ~0.3% at 10K, respectively. When n = ∞ (3D $MAPbI_3$), the degree of polarization is ~0.07%. The CPL at

10K of all perovskites thin film is summarized in **Figure 3.5c**. The CPL experimental error of ~0.2% (occurs when the polarizer is rotated between +45 and -45 degree) is determined by a control experiment with an anisotropic PL from an organic semiconductor thin film made of tris(8-hydroxyquinolinato) aluminum (Alq_3, **Figure 3.7**). We conclude that all measured values of CPL of 2D RP thin film with $n \geq 2$ is within the noise level of the instrument.

Due to the unexpected large CPL value of the 2D RP perovskite with n = 1, we carefully studied the CPL in this thinnest superlattice with various temperatures. **Figure 3.5d** shows the temperature dependence of CPL. The degree of polarization of the whole

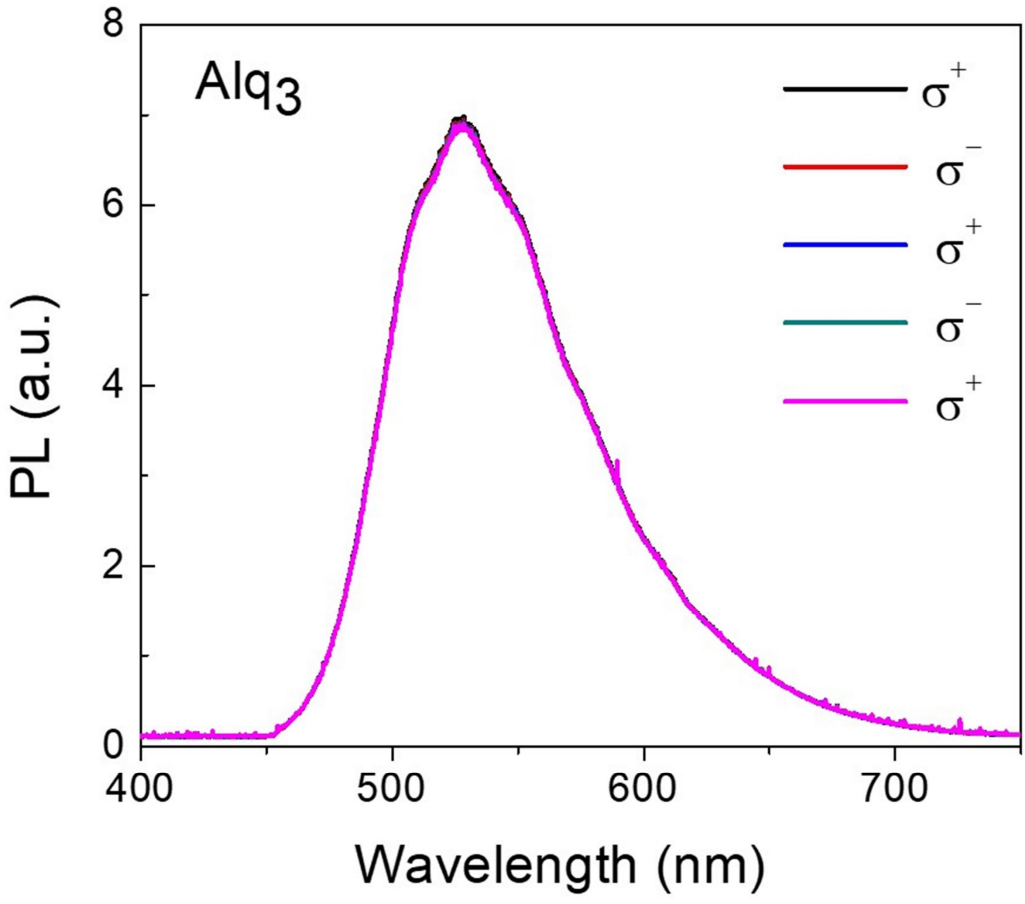

Figure 3.7. Control experiment CPL of Alq3

PL spectrum was remained around 4.5% in the temperature range of 10K to 250K and only started to decrease sharply when the temperature exceeded 250K, at which the structural phase transition occurs.[126] At 275 K and room temperature, the degree of polarization drops from ~ 4.5 % to 3.6 % and 2.7 %, respectively. We speculate that the reduction of the CPL above 250 K is associated with the expansion of the organic inter spacing which causes the reduction of Rashba-Dresselhaus SOC strength.[126] This hypothesis is verified by the DFT calculations in the DFT Calculations Section.

To further investigate the polarization of PL, the degree of polarization each PL peak was calculated. The results (**Figure 3.8**) show that all the PL peaks at low temperature

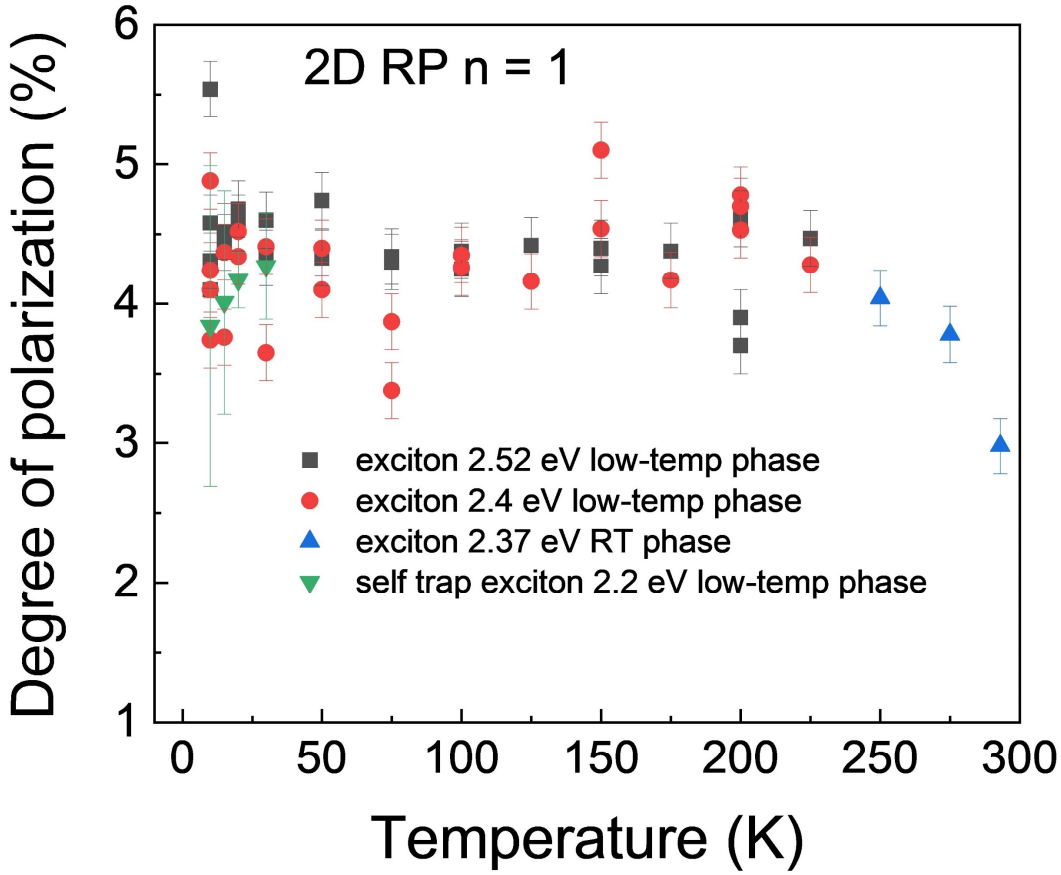

Figure 3.8. Degree of polarization of each exciton at various temperature in the range 10 K – 293 K.

(2.52 eV, 2.4 eV and 2.2 eV) have a degree of polarization ~ 4.4 %. Meanwhile the polarization of the PL peak at higher temperature phase (at 2.37 eV) drops when temperature increases, which has a similar trend shown in **Figure 3.5d**. We note that such sharp decrease in CPL at phase transition temperature was also observed in a previous study when $MAPbI_3$ and $MAPbBr_3$ thin films were pumped with circularly polarized light (Hanle effect).[128] However, it is noteworthy that in their work, the authors did not observe CPL when using linear polarized excitation. It is surprising that the degree of polarization of 2D RP perovskite in the low temperature phase does not depend on temperature as previously reported in chiral Perovskites[114], where the degree of polarization decreased monotonically from 17% at 77K and vanished at room temperature. This implies that the mechanism of CPL in this 2D RP n = 1 perovskite thin film is sensitive to the crystal structure of the material. In the next section, we show the results of the complementary CD studies on investigating the electronic structures of the perovskite superlattices. While CPL is used to study the difference of left and right circular light in emission from excited states, CD is used to study their difference in absorption from ground states.[101] The information obtained from CD and CPL spectra might reveal the structural change in the material is in its ground state and emitting state.

Circular Dichroism Studies

Figure 3.9a and **3.9b** show the CD spectrum (red lines) of the 2D RP perovskites with n = 1 and n = 2, respectively. Interestingly, the CD shapes of both the two thin films are very well-fit with the derivative of absorption spectra (blue lines). CD's ellipticity measured from the 2D RP perovskite with n = 1 reached ~100 mdeg (peak-to-peak magnitude) at the exciton resonance (2.42 eV) which is surprisingly larger than those

previously reported from chiral perovskite thin films.[112-113, 117] We note that in the absorption spectrum of the 2D RP n = 1, there is also a gradual rise in the absorption signal at energies of 2.6 to 2.8 eV, which is attributed to the band gap continuum.[125] However, no trace of CD was observed within the measurement resolution of 0.1 mdeg. This indicates that the observed CD here is associated with the excitonic absorption. When the number of $[PbI_6]^{4-}$ layer is double with n = 2, CD's ellipticity was quickly reduced to 8 mdeg. Similar to the n = 1 film, the derivative-like CD in the n = 2 film associates with the highest excitonic absorption peak at 2.18 eV. There is a tiny CD of ~ 0.5 mdeg appearing around

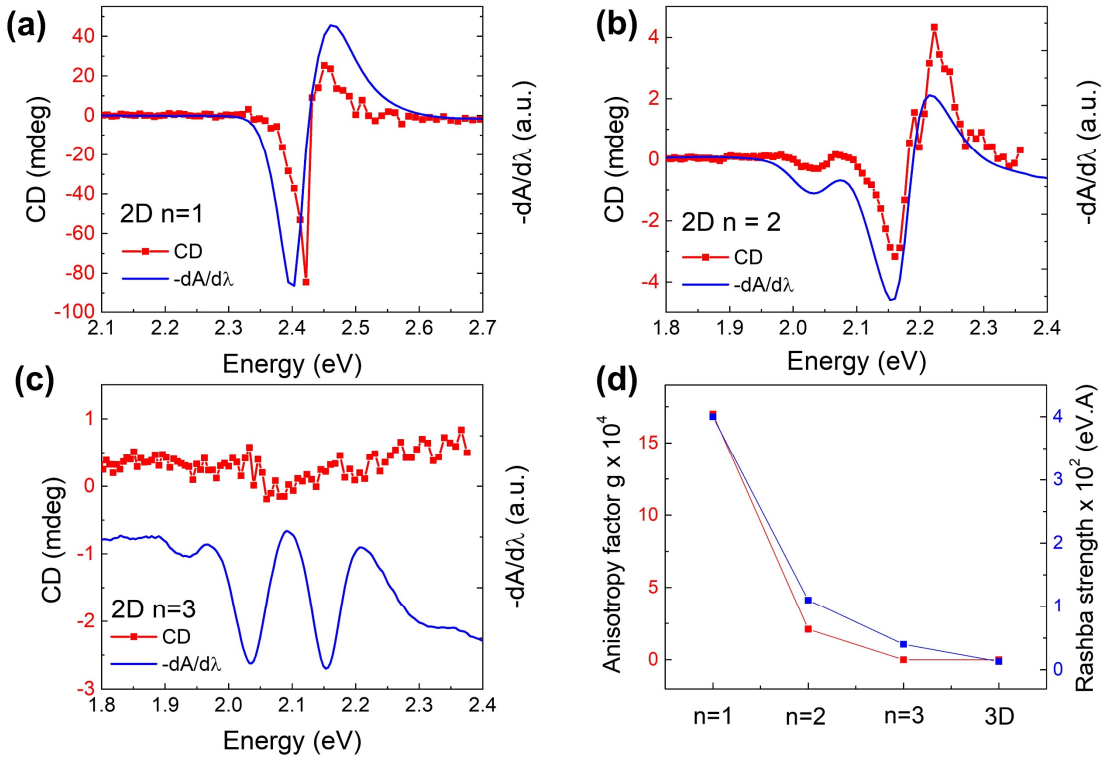

Figure 3.9. Circular dichroism (CD) and derivative of absorption spectra (red and blue lines, respectively) of the 2D Ruddlesden-Popper $(BA)_2MA_{n-1}Pb_nI_{3n+1}$ with n = 1 (a), n = 2 (b), and n = 3 (c). (d) Magnitude of CD of all the 2D and 3D HOIPs with the Rashba strength calculated from second harmonic generation from Yu's work.

2.05 eV, where a smaller a peak present in the absorption spectrum. This small absorption peak was attributed to the exciton resonance for a mixed-phase 2D RP HOIPs thin film comprising of n = 2 and n = 3. This contradiction between absorption and XRD results, which indicated that the thin film is comprising only the quantum well with n = 2, were pinpointed in our previous work.[125] We note the CD rather than the CPL were observed in the superlattice with n = 2 due to the increased sensitivity of the former which is granted by the high-frequency modulation and lock-in detection. Apart from these band-edge features, the CD of both the n = 1 and n = 2 2D RP perovskites thin films is quenched to zero which is clearly different from the CD spectra of chiral perovskites.[112-113] For the 2D RP perovskite with n=3 thin film, we did not observe any trace of CD to the resolution of 0.1 mdeg even at the exciton resonance 2.0 eV which agree with the CPL study (**Figure 3.9c**). In the absorption spectrum of the thin film, we observed very small peaks at 2.05 eV and 2.18 eV, which are attributed to the resonance from $(BA)_2(MA)_2Pb_3I_{10}$ and $(BA)_2(MA)Pb_2I_7$ quantum wells. The weak excitonic resonance in this thin film might be the consequence of weaker Coulomb interaction due to the increasing in quantum well thickness. Moreover, comparing to other 2D RP thin films, the 2D RP with n = 3 has the most phase heterogeneity.[125] Similar to the 2D RP perovskite with n = 3, no trace of CD more than the measurement's resolution was observed from the 3D perovskite thin film.

Noticeably, the CD signal in these RP perovskites has a derivative-like feature ($-\frac{dA}{d\lambda}$) of the corresponding material absorption spectrum, A (see blue lines, **Figure 3.9**). This characteristic is analogous to the magnetic circular dichroism (MCD) where applied magnetic field causes Zeeman splitting and diamagnetic shift that modify the optical transition of LCL and RCL.[22, 129-130] This implies that there is an intrinsic internal magnetic

field inside material, which strongly depends on the width of the superlattice or quantum well. Our result is in agreement with the recent theory proposed by Sercel *et al.*[124] where non-chiral orthorhombic perovskite lead layers can exhibit large extrinsic circular

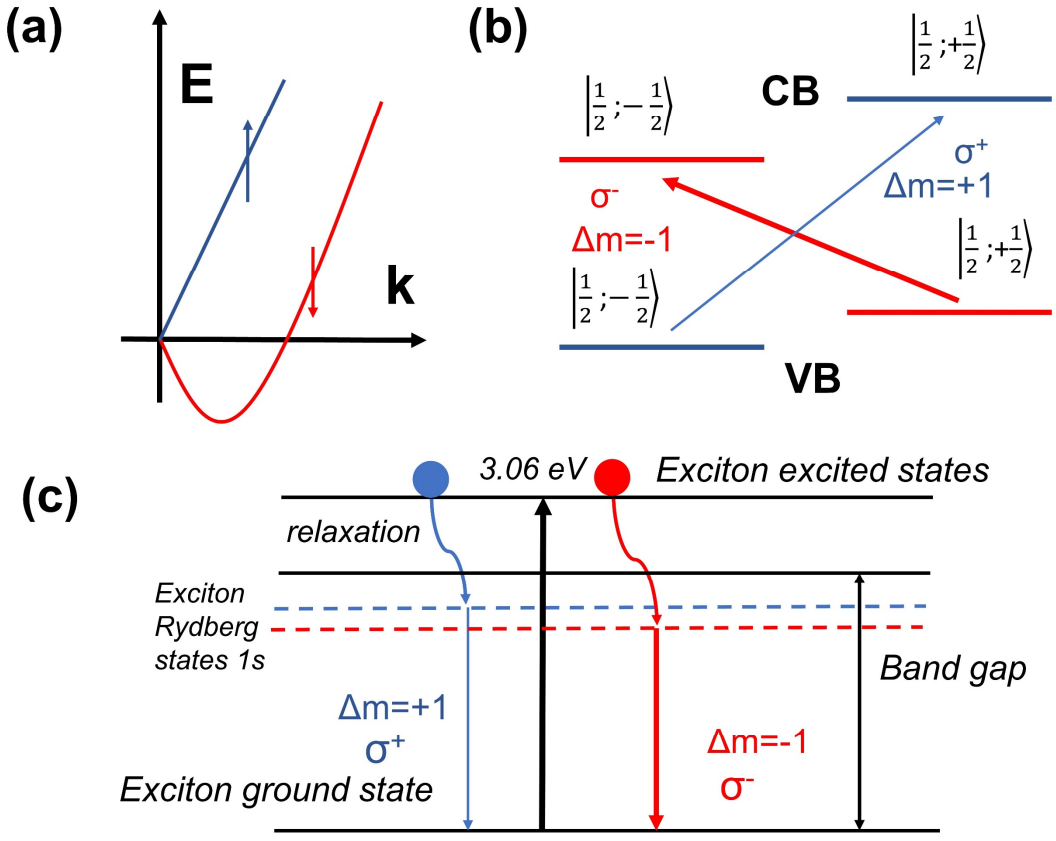

Figure 3.10. (a) Energy splitting due to Rashba-Dresselhaus effect at the bottom of conduction band. The parabola was split into two branches corresponding to opposite spin orientations. (b) Optical selection rules for the absorption at the band gap. The red and the blue arrows demonstrate the absoption of the left and right circular light, respectively. The thicker line indicates the stronger absorption. (c) Exciton energy level picture in photoluminescence process.

dichroism (CD) in the absence of an applied magnetic field due to the presence of strong Rashba-Dresselhaus magnetic field in the order of 10 T.

There was concrete experimental evidence that proves the existence of a giant Rashba-Dresselhaus effect in the 2D HOIPs. Using the transient spectroscopy technique, Zhai *et al*. estimated the magnitude of the energy splitting of 40 meV and Rashba parameter of 1.6 eV•A in 2D Ruddlesden-Popper HOIPs $(C_6H_5C_2H_4NH_3)_2PbI_4$ (2D-PEPI). Liu *et al.* observed the circular photogalvanic effect in 2D-PEPI and confirmed the energy splitting due to Rashba effect is 35 ± 10 meV.[131] **Figure 3.10a** illustrates the splitting of energy levels of the two spin in energy - momentum dispersion relation graph at the conduction bands' minimum of HOIPs.[37] The origin of the spin dependent energy splitting comes from the effective Rashba-Dresselhaus magnetic field[34-35, 132]induced by the bulk inversion asymmetry (BIA) and/or structure inversion asymmetry (SIA) in the crystal. In the 2D RP perovskites crystal, there might be a few mechanisms that could simultaneously contribute to the effective Rashba field: First, the structures of the 2D RP perovskites crystal are orthorhombic point group. This symmetry is a low symmetry and lack of bulk inversion symmetry that theoretically gives rise to Dresselhaus magnetic field.[21] Second, the discrepancy of dielectric constant between the organic chain BA^+ layers and the inorganic lead halide octahedral $[PbI_6]^{4-}$ layers[22] induces an electric field at the interface of the two layers.[22] In other words, the dielectric confinement effect in 2D RP perovskites crystal gives rise to SIA or Rashba magnetic field. We note that the Dresselhaus and Rashba fields (denoted as Rashba-Dresselhaus field) might coexist in the perovskites. Moreover, another mechanism also suggested in some theoretical and experimental works are the dynamics of the MA cation[26, 28] and the distortion of the inorganic lead halide octahedral $[PbI_6]^{4-}$

lattice due to the dynamics of organic cations.[26, 36, 133] The latter has been proven to be the cause of large Rashba-Dresselhaus splitting in the studied superlattice (see our DFT calculations below).

To understand the observed CD mechanism, a simple picture of electronic states of electrons and holes at the top of valence band (VB) and bottom of conduction band (CB) in HOIPs is shown in **Figure 3.10b**. In HOIPs, the conduction band bottom has the states with total angular momentum J=1/2 (J=L+S, with L=0 and S=1/2), whereas the top of valence band has states with spin angular momentum S=1/2. [113, 128, 134-137] The transition between states from valence band to conduction band for the circularly polarized light needs to satisfy the optical selection rule $\Delta m_J = \pm 1$. The carriers (electrons or holes) with opposite spin direction have different energy levels, due to the splitting caused by Rashba-Dresselhaus magnetic field. The derivative-like feature of the CD spectrum was due to the shifted of the absorption peaks from the left and right circular light, which stems from the energy splitting from Rashba-Dresselhaus field demonstrated in **Figure 3.10b**. Moreover, the CD spectrum is asymmetric, which is due to the different absorbance of the left and right circular lights at their corresponding peaks. The absorption rate is governed by the Fermi's golden rule:

$$W = \frac{2\pi}{\hbar}\left|\langle\psi_i|H|\psi_f\rangle\right|^2 \delta\left(E_f - E_i - \hbar\omega\right) \quad (3.3)$$

where W is the transition probability, which is proportional to the absorption rate. E_i and E_f are energy level of initial and final states of electron at valence and conduction band, respectively. $\left|\langle\psi_i|H|\psi_f\rangle\right|$is transition matrix element, where ψ_i and ψ_f are wavefunctions of electron of the unperturbed initial and final state. ω is the frequency of the photon. H is the Hamiltonian of an electron. When considering the effect from Rashba-Dresselhaus

SOC, one needs to include the Rashba-Dresselhaus Hamiltonian term[35]: $H_{SO} = \alpha [\boldsymbol{\sigma} \times \boldsymbol{k}] \boldsymbol{\nu}$ where α is the Rashba coefficient, $\boldsymbol{\sigma}$ is the Pauli matrix and $\boldsymbol{\nu}$ is the unit vector perpendicular to the plane that electron is confined. In **Equation 3.3**, a large transition rate is directly associated with a large α coefficient or Rashba-Dresselhaus splitting. This indicates that the superlattice with n = 1 is expected to have the largest Rashba- Dresselhaus effect corresponding to its large exitonic oscillator strength. In addition, due to the effect of the Rashba-Dresselhaus term in the Hamiltonian, the two opposite spin states would have different transition probabilities, which leads to the observed CD in 2D RP perovskites thin films. Details in the calculation of Rashba splitting and CD in HOIPs can be found from the theoretical work of Kepenekian *et al.*[37] and Sercel *et al.*[124].

Figure 3.10c depicts the PL from RCL and LCL in the exciton energy picture. The red and blue circles are the exciton corresponding to the helicity of +1 and -1. After its creation when the electron from conduction band absorbs a photon with helicity +1 (or -1), exciton at the excited states relax to the 1s state, the lowest energy exciton in the Rydberg states. The Rydberg exciton states are usually observed in the low dimension semiconductor[138], where the Coulomb interaction between electron and hole are enhanced. The strongest PL peak in 2D RP perovskites is indeed the luminescence from the 1s Rydberg state.[22, 139] The exciton with helicity of +1 and -1 come back to the exciton ground state by emitting a right and left circular light, respectively. Due to the discrepancy of transition matrix element original from Rashba-Dresselhaus SOC term, the two emissions have different emission rates, which is reflected in the CPL results. There is experimental evidence for the formation of helical excitons in 2D RP single crystal by using high-resolution and angle-dependent spectroscopic ellipsometry.[140] We note that the two exciton

states with different helicity have different energy levels, but the splitting is too small to be observed by PL spectroscopy and needs to be studied by a more sensitive technique.

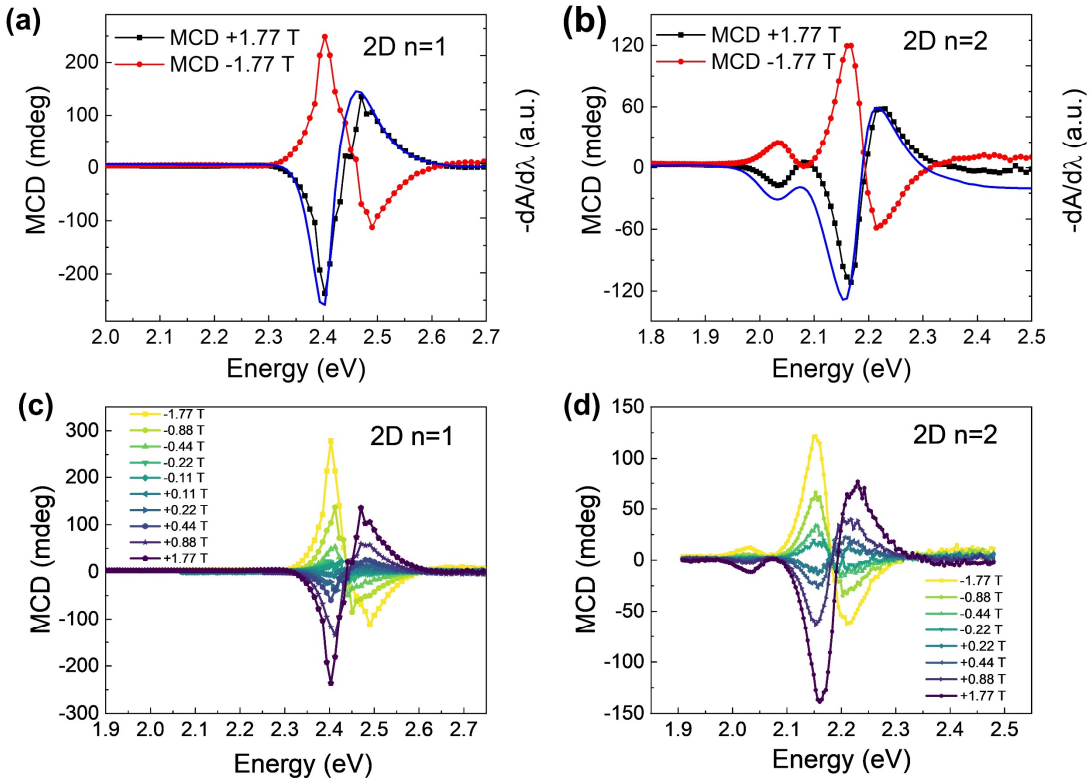

Figure 3.11. Magnetic Circular Dichroism (MCD) spectra of the 2D RP perovskites thin film with n = 1 (a) and n = 2 (b) under applied magnetic fields of ±1.77 T. All materials showed the derivative-like features at absorption peaks. MCD with various applied magnetic field B of 2D RP perovskites thin films with n = 1 (c) and n = 2 (d).

To understand the nature of the internal field and estimate the effective Rashba-Dresselhaus magnetic field strength, the MCD study is performed. **Figure 3.11a** shows the MCD spectra of the 2D RP with n = 1 under the applied magnetic field of +1.77 T, -1.77 T. The two curves present derivative-like feature $(-\frac{dA}{d\lambda})$ and are symmetric about the x-axis, which is normally observed in magnetic circular dichroism spectroscopy.[129-130] We

note that both of the peak and dip from CD and MCD spectra of the 2D RP perovskite thin film with n = 1 appear at almost the same locations corresponding to the two Gaussian peaks (2.39 and 2.45 eV) from the fitting of absorption line (**Figure 3.12**). These two peaks are widely observed in 2D RP perovskites and assigned to the exciton 1s level and the exciton 1s coupling to phonon.[141-142] There are noticeably small shifts in peak position of the CD spectrum and MCD spectrum in n = 1 film (in **Figure 3.9a** is located at 2.42 eV and 2.45 eV. Meanwhile, the peak and dip of MCD spectrum in **Figure 3.11a** is presented at 2.40 eV and 2.47 eV, respectively). However, we point out that the effect from Zeeman splitting is much smaller than the 20 meV shift here[22, 141]. One can estimate the splitting energy due to Zeeman effect by the Gaussian fitting method.[117, 143-145] The splitting energy is:

$$\Delta E_{Zeeman} = \frac{2\sigma\Delta A}{A} \quad (3.4)$$

where σ is the halfwidth of Gaussian fitting curve from absorption spectrum, ΔA and A are the CD (MCD) and absorption intensity at the excitonic transition, which can be obtained

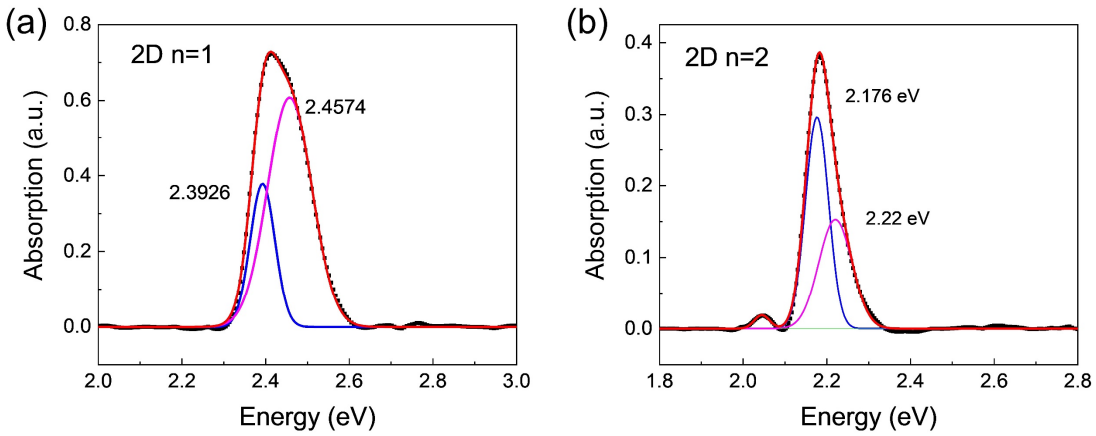

Figure 3.12. Gaussian fitting of absorption spectra of 2D RP HOIPs n = 1 (a) and n = 2 (b).

from **Figures 3.9a and 3.11a**, respectively. From **Equation 3.4**, we calculate Zeeman

splitting energy in 2D RP n = 1 under external B = + 1.77 T is ~ 0.3 meV. **Figures 3.11c and 3.11d** present the MCD spectra of the 2D RP thin film with varied applied field B. Using **Equation 3.4** and the MCD results from **Figure 3.11c** and **3.11d**, one can estimate the Zeeman splitting energy and deduce a g factor of 2.8 and 3.1 for the 2D RP perovskite thin film with n = 1 and n = 2, respectively. More details of the calculation can be found in **Appendix B**. The g-factor values are in agreement with a recent report of g factor of 2D RP perovskite from MCD measurement.[146] **Figure 3.11c** shows the MCD of the 2D RP n = 1 thin film with various applied B. We observed that the MCD is linearly dependent on the applied magnetic field B. With the same magnitude of applied B (and opposite direction), the MCD magnitude results in similar values, for example, with B = ± 1.77 T, MCD magnitudes at 2.4 eV are 236 and 248 mdeg. This is surprising, because one might expect to see an asymmetry feature of MCD due to a huge CD peak magnitude ~ 85 mdeg value observed at 2.4 eV, when the applied B = 0. Even with a small applied magnetic field,e.g 0.22 T, the MCD magnitude of 40 mdeg still follows the linear dependent trend and is much smaller than CD magnitude. A plausible scenario may be that the applied magnetic field B, even when small, can "erase" the effect of the relativistic Rashba-Dresslhaus field. Electrons and holes with a velocity v under an applied magnetic field B, will feel a real Lorentz force. Since the direction of applied $\vec{B}$ is fixed (perpendicular to the quantum well plane), the Lorentz force makes electrons and holes's trajectory a cycle in the quantum well planes, which leads to a zero $\vec{v}$ average of electrons and holes. Therefore, the effective Rashba-Dresslhaus field is zero.

From **Equation 3.4**, for 2D RP perovskites with n = 1 $\Delta E_{Zeeman\ CD}/\Delta E_{Zeeman\ MCD} = \Delta A_{CD}/\Delta A_{MCD\ (1.77\ T)}$ = 100 mdeg/360 mdeg = 5/18. Since $\Delta E_{Zeeman} = g.\mu_B.B$, where g is the

g-factor, μ_B is the Bohr magneton (5.788 eV. T^{-1}) and B is the magnetic field that induces the splitting. Therefore, $B_{CD}/B_{MCD} = \Delta E_{Zeeman\ CD}/\Delta E_{Zeeman\ MCD}$, and we can estimate the B_{CD} or internal Rashba-Dresselhaus magnetic field effect in the range of 400 mT~ 500 mT. **Figure 3.11c** The MCD under the applied B = ±0.44 T (440 mT) also shows an equivalent magnitude to that of CD. We note that the CD/MCD magnitude ratio strongly depends on the morphological characteristics of the films e.g crystal orientation, grain size, defect density, etc. For example, the CD magnitude and spectrum's shape of chiral perovskites thin film strongly depends on fabrication details such as the precursors' solution concentration, as reported by Ahn *et al.*[112] There is a large difference in our estimation of the RD magnetic field of 500 mT in comparison to the calculation from Sercel *et al.*, where the Rashba-Dresselhaus magnetic field in 2D perovskite $(PEA)_2PbI_4$ (PEA = $C_6H_5(CH_2)_2NH_3$) was estimated ~ 24 T.[124] Experimentally, our optical spot size (~ 1 cm^2) is several orders of magnitude greater than the average grain size within the polycrystalline thin film (~ 1 μm^2, **Figure 3.4**). There is a nonuniform distribution of grain orientations and therefore opposing orientation Rashba-Dresselhaus magnetic fields cancel one another in our observed CD signal. That leads to such a significantly smaller magnitude in comparison to that of Sercel's work, in which the RD magnetic field was calculated locally. **Figure 3.11b** shows the MCD measurement of the 2D RP perovskite with n=2. The peak and dip of both the CD and MCD appear at 2.2 eV and 2.16 eV, respectively. Besides this main peak and dip, there is a very small peak at 2.03 eV observed in both CD (peak magnitude ~ 0.7 mdeg) and MCD (peak magnitude ~ 24 mdeg under applied -1.77 T) spectra. This small peak is from the effect of an absorption shoulder at 2.05 eV, which originates from the mixed phase of the 2D RP perovskite with n = 3.[125] The Gaussian fitting

of the absorption line is shown in **Figure 3.12**. The ratio of CD and MCD magnitude is 8 mdeg/ 171 mdeg ~ 0.047 that leads to the estimated Rashba-Dresselhaus magnetic field in 2D RP perovskite with n = 2 is ~ 83 mT.

Figure 3.9d presents the anisotropy factor *g* that calculated from CD ellipticity with the Rashba strength coefficients of the 3D and 2D perovskites from Yu's theoretical work.[96] The anisotropy factor is the ratio of CD ellipticity calculated by the equation:

$$g_{abs} = \frac{A_L - A_R}{(A_L + A_R)/2} \qquad (3.5)$$

Where A_L and A_R are the absorbance of the left and right circular light, respectively. Since the difference $\Delta A = A_L - A_R$ is very small in comparison to A_L and A_R, then $g_{abs} \approx 2\Delta A/A$, where A is the absorbance of the material. The anisotropy factor of the 2D perovskites is the highest, ~17 x 10^{-4}, when the inorganic layer is 1, then quickly drops to 2 x 10^{-4} when the number of inorganic layers n is double. With n = 3 and ∞ (3D), no CD was observed, then g(n=3) and g(3D) = 0. Our anisotropy g factor trend is in good agreement with the Rashba strength coefficient's trend that Yu estimated from second harmonic generation conforming that the origin of large CD and CPL in RP HOIPs is associated with the strong Rashba-Dresselhaus effects.[96]

3.4 DENSITY FUNCTIONAL THEORY CALCULATION

In this part, Density Functional Theory (DFT) calculation is performed by my collaborators, Dr. Huan Tran from Georgia Institute of Technology (Georgia Tech) and Dr. Tuoc Vu from Hanoi University of Science and Technology (HUST). The main goal of our first-principles simulation is to estimate the trend of some structural and electronic structure properties of the series of $(BA)_2(MA)_{n-1}Pb_nI_{3n+1}$. Three members of this 2D organic-inorganic hybrid perovskites series, which correspond to n = 1, 2, and ∞ (the last

one is asymptotically 3D $MAPbI_3$) were considered. The most notable structural distortion, which has been discussed very intensively during the last several years, is the breaking of the inversion symmetry of 3D $MAPbI_3$, the n = ∞ member of this series. The atomic model of 3D $MAPbI_3$ was chosen to be the centrosymmetric tetragonal *I4/mcm* structure (a = 8.80 Å and c = 12.69 Å).[16, 147] Then, the 2D models corresponding to n=1, and 2 were crafted from the *I4/mcm* structure of $MAPbI_3$, introducing the required BA cations. The 2D models consist of alternating layers of BA cations and $(MA)_{n-1}Pb_nI_{3n+1}$. All of these models are visualized in **Figure 3.13**. Our first-principles calculations were performed at the level of density functional theory (DFT) using the projector augmented wave method[148] as implemented in Vienna *Ab initio* Simulation Package (VASP).[149-152] A basis set of plane waves with kinetic energy up to 500 eV was used to represent the Kohn-Sham orbitals. While the generalized gradient approximation Perdew-Burke-Ernzerhof (PBE) exchange-correlation (XC) functional[153] was used throughout this work, the vdW interactions were estimated using the method of Grimme.[154] The Brillouin zone of n = ∞ model was sampled by a Monkhorst-Pack k-point mesh of 5 × 5 × 3 while for those of n = 1, and 2 models, we used the mesh of 5 × 5 × 1. Convergence in optimizing the structures was assumed when the atomistic forces become less than 0.01 eV/A.

The organic-inorganic nature of 3D $MAPbI_3$ has unique and profound implications on its structure. At the atomic level, the PbI_3 network and the MA cations are held together by very weak van der Waals (vdW) and Coulombic interactions while within each of these constituents, the atoms are bonded strongly by ionic and covalent interactions. Because the MA cations are relatively small compared to the cages formed by the PbI_3 network, they can easily vibrate rotationally at rather low frequencies (f ≤ 1THz).[155] On one hand, such

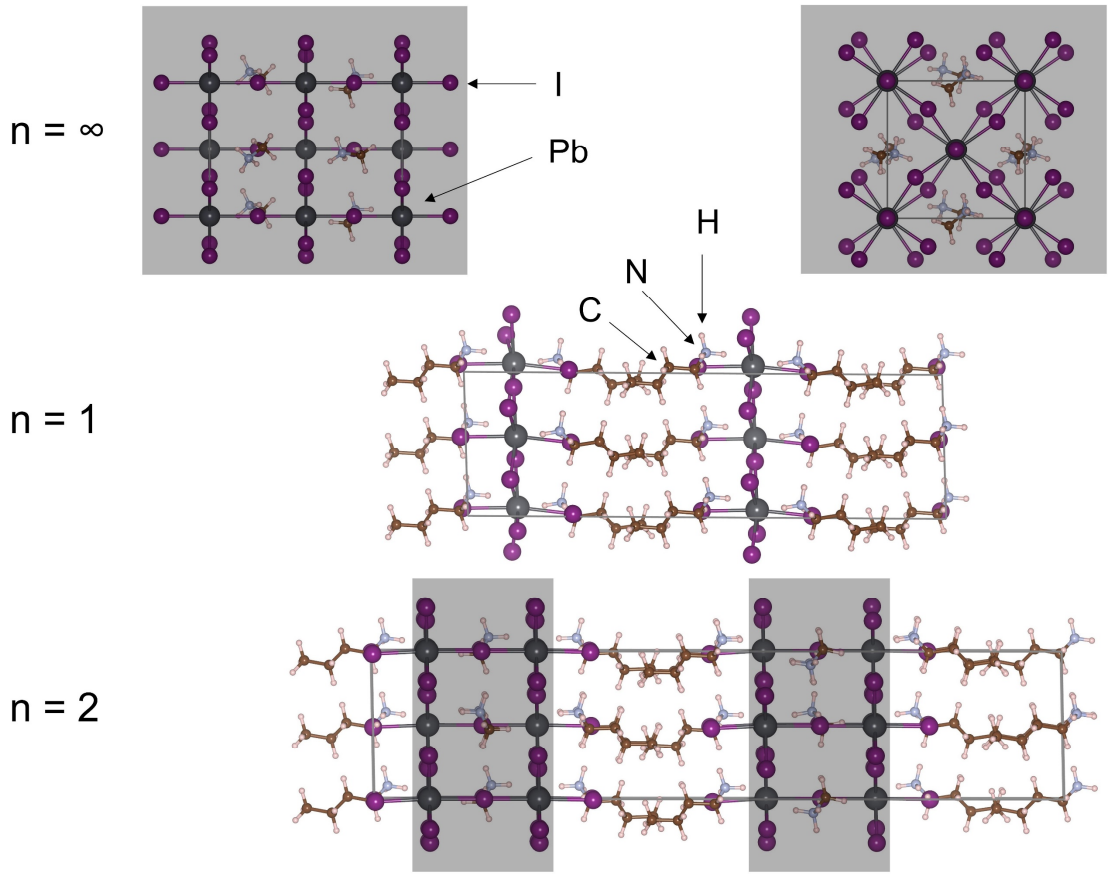

Figure 3.13. Atomic models for n = ∞, 1, and 2 of the series of $(BA)_2(MA)_{n-1}Pb_nI_{3n+1}$. *During the optimization, Pb and I atoms in shared regions were relaxed selectively in order to account for the rotational vibration MA.*

motion makes the asymmetric MA cations appear (effectively) symmetric while preserving the inversion symmetry of the PbI_3 perovskite structure.[16] On the other hand, it makes experimental and computational investigations more challenging. Although the Wyckoff sites of MA can be experimentally resolved, each of them often has a certain probability to be occupied by a given species.[147] From the computation standpoint, selecting a particular "state" of such a "quantum superposition" is required for any static calculations, e.g., those for obtaining the electronic band structure. However, this practice will certainly destroy

the inversion symmetry of the "entropy stabilized" configuration, hereby artificially magnifying some related effects, e.g., Rashba spin-orbit coupling.[16, 96] In a practical solution proposed in 2018[16] for addressing this challenge, the atomic positions of the PbI_3 framework are fixed at the experimental values while the MA cations are relaxed without constraints. Using this this procedure, the experimentally measured Rashba effects[96] in 3D $MAPbI_3$ can be correctly reproduced using DFT.[16] The key point of this solution is that 3D $MAPbI_3$ is essentially electronically decoupled, i.e., its electronic structure is dominated by the connected PbI_3 framework, while the MA cations are isolated and play minor roles.

Noting that the approximations adopted in the exchange-correlation functionals used by DFT generally lead to a systematic numerical error of ≈ +1 - 2 % in the bond length and lattice parameters, we proposed an improved version of the procedure suggested by Frohna *et al.* [16] In the first step of our procedure, the relative coordinates of all the atoms and the shape of the simulation box are fixed while its volume is relaxed. In the second step, the box shape and volume as well as the parts of the PbI_3 framework that are far from the interface and enclose MA cations were fixed while the atomic degrees of freedom of BA cations and the I atoms at the organic/inorganic interfaces were freely optimized (see **Figure 3.13**). These two steps were repeated until the equilibration is obtained. The first step aims at releasing the aforementioned systematic numerical error while preserving the designed symmetries of the PbI_3 framework. The second step is similar to that proposed in the reference[16] simulating the reconstruction of the organic-inorganic interface where the inversion symmetry is broken, while maintaining the entropy-stabilized symmetry of the PbI_3 framework.[16]

With the aforementioned setup, all of the goals of our procedure were obtained. In particular, the optimized *a* and *b* (the in-plane directions) of models corresponding to n = 1, 2, and ∞ are 8.89 Å, 8.88 Å, and 8.82 Å, respectively. For the 3D $MAPbI_3$, the lattice parameters are about 1% higher than the experimental values (8.80 Å). Moreover, the

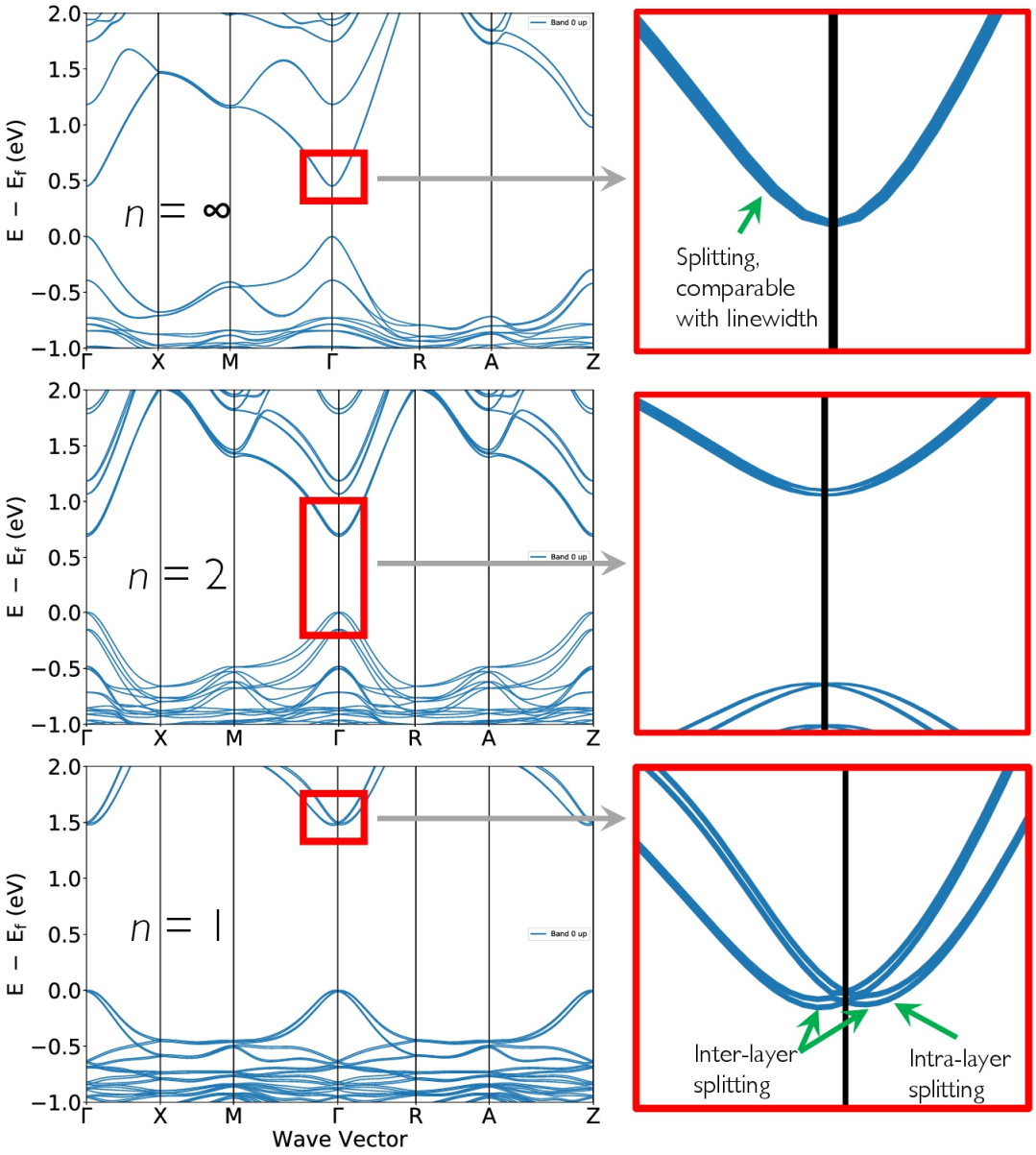

Figure 3.14. Electronics structure of (top) 3D $MAPbI_3$, i. e., n = ∞, (middle) 2D $(BA)_2(MA)Pb_2I_7$, and (bottom) 2D $(BA)_2PbI_4$.

tetragonal symmetry *I4/mcm* of the far-from-surface part of the PbI_3 framework was preserved.

There are two distinct classes of structural reconstructions that break the inversion symmetry. The major class involves the relative position of two consecutive $(MA)_{n-1}Pb_nI_{3n+1}$ layers enclosing a BA layer while structural distortions within each $(MA)_{n-1}Pb_nI_{3n+1}$ is much smaller. These two classes of distortions that induce two types of Rashba spin-orbit splitting, as shown in **Figure 3.14**. For 3D $MAPbI_3$, the splitting is small, being consistent with experimental[96] and computational[16] reports. For the n = 1 2D $(BA)_2(MA)_{n-1}Pb_nI_{3n+1}$ model, the band gap is significantly widened. These effects are commonly reported in the literature. Moreover, the inter-layer distortion leads to the major Rashba spin-orbit splitting while intra-layer distortions further split the electronic bands at a smaller magnitude. The degrees of energy splitting for spin-up and spin-down charges in the conduction and valance bands observed in **Figure 3.14** and its insets are attributed to the different Rashba SOC strengths in the materials in which is the largest SOC strength is for n = 1, and the smallest one is for 3D MAPbI3. The calculated result qualitatively agrees well with our experimental results.

3.5 FARADAY ROTATION OF 2D RUDDLESDEN-POPPER HOIPS

In this part, I will present the experimental results of another complementary magneto-optical effect in 2D RD HOIPs, the Faraday effect. We observed large magnetic circular dichroism effect in the materials, then it is naturally to expect a large Faraday effect would happen because they are both stem from discrepancy of the left and right circular light when interacting with the materials under an applied magnetic field. The Faraday effect, or Faraday rotation, is a magneto-optical phenomenon in which the polarization of light

rotates when it travels through materials under a magnetic field applied along the propagation direction.[156-158] **Figure 3.15** illustrates the Faraday effect: the polarization of light (red arrow) is rotated when travelling through the material under a magnetic field applied along the propagation direction. The Faraday effect has applications in measuring instruments, the most common being theoretical isolator. In research, Faraday rotation and time-resolved resonant Faraday rotation spectroscopy is a powerful tool to study spin dynamics and magnetic properties of materials.[157, 159]

The Faraday effect was discovered by Michael Faraday in 1845 and was the first experimental evidence that light and electromagnetism are related. In some materials, the Faraday effect happens even with no applied magnetic field, which is called optical rotation. The Faraday effect is caused by the difference of speed of the left and right circular light under the applied magnetic field, which is known as circular birefringence. The rotation angle, θ, can be expressed by the difference between refractive index of the left and right circular light.

$$\theta = \frac{1}{2}(n_r kd - n_l kd) \quad (3.6)$$

Where n_r and n_l are the refractive index of the right and left circular light, d is the sample length and k is the wave number of the light.

In general, linearly polarized light along the x-axis can be decomposed into right circular light (RCP) and left circular light (LCP) using Jones matrix formalism.[160]

$$E = e^{i(kz-\omega t)}\begin{pmatrix}1\\0\end{pmatrix} = \frac{e^{i(kz-\omega t)}}{2}\begin{pmatrix}1\\i\end{pmatrix} + \frac{e^{i(kz-\omega t)}}{2}\begin{pmatrix}1\\-i\end{pmatrix}$$

Let n_r and n_l be the refractive index of the RCP and LCP. d is the sample's length. When light transmits through the sample, the electric field vector becomes:

$$E' = \frac{e^{i(n_r kd-\omega t)}}{2}\begin{pmatrix}1\\ i\end{pmatrix} + \frac{e^{i(n_l kd-\omega t)}}{2}\begin{pmatrix}1\\ -i\end{pmatrix}$$

Let $\varphi = \frac{1}{2}(n_r kd + n_l kd)$ and $\theta = \frac{1}{2}(n_r kd - n_l kd)$, we shall get:

$$E' = e^{i(\varphi-\omega t)}(\frac{e^{i\theta}}{2}\begin{pmatrix}1\\ i\end{pmatrix} + \frac{e^{-i\theta}}{2}\begin{pmatrix}1\\ -i\end{pmatrix}) = e^{i(\varphi-\omega t)}\begin{pmatrix}cos\theta\\ -sin\theta\end{pmatrix} \quad (3.7)$$

Equation (3.7) shows that the initially linearly polarized light has rotated an angle θ because of circular birefringence. The rotation angle θ is proportional to the applied magnetic field B,

$$\theta = BdV \qquad (3.8)$$

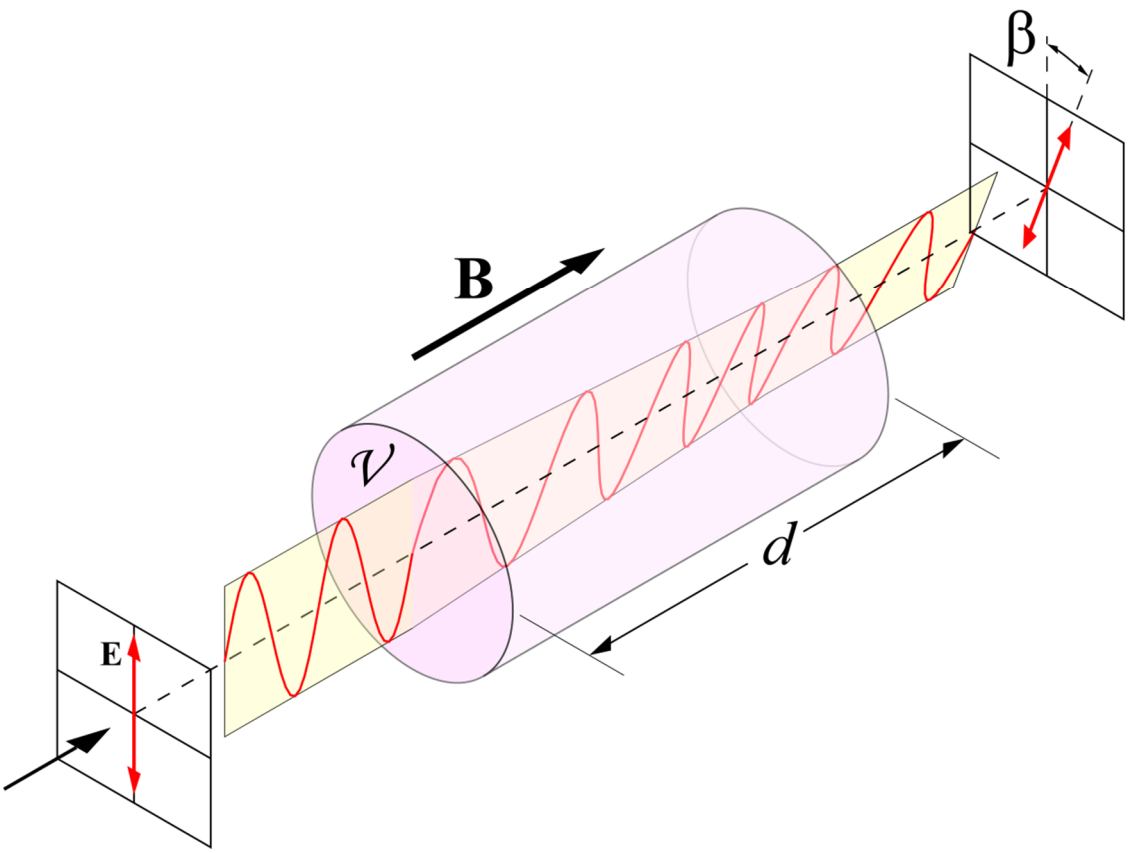

Figure 3.15. Illustration of Faraday effect. The polarization of light (red arrow) is rotated when travelling through the material under a magnetic field applied along the propagation direction.

where B is the applied magnetic field, d is the samples' length and V is Verdet constant. It can be derived classically and quantum mechanically the formula of Verdet constant:[156]

$$V = \frac{e}{2m_0 c}\omega\frac{dn}{d\omega} \qquad (3.9)$$

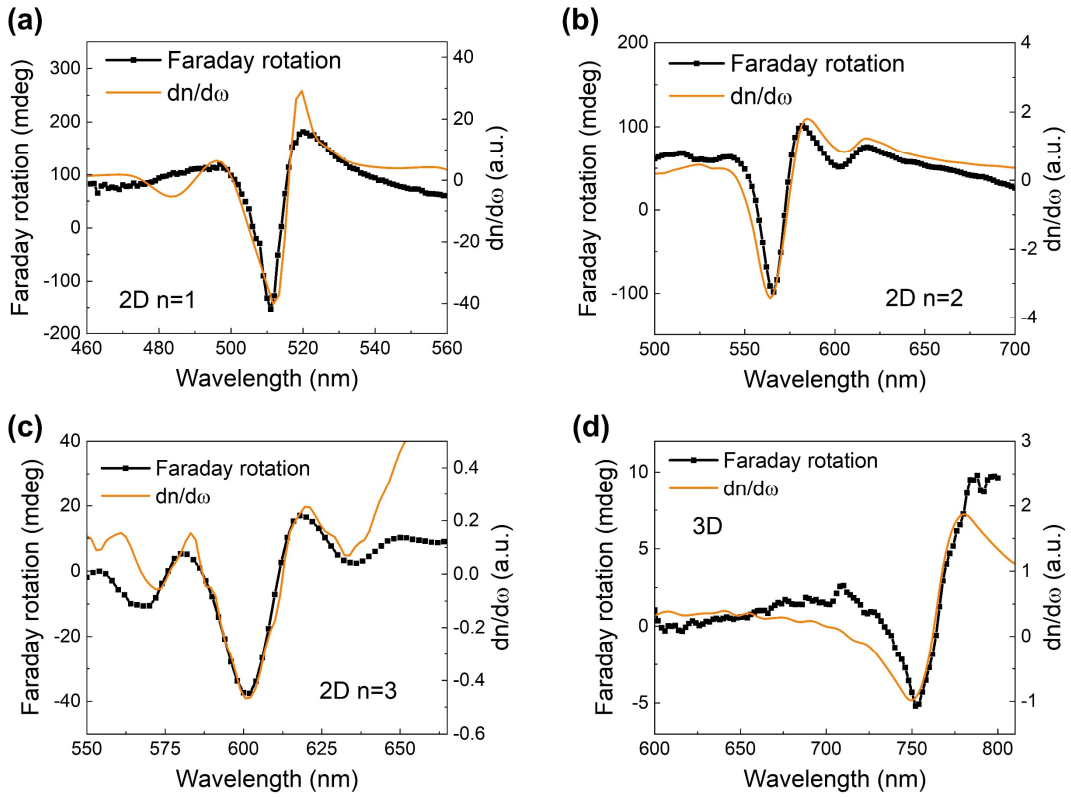

Figure 3.16. Faraday rotation of the 2D RD HOIPs and 3D $MAPbI_3$ thin films (black dot lines) under the applied magnetic field 3.5 T. The orange lines are the first derivatives of the real part of the refractive index.

Where e and m_0 are electron's charge and mass, respectively. c is the speed of light, ω is light's frequency and n is the refractive index of the material.

A high Verdet constant is the key criteria for material used in optical rotator. The industry standard material in the visible range is terbium gallium garnet (TGG), which has extremely high Verdet constant (~ 134 rad/(T.m) at the wavelength of 632 nm.[161-162]

Recently, Sabatini et al. have reported that single crystal 3D perovskite $MAPbBr_3$ exhibits a similar or greater magnitude, up to 2.5 times of Verdet constant in comparison to TGG.[163] Therefore, it is expected that the 2D RD HOIPs would possess an even higher Verdet constant. Next, I will present my results on Faraday rotation of perovskite thin films.

Figure 3.16 presents the Faraday rotation of the 2D RP HOIPs and 3D $MAPbI_3$ at room temperature under an applied magnetic field of 3.5 T. The black dot lines are the Faraday rotation spectra while the orange lines are the first derivative of the real part of the refractive index, which were measured using a spectroscopic ellipsometer. (see details in **Figure C2, Appendix C**). Our results show an excellent fit between Faraday rotation and the derivative of the real part refractive index, n, which are in agreement with **equation (3.9)**. The FR features appear at the excitons' resonance, as in the MCD signals from part 3.3. Here, we observe the same trend in that the FR magnitude monotonically decreases as the number of perovskite layers n increases. For the 2D RP thin films, the peak-to-peak FRs are ~300, 200 and 60 mdeg, when n = 1, n = 2 and n = 3, respectively. Finally, when $n = \infty$, which corresponds to the 3D counter $MAPbI_3$, the peak-to-peak FR is dropped to ~15 mdeg. We note that the FR magnitude depends on the thickness of the films as described in equation (3.8). Therefore, to fairly compare the strength of Faraday effect, we need to count on the Verdet constants. The thickness of all the 3D and 2D RP perovskites thin films are measured by a profilometer. The results are shown in **Figure C1, Appendix C**. **Figure 3.17** shows the Verdet constants spectra of all the perovskite thin films. All the perovskite materials show extremely high Verdet constants. From the results in **Figure 3.17**, The Verdet constant of the 3D perovskite has a magnitude of 1121 rad/T.m at 788 nm, which is 8 times higher than that of TGG at 632nm. The highest value of the Verdet

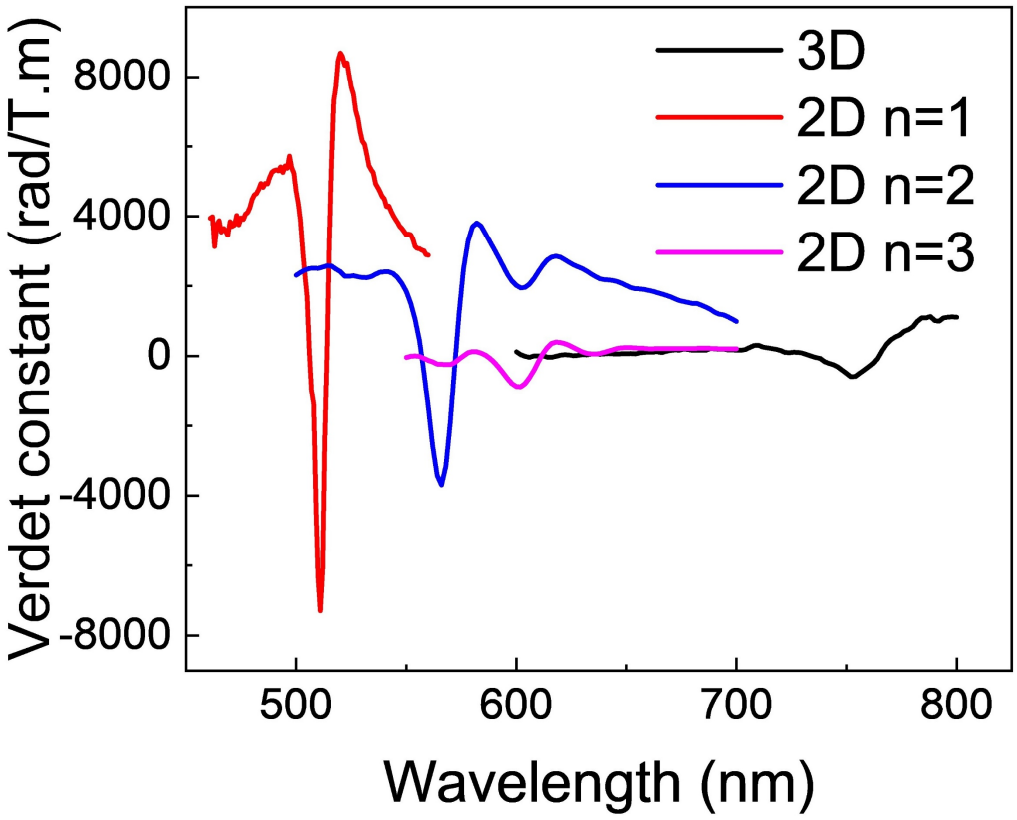

Figure 3.17. Verdet constants of the 2D RP and 3D perovskites thin films

constant is 8689 rad/T.m at 520 nm from the 2D RP n = 1 thin film. However, we note that, the since the peak and dip of FR spectra appear around the excitonic transition, the transmittance is quite low at the wavelengths where the Verdet constant reaches its extrema. For examples, at 520nm for 2D n = 1 thin film, the transmittance is only 12.5%, and at 582 nm (2D n = 2), the transmittance is 29.5%. Away from the resonance, the Verdet constants of 2D perovskite thin films are still extremely large. For instance, comparing to TGG at 632 nm, the Verdet constant of 2D n = 2 thin film is 18 times higher, while the transmittance is 88%. This indicates a very high potential for application of the solution-

processed optical rotator. More details on the Verdet constant of the perovskite thin films can be found at **Table 4**, **Appendix C**.

3.6 CONCLUSIONS

We have systematically studied the CD and CPL effects in non-chiral 2D RP perovskites and found the unusually large CD and CPL effects, especially with n = 1. Our results indicate that "chirality transfer" is not the only mechanism causing the CD and CPL in HOIPs in general. We attributed the large CD and CPL to the giant Rashba-Dresselhaus splitting in the materials. DFT calculations reveal that the main reason for strong Rashba-Dresselhaus splitting in RP HOIPs, especially for n = 1 is the inter-layer distortions in the inorganic layers while the intra-layer distortions further split the electronic bands at a smaller magnitude. The Rashba-Dresselhaus field of ~500 mT in the superlattice with n = 1 was estimated by the MCD spectroscopy. The strong Faraday effect is also observed in the 2D and 3D HOIPs thin films. The Verdet constant in 2D perovskites is a dozen times higher than that of industry's standard TGG. Our findings suggest applications of 2D RP perovskites in novel spintronics and optics devices. More experiments will be conducted to explore the numerous physics in these interesting class of materials.

CHAPTER 4

STUDY OF ENERGY UPCONVERSION AND ENERGY TRANSFER PROCESSES IN RUBRENE/PEROVSKITE SYSTEM BY MAGNETO-PHOTOLUMINESCENCE

The photovoltaics of organic–inorganic lead halide perovskite materials have shown rapid improvements in solar cell performance. Recently, it has been interested in using perovskites as an excellent light absorber for triplet sensitizer to achieve upconversion luminescence under low energy excitation photons. The upconversion occurs when two triplet excitons transferred from perovskite to singlet fission molecules annihilates to create a higher-energy singlet exciton. In a $MA_{0.15}FA_{0.85}PbI_3$/rubrene bilayer system (MA = methylammonium, FA = formamidinium) an upconversion efficiency in excess of 3% has been recently reported. However, the underlying mechanisms associated with the triplets transferred from $MA_{0.15}FA_{0.85}PbI_3$ to rubrene and the singlets transferred back to the $MA_{0.15}FA_{0.85}PbI_3$ have not been thoroughly studied. In this chapter, I will use the magnetophotoluminescene (MPL) to track and resolve the exciton transfers in the $MAPbI_3$/rubrene system, and to understand the triplet-triplet annihilation (upconversion) process.

4.1 OVERVIEW OF ENERGY TRANSFER PROCESSES BETWEEN RUBRENE AND PEROVSKITES

Organic–inorganic hybrid perovskites with the advantages of low-cost, high absorption coefficients, long carrier diffusion lengths and high charge carrier mobilities, have been extensively studied in the field of photovoltaics in the past decade.[164] The record

power conversion efficiency of a perovskite based single-junction solar cell has reached 25.2%,[165] approaching its theoretical Shockley–Queisser limit (~30.5%).[166-167] In general, two promising strategies have been proposed to circumvent the Shockley-Queisser limit in single-junction solar cells. The first strategy is to reduce the thermalization losses caused by the absorption of excessive photo energy and enable better sensitivity to light by sensitizing the solar cell using singlet exciton fission, in which two triplet excitons are generated from a photoexcited state of higher energy singlet exciton.[168-169] The second strategy is to collect below-gap photons by the energy upconversion process. In upconversion, light of a given photon energy is converted into higher energy photons. While this can be achieved under high light intensities using non-linear optical techniques and pulsed lasers (two-photon absorption, and second harmonic generation, etc.[170]), there has been recent interest in low-power, incoherent upconversion due to triplet–triplet annihilation (TTA) as described in **Figure 4.1a**.[171] In this scheme, the triplet sensitizer absorbs a photon to yield a photo-excited singlet exciton. The exciton then undergoes intersystem crossing (ISC) to convert the singlet exciton into a triplet exciton with a lower energy by an exchange energy. The triplet exciton may transfer to the adjacent emitter molecule by the process such as Dexter energy transfer[169] or sequential electron-hole transfer.[172-173] Eventually, the upconverted light is produced through the reaction of triplet molecules in the emitter via the TTA process. This process can thus be affected under a weak and incoherent light such as from the sun.[174] If this process can be made significantly efficient, it could be applied to single threshold solar cells to harvest that unused part of the solar spectrum of energy lower than the band-gap, boosting energy conversion efficiencies. Despite the importance of low-power upconversion, there is still no consensus

as to the theoretical upper limit for the TTA process. The upconversion efficiency of up to 40% and 20% has been theoretically predicted and experimentally achieved.[175]

Lead halide perovskite, $MAPI_3$, thin films have shown great promise as excellent triplet sanitizer because of the following reasons. First, it has high absorbance as high as 10^5 cm^{-1}[1176] in a broad absorption spectrum down to the near IR region, the ideal condition for the light absorber thin film (about 280 nm of $MAPbI_3$ is sufficient to absorb ~80% of the incident sun light below the bandgap[177]). Next, due to the strong intrinsic spin-orbit coupling (SOC) and Rashba-Dressellhaus SOC, $MAPbI_3$ has a slightly indirect band gap with negligible recombination. With a large dielectric constant,[98-99] long carrier diffusion lengths on the order of 100 μm[178], and high electron/hole mobility of ~ 100 $cm^2(Vs)^{-1}$ [179], electrons and holes in $MAPbI_3$ are delocalized and form Wannier-type exciton with negligible exchange energies, resulting in the negligible energy loss due to the singlet-to-triplet interconversion process.[180] Finally, strong SOC in $MAPbI_3$ also allows fast intersystem crossing rate between singlet and triple excitons which is very promising for achieving up to100% triplet exciton yield when combining with suitable emitter molecules. Recently, Nienhaus. et al.[172] have achieved an upconversion efficiency that exceeds 3% in a $MA_{0.15}FA_{0.85}PbI_3$/rubrene bilayer system. Although the concept was demonstrated, the ultra-thin $MAPbI_3$ of a little above 10 nm thickness causes ultra-small absorbance from the absorber, thus limiting its practical applications. Rubrene is an ideal TTA or singlet fission/fusion material whose triplet energy of ~1.14 eV[181] is lower than triplet energy of ~1.50 eV in the $MAPbI_3$ that facilitates strong triplet Dexter energy transfer from $MAPbI_3$ to rubrene. However, according to Nienhaus *et al.*[172] the dominant triplet energy transfer from $MA_{0.15}FA_{0.85}PbI_3$ to rubrene in the bilayer system is not governed by the Dexter

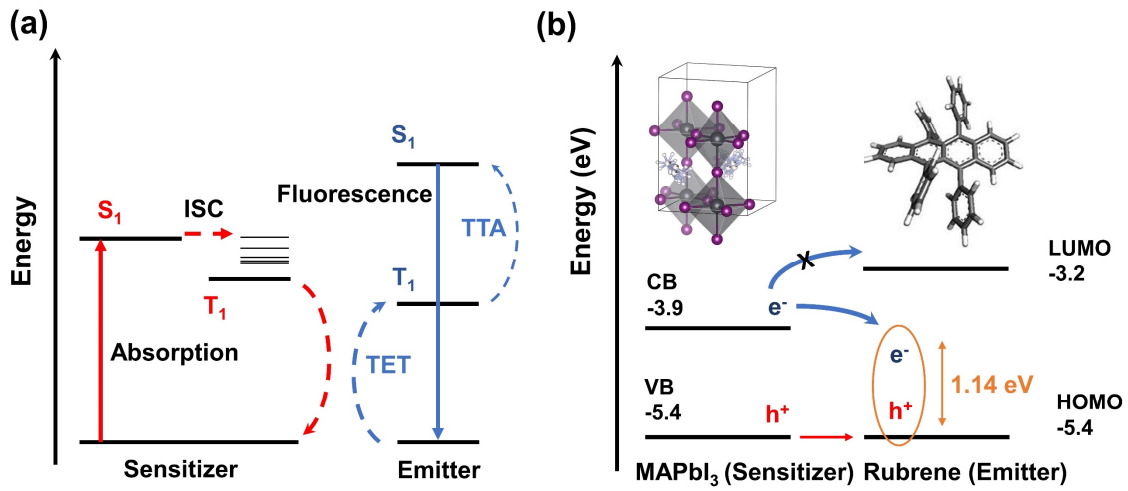

Figure 4.1. (a) Jablonski diagram describing photon upconversion through triplet-triplet annihilation. (b) Band diagram of $MAPbI_3$ and rubrene, showing the hole transport from the perovskite valance band (VB) to the rubrene HOMO. The electron cannot directly transfer from the perovskite conduction band (CB) to the rubrene LUMO due to an energy barrier of ~1 eV. The inset shows the chemical structure of rubrene and $MAPbI_3$.

energy transfer (**Figure 4.1a**) but by the sequential electron and hole transfer resulting in a bound triplet on the rubrene molecule as described in **Figure 4.1b**. The energetic band alignment indicates that when the electron-hole pair is generated in $MAPbI_3$ by photoexcitation, the hole transfer from the perovskite valence band (VB) to the highest occupied molecular orbital (HOMO) of the rubrene can be very efficient due to the driving energy of ~0.4 eV.[182] An unbound electron on the other hand cannot transfer directly into the lowest unoccupied molecular orbital (LUMO) of rubrene due to the ~1 eV energy gap between the perovskite conduction band (CB) and the rubrene LUMO, despite significant band bending reported by Ji *et al*.[182] However, with a hole residing on the rubrene molecule, it may be possible to transfer the electron directly into the bound triplet state (T_1) through a mediating charge-transfer state (CT) at the interface.[183-184] If this is a case, the time scale

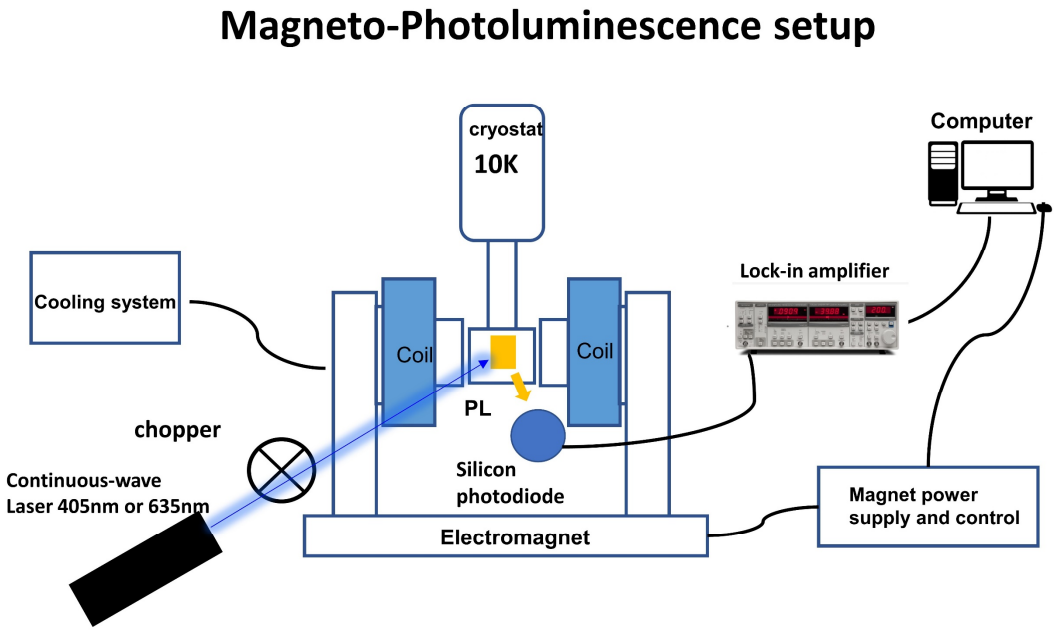

Figure 4.2. MPL measurement setup.

for T_1 in rubrene to be formed would be long. Nienhaus. *et al.*[172] suggest that sequential charge transfer is likely to be the dominant triplet sensitization mechanism. However, if this scenario happens, the triplet formation in the triplet sanitizer $MAPbI_3$ is not needed for the upconversion process. In this chapter, I will employ the magnetic field effect on photoluminescence (MPL) to systematically study the energy/charge transfer and upconverstion processes in the $MAPbI_3$/rubrene system which has slightly different energy levels than the $MA_{0.15}FA_{0.85}PbI_3$/rubrene system (**Figure 4.1b**). Several $MAPbI_3$/rubrene thin films including $MAPbI_3$/rubrene blends, $MAPbI_3$/rubrene bilayers, $MAPbI_3$/insulator/rubrene trilayers are designed to distinguish the charge and triplet energy transfer processes. Since the MPL in rubrene and $MAPbI_3$ films are very different, they will be used to analyze and resolve upconversion and energy transfer processes.

4.2 SAMPLE PREPARATION, CHARACTERIZATION AND MEASUREMENT

The thin films, including 3D perovskite $MAPbI_3$ and the blend films (3D perovskite and rubrene) were prepared by solution casting method. The host-casting method was used as described in the previous chapter. The perovskite crystal was dissolved in DMF to get a solution with concentration of 0.25 M. Rubrene powder was dissolved in toluene to obtain a solution of 10 mg/mL. The two solutions were well mixed thank to the good solubility of the two solvents. The percentage of rubrene volume in the mixture were 2%, 25% and 50%. For the bilayer perovskite/rubrene and trilayer of perovskite/ Poly (methyl methacrylate) (PMMA)/rubrene samples, the perovskite layer (~50nm) was spin casted on glass substrate using the same procedure in Chapter 2 and 3. 20nm of PMMA and 100 nm of rubrene layers were thermal evaporated at a rate ~0.5 A/s under the vacuum of 1 x 10^{-6} mbar. The samples then were characterized with X-ray diffraction spectroscopy (XRD).

Figure 4.2 depicts a schematic of the MPL measurement setup. The sample (thin film) is mounted on the cold finger of a closed-cycle helium cryostat purchased from Advanced Research System that keep the temperature of the film at 10 K. The cryostat is placed between two poles of an electromagnet that can produce a magnetic field up to 300 mT with a one-Gauss resolution. The thin film was excited by the continuous-wave laser 405 nm (or 635 nm) and the PL intensity was simultaneously measured by a Si photo-detector, while sweeping B. The MPL is defined as follow:

$$MPL(\%) = \frac{PL(B) - PL(0)}{PL(0)} 100\%$$

Where *PL(B)* and *PL(0)* are the current flowing through the device with and without an applied magnetic field B.

Figure 4.3a shows the XRD spectra of the $MAPbI_3$/rubrene bilayer and thin films with 0%, 2%, 25%, 50% rubrene blended in the $MAPbI_3$ 3D perovskite. The strong diffraction features of the $MAPbI_3$ crystal at (110) and (220) crystallographic planes remain in all films.[84] However, such peaks become weaker with the larger rubrene concentration in the film and are significantly suppressed with the 50% rubrene concentration. We conclude that the crystallinity of the $MAPbI_3$ perovskite in the film starts collapsing at this

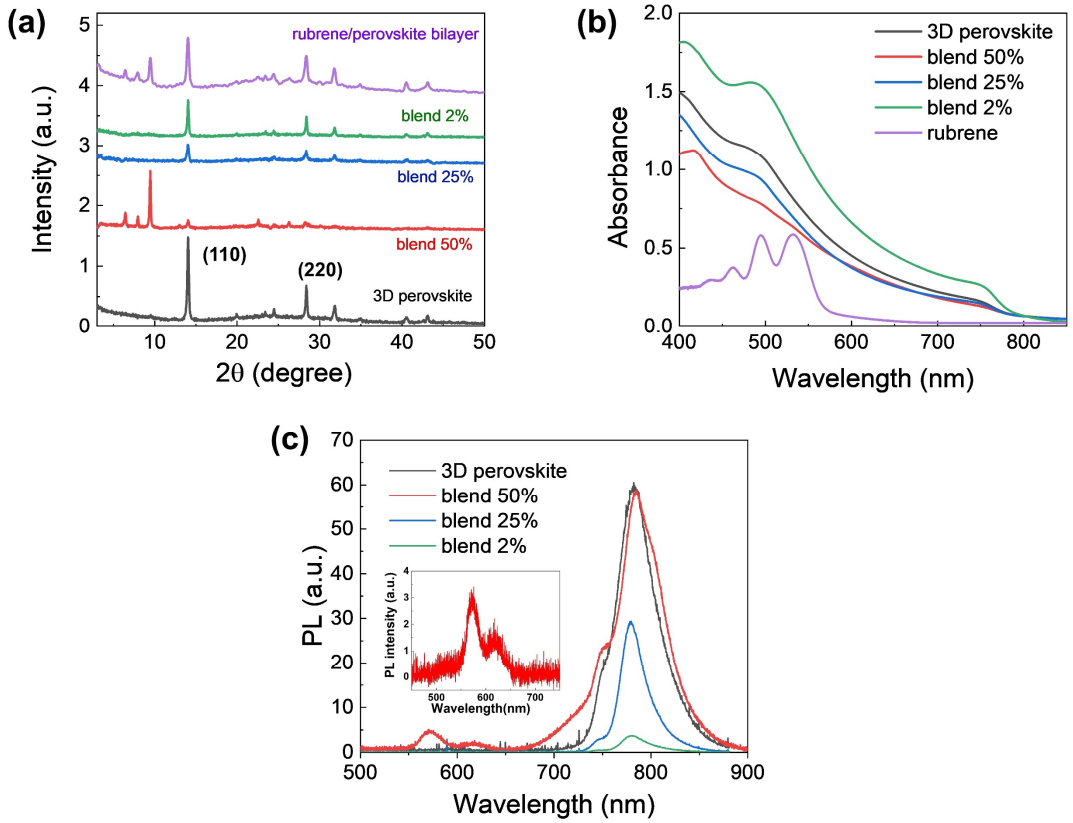

Figure 4.3. (a) Absorption spectra of pure $MAPbI_3$, pure rubrene thin films and thin films of their blends. (b) XRD spectra of the thin films. (c) PL spectra of the films excited by a 405 nm laser. The inset shows the zoom-in of rubrene emission spectrum of the 50% rubrene film.

concentration. The rubrene nanocrystalline grain size of ~45 nm is estimated using the Scherrer formula.[185] Using the same method, the perovskite nanocrystalline grain sizes are both ~52 nm for the pure perovskite and the 2% rubrene blend thin film. Interestingly, the perovskite grain size in 2% rubrene blend (52.4 nm) is slightly larger than that of the pure perovskite thin film (52.3 nm). It might be the reason for the improvement in absorption of the 2% rubrene bend thin film shown in **Figure 4.3b**. This might suggest that rubrene can be used as an additive for a better perovskite solar cell. The grain sizes become smaller when the concentration of rubrene in the blend increases: they are ~ 39 nm and 35 nm corresponding to the 25% and 50% blends, respectively. We note that at 50% rubrene concentration, additional strong diffraction features occur at below 10º and are assigned to the diffraction from rubrene nanocrystals. The features can be clearly seen in the XRD spectrum of the $MAPbI_3$/rubrene bilayer but not in the pure $MAPbI_3$ film (see **Figure 4.3a**).[186] Such features do not exist in the thin films with 2% and 25% rubrene concentrations indicating that the rubrene molecules are well-mixed in the perovskite at these concentrations and the rubrene morphology is amorphous. **Figure 4.3b** shows the absorption spectra of the thin films with 0%, 2%, 25%, 50%, 100% rubrene concentrations. The absorption features of $MAPbI_3$ at ~760 nm and ~490 nm clearly remain in the blends with the exception of 50% rubrene film where those features are weak. Those absorption features are theoretically assigned to the band-to-band transitions in $MAPbI_3$.[187] The absorption spectral study confirms the crystallographic result by XRD in **Figure 4.3a** that the quality of $MAPbI_3$ in the 50% rubrene film is highly suppressed. We note that the rubrene absorption features are not noticeable in the spectra of the blend due to the weak absorbance of rubrene relative to that in $MAPbI_3$. **Figure 4.3c** shows the

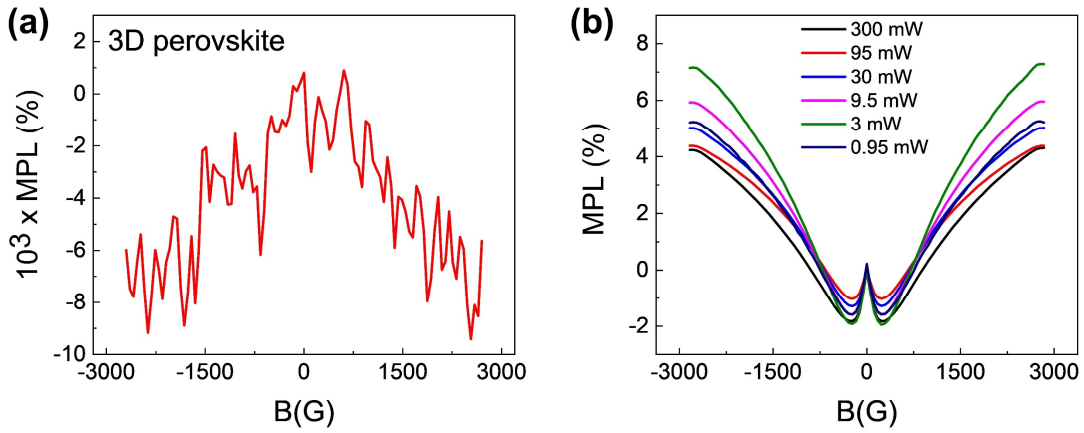

Figure 4.4. MPL responses of (a) a pure $MAPbI_3$ film and (b) a pure rubrene thin film at 10K.

photoluminescence (PL) spectra of all films under a laser excitation at 405 nm with 10 mW laser power. While the PL peak of $MAPbI_3$ at 785 nm is clearly seen in all films, the PL spectrum of rubrene at below 660 nm can be weakly seen only in the 50% rubrene film.[188] There are two scenarios for the absence of the rubrene PL spectrum in such films. First, since the emission spectra of the rubrene are overlapped with absorption spectrum of the $MAPbI_3$ (**Figure 4.3b** and **4.3c**), fast Förster energy transfer rate occurs in the blend to transfer the single excitons from rubrene to single excitons in the $MAPbI_3$, thus quenches the emission from the rubrene.[189] Second, rubrene may emit photons with a slower rate than the energy transfer rate, typically in a ns time scale, that are immediately reabsorbed by $MAPbI_3$. If this scenario occurs, most but not all photons emitted from lower rubrene concentration regime could be reabsorbed by the surrounding $MAPbI_3$. Since the effective radius of faster non-radiative Förster energy transfer rate is just 10 nm while the rubrene grain size is 45 nm in the 50% rubrene film, both Förster energy transfer and reabsorption processes may simultaneously occur in the film. The clear rubrene emission from the film is observed since the $MAPbI_3$ cannot absorbed all emitted photon from rubrene. In contrast,

in the 2% and 25% films, the rubrene is well-mixed with the perovskite probably causing the effective distance between the donor and the acceptor of less than 10 nm. It is likely that a singlet exciton in rubrene generated by either direct photoexcitation or by TTA immediately transfer into $MAPbI_3$ located within the effective radius via the fast non-radiative Förster energy transfer. This causes the absence of rubrene emission in these films even when they are excited by strong laser excitation of ~100 mW at 405 nm, 450nm and 532 nm.

Figure 4.4a shows the magneto-photoluminescence (MPL) of pure $MAPbI_3$ thin film which is negative and has a very weak magnitude of 0.008% at the applied magnetic field B = ±300 mT and a broad response width, and is consistent with that reported by Zhang et al.[190] The strong intrinsic SOC and Rashba-Dressellhaus SOC are believed to cause the broad MPL response and suppress the MPL magnitude.[56, 190] Since the PL of $MAPbI_3$ directly relates to the photo-excited electron-hole pairs, any explanation of the MPL must involve the spin dynamics of electron-hole pairs in the material. The most possible mechanism for the MPL is the so-called Δg mechanism as thoroughly discussed in Chapter 2. Since the g factors of the electron and hole in the spin-pair are largely different, their spin momenta precess around the applied magnetic field with different Larmor frequencies, $f \propto gB$, where g is the g factor of electron or hole. Obviously, large spin mixing rate between singlet, S^0 and triplet spin-pairs, T^0 depends on the g factor difference, Δg, between electron and hole and the magnitude of the applied magnetic field, B. Due to the large SOCs in $MAPbI_3$, Δg has been measured to be very large in the order of unity.[22] **Figure 4.4b** depicts the typical MPL response in a pure rubrene film versus the pump laser power at 405 nm when B is scanned from −300 mT to +300 mT. The positive

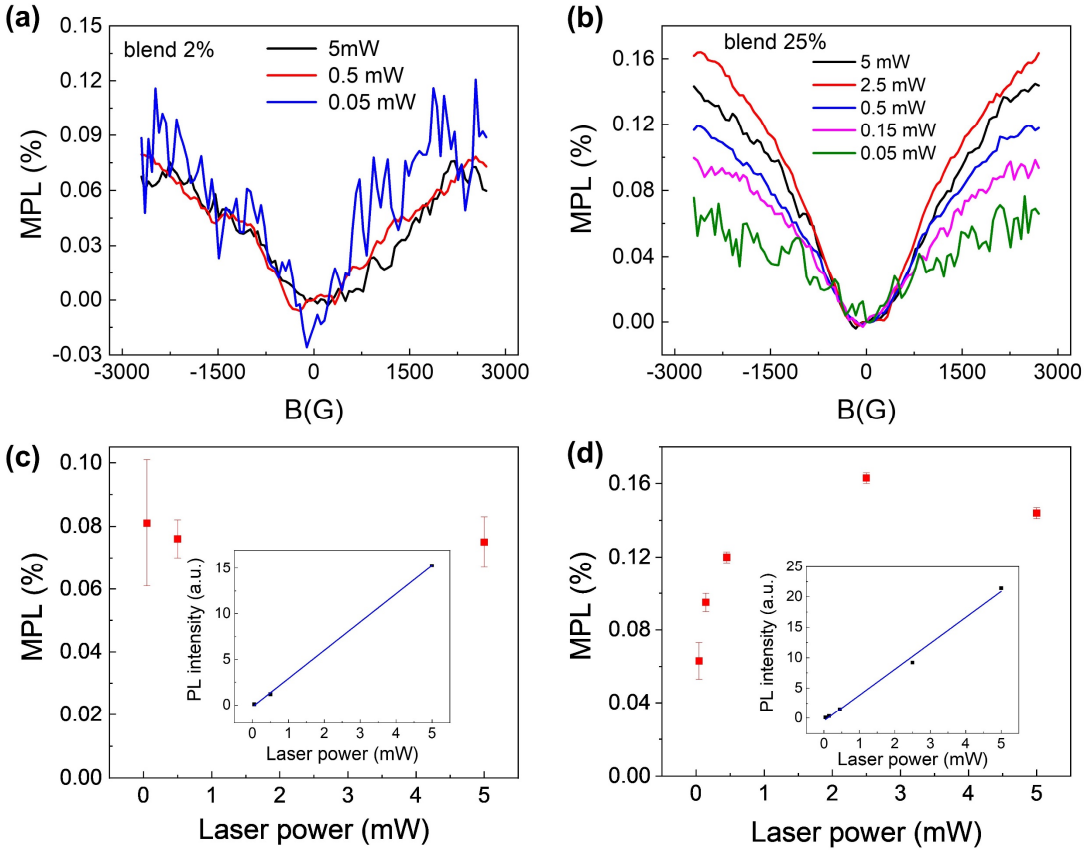

Figure 4.5. MPL of (a) 2% and (b) 25% rubrene films with a 635 nm laser excitation at different laser power. The corresponding magnitudes of MPL in (a) and (b) are processed in (c) and (d) for 2% and 25% rubrene, respectively. The insets show the linear dependent of PL intensity on the pump power. All data were taken at 10K.

MPL magnitude slightly increases from 5.2% at 0.95 mW laser to 7.3% at 3.00 mW laser and slightly reduces when the pump laser intensity increases. Such power dependent MPL is very common in organic semiconductors where multiple spin dependent processes may simultaneously occur causing a complicated MPL response.[56] In general, the MPL response in rubrene comprises of two components: very broad width in the order of several hundred mT and the narrow width with the half width at half maximum (HWHM) of about 5 mT. Such MPL behavior was explained by Merrifield more than 50 years ago by the mechanism

namely TTA mechanism.[191-192] In this mechanism, a triplet-triplet pair with the spin multiplicity in one of the following states can be formed: one singlet states (total spin 0), three triplet states (total spin 3) and five quintet states (total spin 2). Therefore, the probability of forming a singlet state and hence a photon by the annihilation is 1/9. Based on the theory, the TTA process is B-dependent in such a way that the singlet probability slightly reduces at low B but increases at large B causing magnetic response as described in **Figure 4.4b**. Interestingly, since the small field effect has the HWHM of 5 mT which is similar to the typical hyperfine field in organic semiconductors, electron-hole pair mechanism which is based on the spin mixing between singlet and triplet electron-hole pairs by the hyperfine field can be used to explain the effect.[180] Our MPL response is in agreement with the result reported by Tarasov et al.[193] who found that the small field effect is significantly large in the polycrystalline film in compared to the amorphous film.

Figure 4.5a and **4.5b** shows the MPL response of the 2% blend and 25% blend film under different photo-excited laser intensities at 635 nm (~1.95 eV). This laser excitation has a smaller energy than the bandgap of rubrene but larger energy than the band gap of $MAPbI_3$ (see **Figure 4.1b**). As the result, only photo-excited excitons in $MAPbI_3$ are initially generated. We note that in both films, the PL intensity is linearly proportional to the laser intensity as shown in the insets of **Figure 4.5c** and **4.5d**. In this case, we would expect to have similar MPL as seen in the pure $MAPbI_3$ film if there is no optically and electrically coupling between materials (**Figure 4.3a**). Surprisingly, the MPL response in **Figure 4.5a** and **4.5b** are positive, narrower, and larger in magnitude by an order compared to the MPL in pure $MAPbI_3$. The HWHM of the MPL response essentially remains the same in both films. The MPL magnitude in 2% rubrene film stays essentially the same at

0.08% within the measurement noise. The MPL magnitude in 25% rubrene film increases from 0.06% at 0.05 mW laser power to 0.16% at 2.5 mW, and saturate for the larger laser power. The results imply that either the energy/charge transfer from $MAPbI_3$ to rubrene or TTA process is saturated at 2% rubrene film. This is essentially correct since TTA is not sufficient at low rubrene concentrations. Due to the very different MPL responses at the $MAPbI_3$ emission between pure and blended $MAPbI_3$ films, we hypothesize that the photo-excited triplet excitons in $MAPbI_3$ must transfer to rubrene, and undergo energy

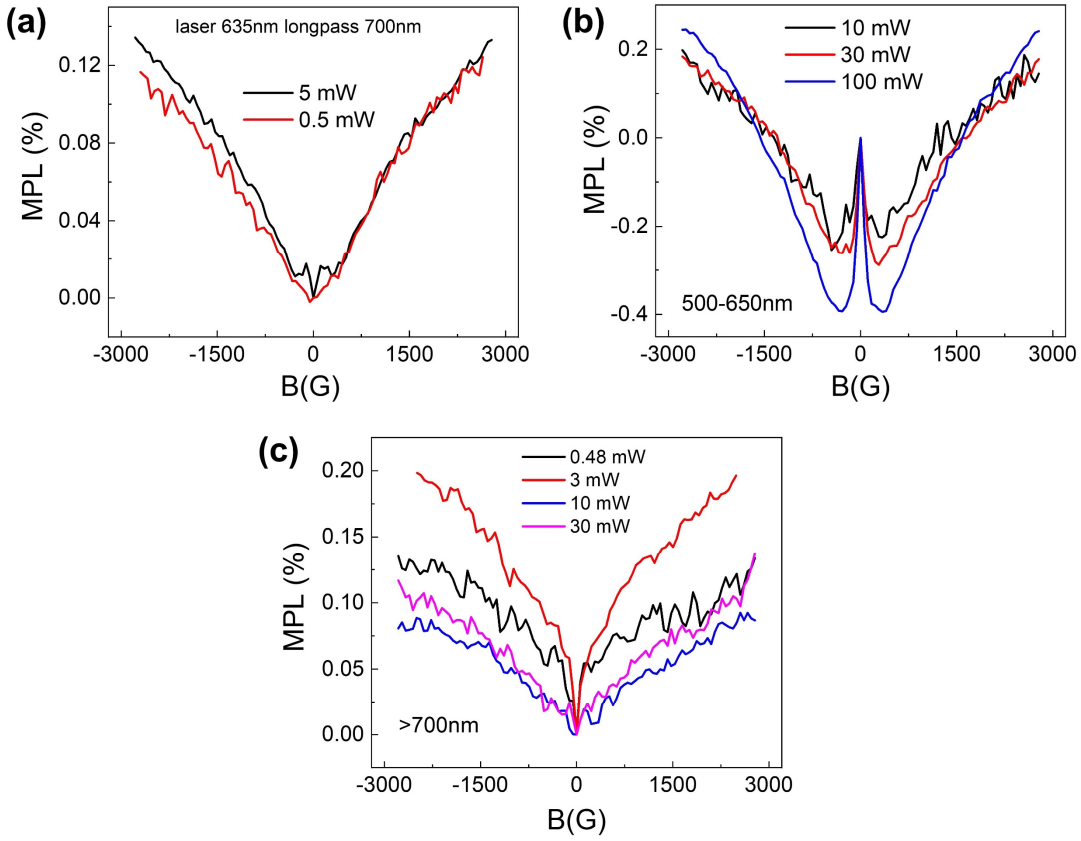

Figure 4.6. (a) MPL response of the 50% rubrene film when the film was pumped by a 635 nm laser at 0.5 and 5 mW powers. MPL of (b) the rubrene emission and (c) the $MAPbI_3$ emission when the film was pumped with a 405 nm laser at different laser powers. All data were taken at 10 K.

upconversion to create singlet excitons in rubrene, which can partially transfer back to the $MAPbI_3$. The TTA rate strongly relies on the rubrene density and morphology. The energy transfer rates between $MAPbI_3$ and rubrene depend on the effective distance between the donors and accepters: typically ~10 nm for Förster energy transfer (a dipole−dipole based energy transfer mechanism), and ~1 nm for Dexter energy transfer (orbital overlap based mechanism), and therefore also depends on the rubrene concentration and morphology as well.[194] Therefore, the MPL magnitude and shape in $MAPbI_3$ has strong dependence on the rubrene density/morphology and magnetic field effect on rubrene. Since the line-shape of MPL in 2% and 25% films is very different from the MPL in rubrene shown in **Figure 4.4b**, both TTA mechanism and electron-hole pair mechanism are not appropriate for explaining the shape of the observed MPL in the blended films. Because both triplet excitons and free holes exist in the rubrene layer, triplets may be annihilated not only by TTA, but also through triplet-charge annihilation (TCA). In the TCA process, a triplet exciton collides with an adjacent single charge and either scatters it.[195] The magnetic field effect has been found to prevent TCA happening[196], remains the triplet density in the rubrene, and thus increases the TTA rate. The response found in **Figure 4.5** and **4.6** perfectly agree with this TCA mechanism.

In order to investigate the MPL effect in a stronger rubrene/$MAPbI_3$ interaction system, the MPL in the 50% rubrene film with the nanocrystalline grain size of ~45 nm is studied. **Figure 4.6a** shows the MPL of the $MAPbI_3$ emission with ~0.12% and ~0.14% magnitudes excited by a 635 nm laser at 0.5 mW and 5 mW, respectively. We note that no rubrene emission was detected within the noise level of our measurement system. In general, the magnitude and the line-shape of the MPL are similar to that observed in 25%

blend film. However, at the small applied field effect with 5 mW power, there is a very small feature that may come from either the effect of hyperfine field in electron-hole pair mechanism or from the TTA mechanism. Since the rubrene emission exists in the film under the 405 nm laser excitation, we decide to study the MPL of rubrene and $MAPbI_3$ separately. By using approximate long pass and short pass filters, the emission of each material can be studied independently under the effect of magnetic field. **Figure 4.6b** shows the MPL effect of the rubrene emission at different laser powers. The MPL line

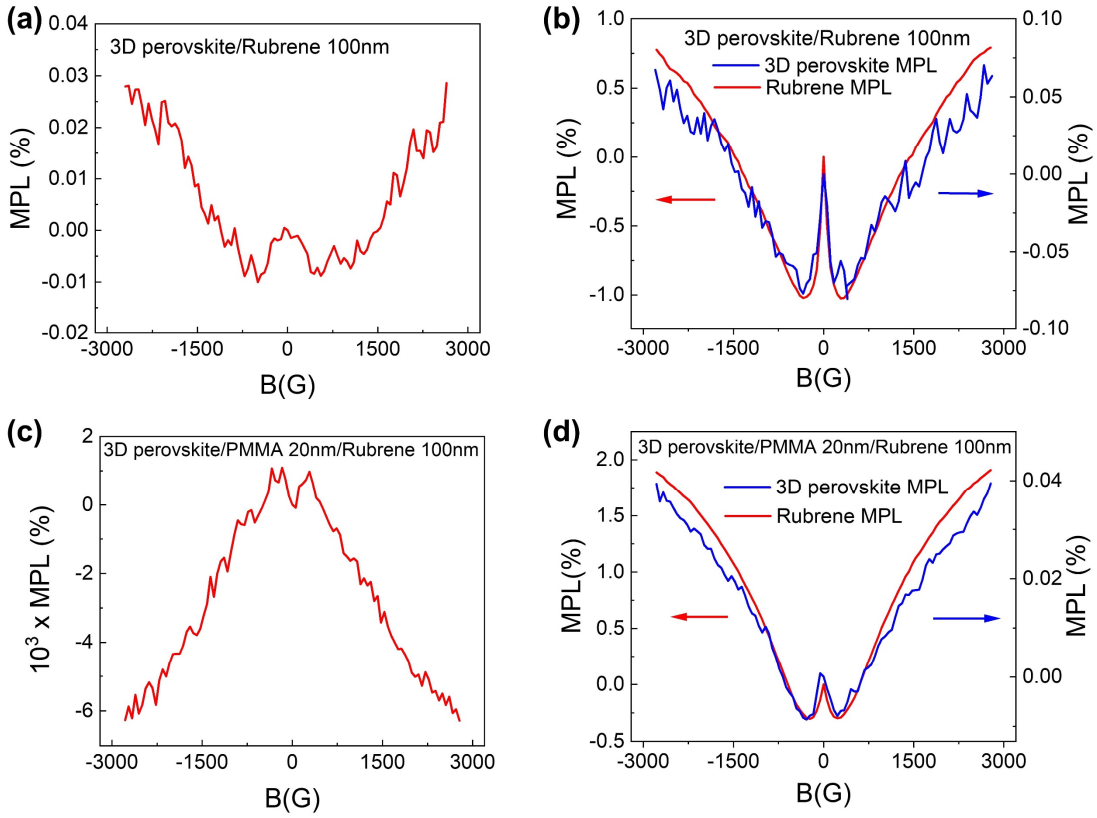

Figure 4.7. MPL in a bilayer films, glass/$MAPbI_3$/rubrene (100nm) when (a) pumped with 635 nm laser and (b) pumped with 405 nm laser where the MPL of rubrene and perovskite are separated. MPL in the bilayer films, glass/$MAPbI_3$/PMMA(20nm)/rubrene (100nm) when pumped with (c) 635 nm nm and (d) 405 nm. All data were taken at 10 K.

shape is essentially like what was observed in the pure rubrene film (**Figure 4.4b**) with two contributions from the low and high field effect. However, while the small field MPL has a similar magnitude, the large field MPL of 0.2% in the 50% blend is much weaker than about ~6% MPL in the pure rubrene film. This might be because the 50% rubrene film has better crystallinity than the pure rubrene film (see the **Figure 4.3a**) causing the suppressing of the large field effect.[193] The TTA-based MPL in rubrene films was shown to be strongly affected by the magnetic field dependent spin lattice relaxation.[193] The MPL of $MAPbI_3$ at different powers are shown in **Figure 4.6c**. Interestingly, the MPL with power larger than 10 mW does not show small field effect as shown in the rubrene case in **Figure 4.6b**. We rule out the scenario that that the MPL in $MAPbI_3$ is dominant the direct absorption of photons emitted from rubrene because if this is the case the MPL in $MAPbI_3$ would have a similar response as the MPL in rubrene. Our hypothesis is strengthened by the opposite MPL sign at small applied B when the pump power is less than 10 mW.

In order to have more control in the interfacial property between rubrene and $MAPbI_3$, we perform the MPL in the rubrene/$MAPbI_3$ bilayer film, where weaker energy/charge transfer occurs only at the interface between the two materials. **Figure 4.7a** show MPL of the bilayer film pumped at 635 nm laser with 5 mW power. We observed only PL spectrum from $MAPbI_3$. Interestingly, the MPL is small and positive. The magnitude of ~0.03% is smaller than what have been observed in the 2% and 25% rubrene films. This result might be because the interface between the materials has been substantially reduced causing a weaker charge and energy transfers. **Figure 4.7b** shows the MPL of rubrene and $MAPbI_3$ under the 405 nm laser excitation. Surprisingly, the MPL line shapes of rubrene and perovskite look essentially the same and the MPL in rubrene is two

orders of magnitude larger than that in $MAPbI_3$. The result implies that they have the same origin. Furthermore, they also look the same as the MPL response of rubrene in **Figure 4.4b** and **4.6b**. We conclude that the singlet excitons in rubrene in **Figure 4.7b** are manipulated by the magnetic field. When transferred to $MAPbI_3$ either by emitting a photon, or by Förster energy transfer, the single excitons in $MAPbI_3$ would have the same modulation as that in rubrene. Since the rubrene film is 100 nm thick, the Förster energy transfer might not be a major effect in this process since Förster energy transfer has an effective range of 10 nm only.

To completely eliminate the effect of the Förster, Dexter and charge transfer between the materials, we fabricated a 20 nm insulator, namely Poly(methyl methacrylate) (PMMA) between the perovskite and rubrene. Since 20 nm PMMA is thicker than the effective radius of Förster energy transfer, we would expect that the change in singlet excitons (MPL) in $MAPbI_3$ perovskite is only from the energy reabsorption process. **Figure 4.7c** show the MPL effect in $MAPbI_3$ emission under the 635 nm laser excitation. When rubrene and $MAPbI_3$ are decoupled, the MPL in the $MAPbI_3$ is exactly the same as the MPL in the pure $MAPbI_3$ thin film as shown in **Figure 4.4a**. This again reconfirm the energy transfers between two materials when they are coupled. **Figure 4.7d** shows the MPL of $MAPbI_3$ and rubrene when the film is excited by the 405 nm laser. The MPL in rubrene is nearly two orders of magnitude larger than that in $MAPbI_3$ but they have the same line shape due to the reabsorption process. We note that the small field effect in the trilayer film is much smaller than that in the bilayer films. This may be because the polycrystallinity of rubrene grown on perovskite is better than grown on PMMA.

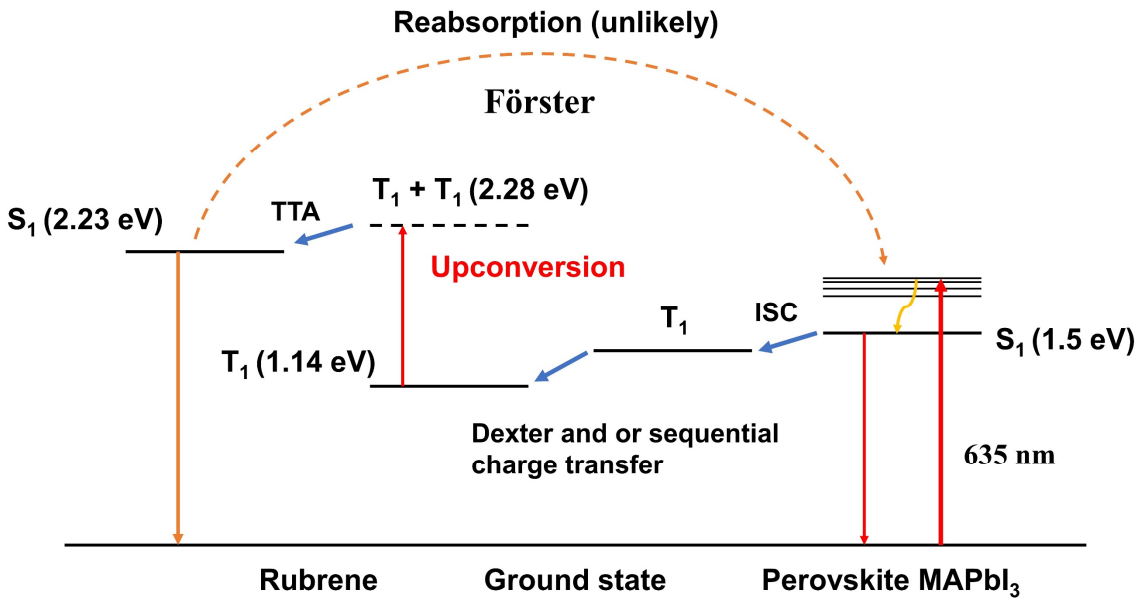

Figure 4.8. A simple diagram for the upconversion process in the rubrene/$MAPbI_3$ system when it is pumped with a 635 nm laser.

Based on the PL and MPL studies of the films, we suggest a model as shown in **Figure 4.8** for understanding the MPL and energy transfer between rubrene and $MAPbI_3$ perovskite. When the system is pumped by a 635 nm laser excitation, the singlet excitons are formed in $MAPbI_3$ that quickly relaxes to the lowest excited singlet excitons, S_1. A small portion of this excited states recombine radiatively to form photons. Most of them undergoes ISC to triplet states, T_1, and dissociate to loosely bound electron-hole pairs and free carriers. The formation of the triplet excitons, T_1, in rubrene can occur by either the short-range Dexter triplet energy transfer or by sequential electron-hole transfer although the latter is not as effective as in the system studied by Nienhaus *et al.*[172] The effective radius of these process is typically ~1 nm. After singlet excitons, S_1, in rubrene are formed by the triplet-triplet annihilation or singlet fusion, they are immediately transferred to singlet excitons, S_1, in the $MAPbI_3$ by the Förster energy transfer that has a long-range

interaction up to 10 nm and/or the reabsorption process. The reabsorption process is not effective since it would take several nanoseconds for the single excitons in rubrene to recombine radiatively while the Förster energy transfer occurs in the ps range.[189] In addition, within this reabsorption process time, slow intersystem crossing between singlet and triplet loosely electron–hole pair in rubrene would cause the magnetic field effect at the small field of ~5 mT caused by the hyperfine field. We barely observe this magnetic field effect. We note that the MPL of $MAPbI_3$ is dictated by the MPL of the rubrene triplet exciton density. In the strong interaction system (2% and 25% rubrene films), we found that the magnetic field effect on TCA process in rubrene is dominant while in the loosely coupled system, the magnetic field effect on TTA in rubrene is dominant. We observe the MPL in rubrene is about 2 orders of magnitude larger than that in perovskite. We find that the charge transfer is only effective in the low rubrene concentration blends. We note that the PMMA used in our experiment can simultaneously block the short-range Dexter energy transfer and sequential electron-hole charge transfer processes. Therefore, it is challenging to distinguish the main mechanism that produces the triplet excitons in rubrene.

4.4 CONCLUSION

By using PL and MPL studies of rubrene/$MAPbI_3$ thin film system, we are able to prove the energy upconversion in rubrene and the energy transfer between rubrene and $MAPbI_3$ in the system. In particular, we found that the major energy transfer from rubrene to $MAPbI_3$ is governed by the Förster energy transfer. Both the Dexter and charge transfer occurs in the system and might be equally important for existence of triplet excitons in rubrene. We observe two competitive magnetic field effect mechanisms happening in the system. In the strong interaction system (2% and 25% rubrene films), we found that the

magnetic field effect on TCA process is dominant while in the loosely coupled system, the magnetic field effect on TTA in rubrene is dominant. We note that MPL method can used to effectively investigate the energy downconversion/single fission process as well, as long as we can find a singlet fission molecule whose triplet energy is higher than that in the $MAPbI_3$.

CHAPTER 5

FUTURE WORK

5.1 SPIN HALL EFFECT

By using magnetic field effect and optical studies, we have found that a large Rashba-Dresselhaus field exists in the 2D RD perovskites. We plan to probe this field by another method, which is based on spin Hall effects.

Spin Hall effect (SHE) is a spin transport phenomenon predicted by Russian physicists Dyakonov and Perel in 1971.[197-198] It originates from the coupling of the charge and spin currents due to spin-orbit coupling. After 33 years, the SHE was experimentally observed by two group in Santa Barbara, US[4] and in Cambridge, UK.[199]

The SHE consists of spin accumulation at the lateral boundaries of a current-carrying conductor, the directions of the spins being opposite at the opposite boundaries. SHE is

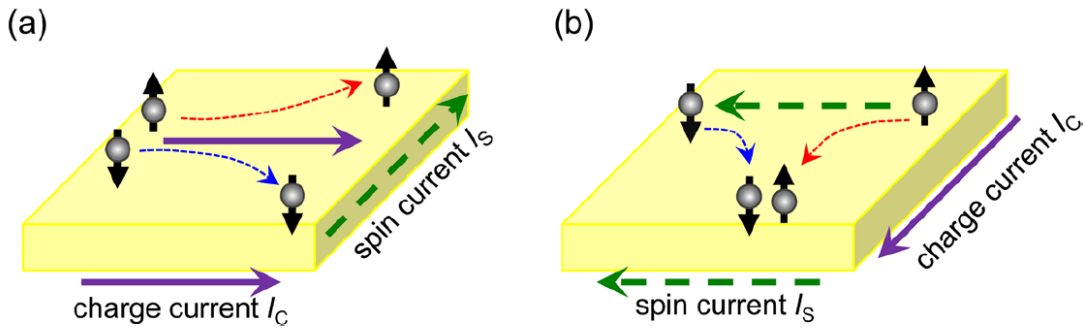

Figure 5.1. SHE and inverse SHE (ISHE). The solid, broken, and dotted arrows indicate the direction of electric charge current, spin current and the motions of spin-up and spin-down electrons. The figure is adopted from reference.[2]

somewhat similar to the normal Hall effect, where charges of opposite signs accumulate at the sample boundaries due to the action of the Lorentz force under applied magnetic field[200] but the SHE does not required an applied magnetic field.

Figure 5.1 depicts the SHE and inverse Spin Hall effect (ISHE). ISHE is the effect in which charge current is induced by a spin current. A spin current can be thought of as a combination of a current of spin-up electrons in one direction and a current of spin-down electrons in the opposite direction, resulting in a flow of spin angular momentum with no net charge current.

Two possible mechanisms have been proposed for understanding the origin of the SHE. The original one proposed by Dyakonov and Perel consists of spin-dependent Mott scattering, where opposite sign charge carriers diffuse in opposite directions when colliding with impurities in the material. The second mechanism is due to intrinsic properties of the materials, where the charge carriers' trajectories are distorted due to the spin-orbit coupling as a consequence of the asymmetry in the materials.[132] In HOIPs, especially 2D RD perovskites, strong Rashba-Dresselhaus SOC stem from bulk inversion asymmetry (BIA) and structure inversion asymmetry (SIA) were intensively studied in chapter 2 and chapter 3. Therefore, there is a high possibility of sizable SHE and ISHE observation in these materials.

An experimental tool for SHE is Kerr rotation microscopy which was used by Kato et al. to observe the SHE in unstrained gallium arsenide and strained indium gallium arsenide.[4] **Figure 5.2a** shows the schematic of the GaAs samples and experimental geometry. An external electric field E = 10 mV/μm is applied in y direction. **Figure 5.2f** presents the normalized reflectivity R signal as a function of x. The two dips indicate the

position of the edges and the width of the dips gives an approximate spatial resolution. **Figure 5.2c** presents the result of Kerr rotation color map with applied B and x position of

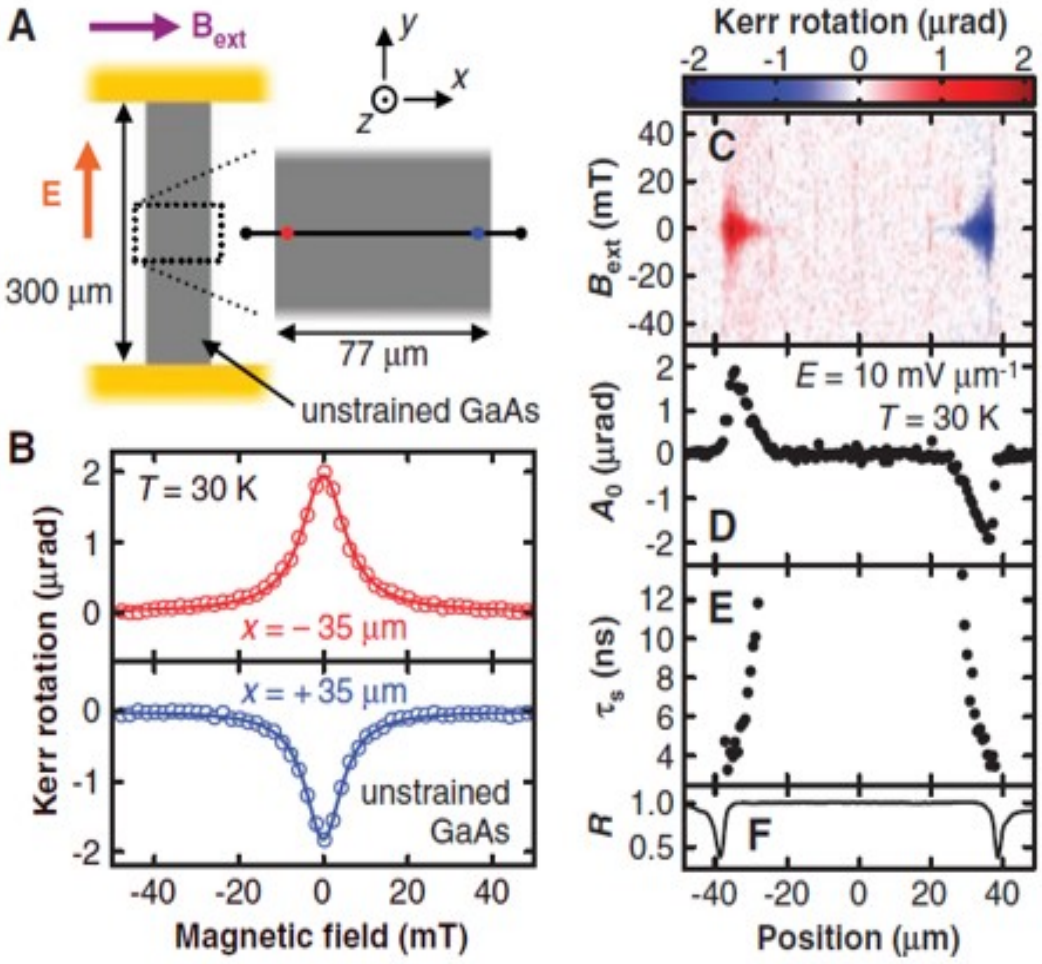

Figure 5.2. The spin Hall effect in GaAs (at 30K). (A) Schematic of the GaAs sample and the experimental geometry. (B) Measurement of Kerr rotation as a function of B_{ext} for x = -35 μm (red circles) and x = +35 μm (blue circles) for E = 10 mV μm^{-1}. Solid lines are fits. (C) Color map of Kerr rotation as a function of x and B_{ext} for E = 10 mV μm^{-1}. (D) and (E) Spatial dependence of peak Kerr rotation A_0 and spin lifetime τ_s, respectively, obtained from fits to data in (C). (F) Reflectivity R as a function of x. R is normalized to the value on the GaAs channel. The figure is adopted from the work of Kato et al.[4]

the measured point. **Figure 5.2b** and **5.2c** show that the opposite spins are accumulated at the two edges of the sample. The observation that Kerr rotation is largest when the applied magnetic field B = 0 proves the existence of the spin Hall effect as theoretical prediction. Moreover, when an external magnetic field in the x direction is applied, which is perpendicular to the spin polarization direction, it will destroy the spin polarization. As seen in **Figure 5.2b**, the Kerr rotation magnitude shows a Lorentzian curve with applied magnetic field B, which is known as the Hanle effect. From these curves, one can find out the spin lifetime as shown in **Figure 5.2e**.

Going forward, my plan is to perform this Kerr rotation experiment with the 2D RD HOIPs. I expect to observe the SHE in these materials, and from the results, we can obtain some fundamental information of the materials such as spin lifetime, g-factor and effective Rashba-Dresselhaus field.

APPENDIX A

3D $MAPbI_3$ and 2D Ruddlesden-Popper $(BA)_2(MA)_{n-1}Pb_nI_{3n+1}$ perovskites fabrication and characterization. (Dr. Eric Amerling from the university of Utah's work).

The fabrication procedure of the 3D MAPI and 2D Ruddlesdence-Popper perovskites is quite simple. All the chemical reactions were performed in a controlled atmosphere. Lead (II) oxide (PbO, ≥99.0% pure), n-butylamine ($CH_3(CH_2)_3NH_2$; 99.5% pure), and stabilized hydriodic acid (HI; 57 wt. % in H_2O, contains ≤1.5% H_3PO_4 acid as a stabilizer) were purchased from Sigma Aldrich and used without further purification. Methylammonium chloride (MACl) was purchased from Dyesol (now Greatcell Solar) and used without further purification. For the $MAPbI_3$ ($n = \infty$), 4.8 mmol (1.1 g) of PbO was dissolved in 10 mL of stabilized HI. The solution was then heated at 60°C and stirred until completely dissolved and brilliantly yellow. Then, 7.2 mmol (500 mg) of MACl was added to the solution which turned black instantly. The solution was left to stir for 30 min. Subsequently, a black precipitate was formed. Prior to any characterization, this precipitate was washed with cold ether and dried in a vacuum oven at 60 °C for 2 h.

For the synthesis of $(BA)_2(MA)_{n-1}Pb_nI_{3n+1}$ single crystal, stoichiometric amounts of PbO were dissolved in stabilized HI, heated mildly (60 °C), and stirred until completely dissolved and brilliantly yellow. MACl powder was subsequently added causing the solution to immediately turn black. After a few minutes of heating and stirring, the MACl was completely dissolved and the solution returned to a bright yellow state. Next, n-butylamine was added to the solution dropwise under vigorous stirring. The solution was

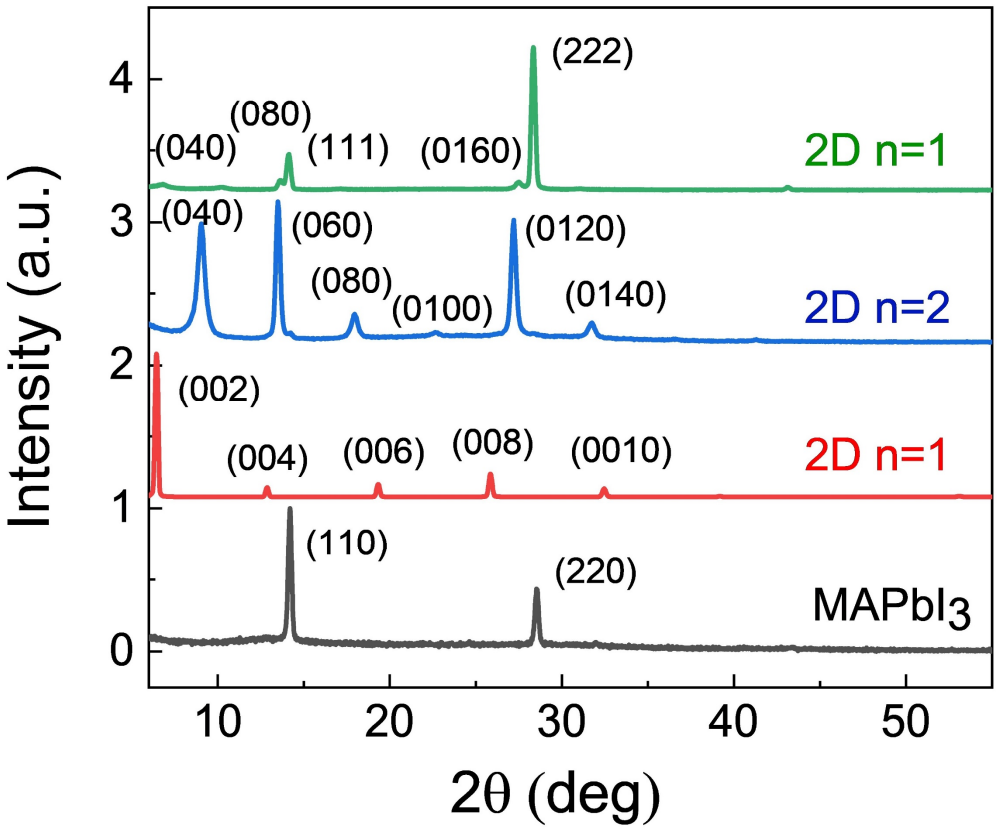

Figure A1. XRD of the 3D $MAPbI_3$ (black line) and 2D Ruddlesden-Popper perovskites with n=1, n=2 and n=3 (red, blue, and green line, respectively.) thin film deposited on glass substrates.

left to stir for 10 min. A molar 3:1 addition of NaI : PbI_2 (2.2 g) was added to prevent decomposition and formation of defective perovskite phases. Finally, 6 mL of glacial acetic acid was added to quench the reaction and form the desired product. Prior to any characterization, the precipitate was washed with cold ether and dried in a vacuum oven at 60 °C for 2 h. The exact amounts of each precursor used to yield the desired $(BA)_2(MA)_{n-1}Pb_nI_{3n+1}$ single crystal are summarized in **Table 2**. The single crystals of 2D RD and 3D perovskites were characterized with X-Ray Diffraction (XRD), the results are shown in

Figure A1 confirm a successful fabrication process that yields the same crystal's structure as reported.[20-21]

The 2D and 3D HOIP powders were dissolved in a dimethylformamide (DMF) solution to yield a 0.25 M concentration. All other fabrication steps were carried out in a nitrogen

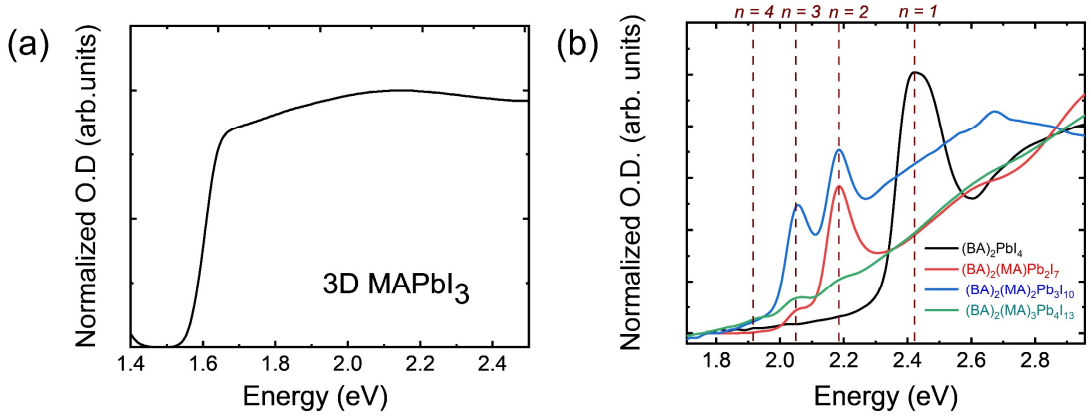

Figure A2. Broad absorption spectrum of the 3D $MAPbI_3$ (a) and absorption spectra of 2D Ruddlesden-Popper perovskite thin films (b). The UV-vis absorption spectrum for2D n=1 film shows a prominent band at 2.4 eV, which is corresponds to a strong exciton resonance. From n=2, the absorption spectrum shows evolution of a strong exciton band at ~2.2 eV and a weak second band at 2.0 eV. Dashed lines indicate exciton absorption resonances.

filled glovebox. Inside the glovebox, the perovskite solutions and glass substrates were preheated to 80°C for 30 min. Then the perovskite solution was spin coated onto the substrate at 5000 rpm for 30 s.

Absorption and photoluminescence spectra of the 3D $MAPbI_3$ and 2D Ruddlesden-Popper perovskites were collected and presented in **Figure A2** and **Figure A3**. The 3D $MAPbI_3$ thin film absorption shows a broad band from 1.6 eV, while the absorption of the 2D perovskites shows specific peaks associated to excitonic transition. Both absorption and

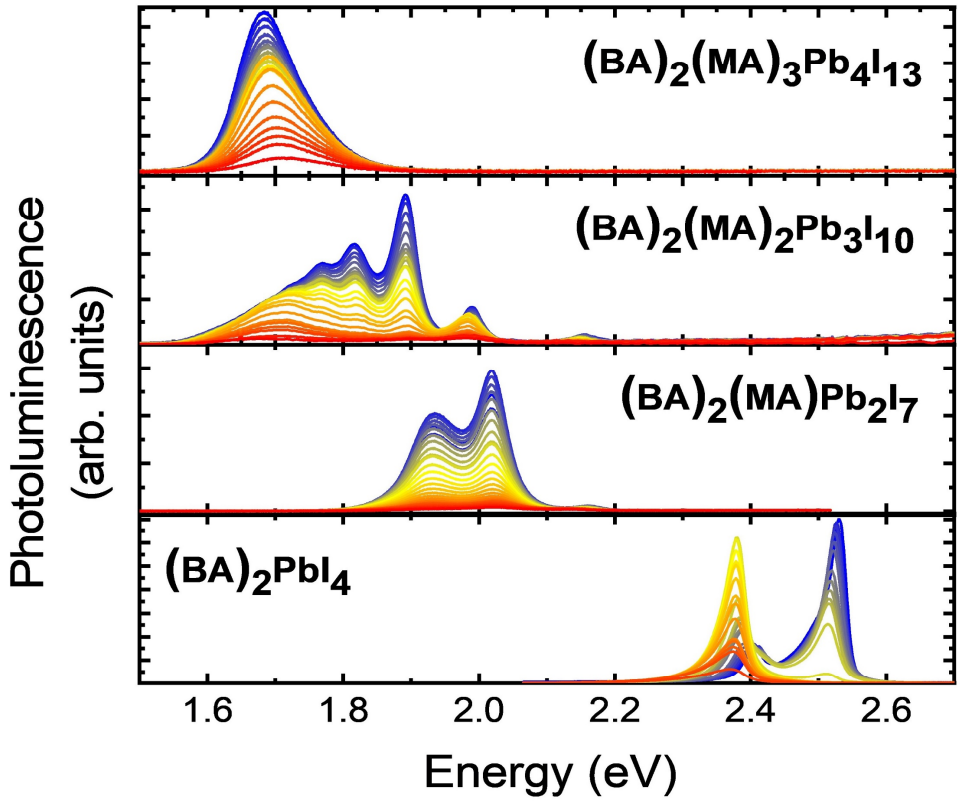

Figure A3. Photoluminescence spectra at various temperatures from 300 K (red) to 50 K (blue) for 2D Ruddlesden-Popper perovskites $(BA)_2(MA)_{n-1}Pb_nI_{3n+1}$ thin films with n = 1, 2, 3, and 4 (λ_{ex} = 405 nm).

photoluminescence spectra are similar to those reported in literature, indicate a successful material fabrication.[20]

Table 2 – Summary of precursors used for crystal growth of $BA_2MA_{n-1}Pb_nI_{3n+1}$ crystals.

		HI (mL)	PbO (g)	MACl(mg)	n-BA (uL)
n = 1	BA_2PbI_4	10	1.1	0	593

n = 2	$BA_2MAPb_2I_7$	10	1.1	162	238
n = 3	$BA_2MA_2Pb_3I_{10}$	10	1.1	216	158
n = 4	$BA_2MA_3Pb_4I_{13}$	10	1.1	243	79
n = ∞ (3D)	$MAPbI_3$	10	1.1	500	0

APPENDIX B

g-factor calculation from the MCD – B dependence measurement

One can estimate the splitting energy due to Zeeman effect by Gaussian fitting method.[117, 143-145] The splitting energy is:

$$\Delta E_{Zeeman} = \frac{2\sigma\Delta A}{A}$$

Where σ is the halfwidth of Gaussian fitting curve from absorption spectrum, ΔA and A are the MCD and absorption intensity at the excitonic transition, which can be obtained from **Figure 3.11c** and **Figure 3.11d**.

Table 1. Zeeman splitting energy calculation from equation (5) for the 2D RP perovskite thin film n = 1 and n = 2.

B applied (T)	MCD peak 2D n=1 (mdeg)	Zeeman splitting n=1 (meV)	MCD peak 2D n=2 (mdeg)	Zeeman splitting 2D n=2 (meV)
-1.77	278	0.309	122	0.298
-0.88	136	0.151	66	0.161
-0.44	52	0.057	33.8	0.082
-0.22	22	0.024	19.3	0.047
0.22	-34	-0.037	-13.4	-0.032
0.44	-59	-0.065	-26.8	-0.065
0.88	-135	-0.150	-63	-0.154
1.77	-236	-0.262	-138	-0.337

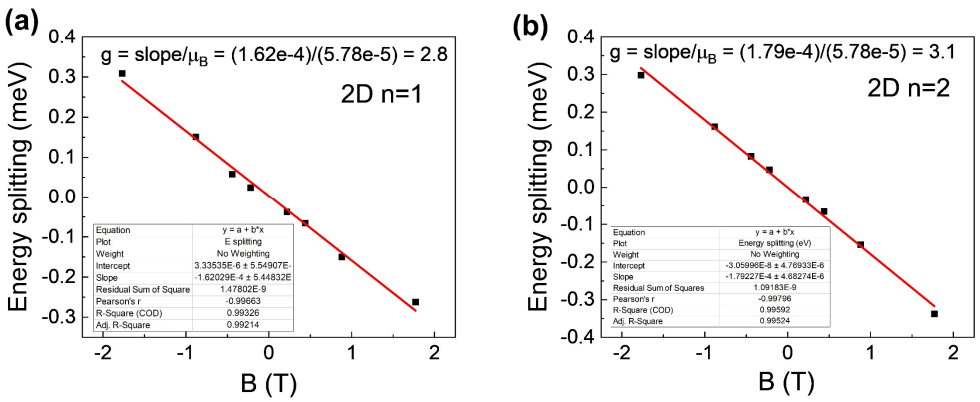

Figure B1. g factor calculation from the MCD measurement. (a) g = 2.8 for the 2D RP n = 1 and (b) g = 3.1 for the 2D RP n = 2.

APPENDIX C

Perovskite thin films thickness measured by the profilometer

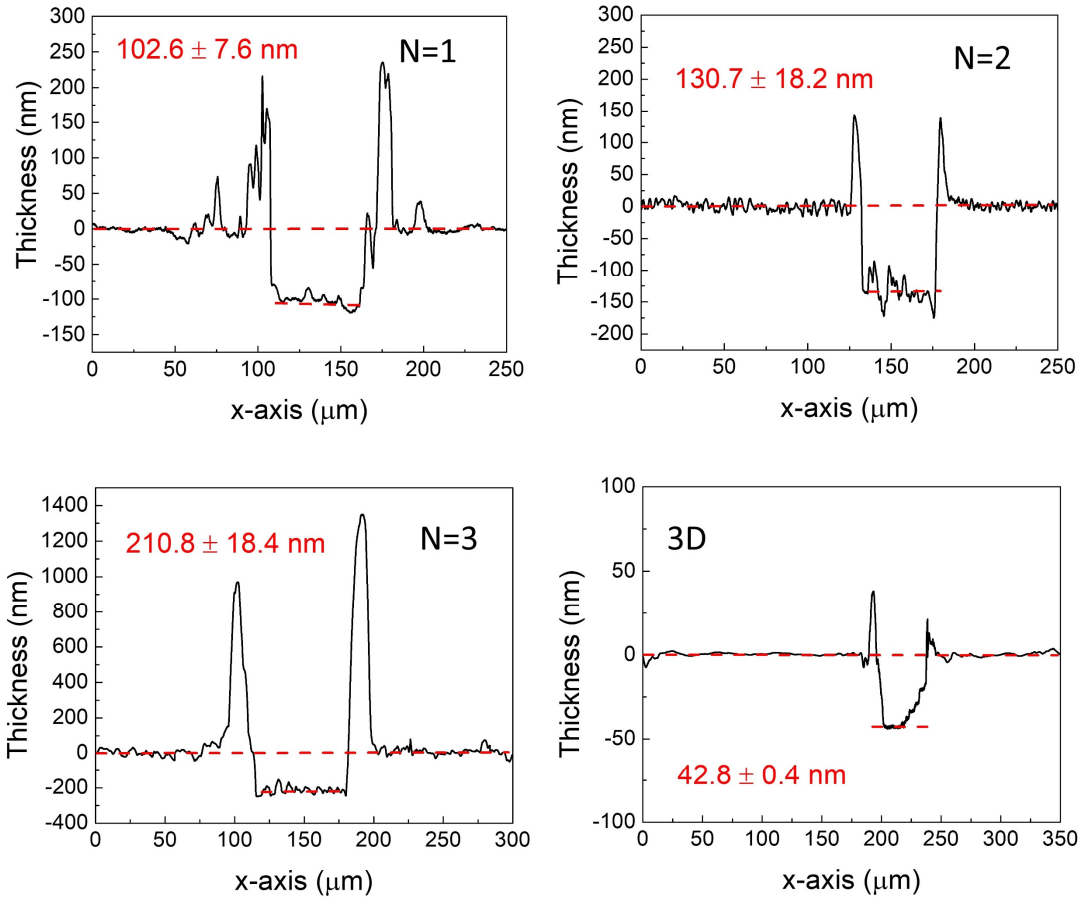

Figure C1. Perovskite thin films thickness measured by the profilometer.

Table 2. The highest Verdet constants of perovskite thin films and the transmittance at the correspomding wavelengths

Materials	Verdet constant (rad/T.m)	At wavelength (nm)	Transmittance (%)

3D perovskite	-595	752	62.8
3D perovskite	1121	788	69.6
2D n = 1	-7293	511	0.4
2D n = 1	8689	520	12.5
2D n = 2	-3695	566	8
2D n = 2	3801	582	29.5
2D n = 3	-873	600	20
2D n = 3	396	618	29.3
3D perovskite	34	632	53
2D n = 1	-	632	-
2D n = 2	2419	632	88
2D n = 3	77	632	36

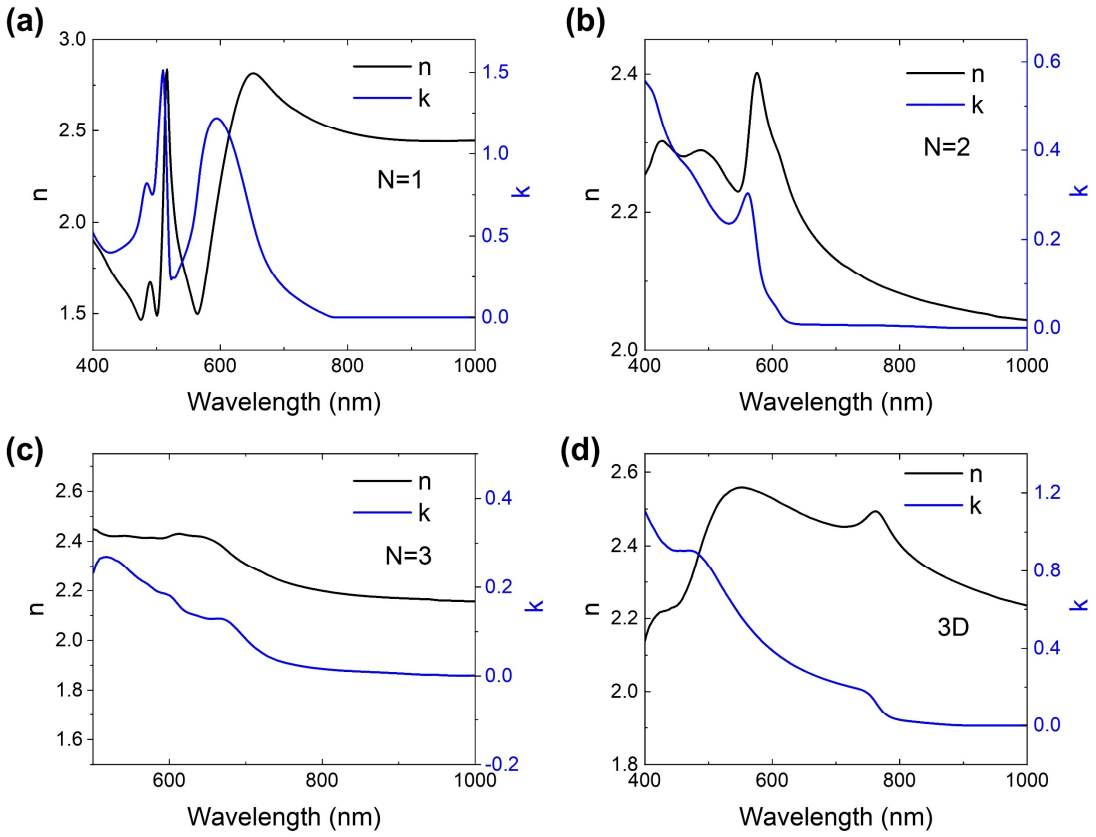

Figure C2. Refractive indices of the perovskite thin films measured by the ellipsometer.

REFERENCES

1. https://www.edinst.com/wp-content/uploads/2018/05/AN45_Phase-Transitions_Halide-Perovskites.pdf.

2. Niimi, Y.; Otani, Y., Reciprocal spin Hall effects in conductors with strong spin–orbit coupling: a review. *Reports on Progress in Physics* **2015,** *78* (12), 124501.

3. Nguyen, T. D.; Sheng, Y.; Rybicki, J.; Wohlgenannt, M., Magnetic field-effects in bipolar, almost hole-only and almost electron-only tris-(8-hydroxyquinoline) aluminum devices. *Physical Review B* **2008,** *77* (23), 235209.

4. Kato, Y. K.; Myers, R. C.; Gossard, A. C.; Awschalom, D. D., Observation of the Spin Hall Effect in Semiconductors. *Science* **2004,** *306* (5703), 1910.

5. Weber, D., CH3NH3PbX3, ein Pb(II)-System mit kubischer Perowskitstruktur / CH3NH3PbX3, a Pb(II)-System with Cubic Perovskite Structure. *Zeitschrift für Naturforschung B* **1978,** *33* (12), 1443-1445.

6. Ushakova, E. V.; Cherevkov, S. A.; Kuznetsova, V. A.; Baranov, A. V., Lead-Free Perovskites for Lighting and Lasing Applications: A Minireview. *Materials* **2019,** *12* (23).

7. Yuan, M.; Quan, L. N.; Comin, R.; Walters, G.; Sabatini, R.; Voznyy, O.; Hoogland, S.; Zhao, Y.; Beauregard, E. M.; Kanjanaboos, P.; Lu, Z.; Kim, D. H.; Sargent, E. H., Perovskite energy funnels for efficient light-emitting diodes. *Nature nanotechnology* **2016,** *11* (10), 872-877.

8. Liao, K.; Hu, X.; Cheng, Y.; Yu, Z.; Xue, Y.; Chen, Y.; Gong, Q., Spintronics of Hybrid Organic–Inorganic Perovskites: Miraculous Basis of Integrated Optoelectronic Devices. *Advanced Optical Materials* **2019,** *7* (15), 1900350.

9. Kojima, A.; Teshima, K.; Shirai, Y.; Miyasaka, T., Organometal Halide Perovskites as Visible-Light Sensitizers for Photovoltaic Cells. *Journal of the American Chemical Society* **2009,** *131* (17), 6050-6051.

10. De Leebeeck, A.; Kumar, L. K.; de Lange, V.; Sinton, D.; Gordon, R.; Brolo, A. G., On-chip surface-based detection with nanohole arrays. *Analytical chemistry* **2007,** *79* (11), 4094-100.

11. Dixon, A. E., 16 - PHOTOVOLTAIC ENERGY CONVERSION: THEORY, PRESENT AND FUTURE SOLAR CELLS. In *Solar Energy Conversion II*, Janzen, A. F.; Swartman, R. K., Eds. Pergamon: 1981; pp 243-259.

12. Ball, J. M.; Lee, M. M.; Hey, A.; Snaith, H. J., Low-temperature processed meso-superstructured to thin-film perovskite solar cells. *Energy & Environmental Science* **2013,** *6* (6), 1739-1743.

13. de Quilettes, D. W.; Vorpahl, S. M.; Stranks, S. D.; Nagaoka, H.; Eperon, G. E.; Ziffer, M. E.; Snaith, H. J.; Ginger, D. S., Impact of microstructure on local carrier lifetime in perovskite solar cells. *Science* **2015,** *348* (6235), 683-686.

14. Stranks, S. D.; Eperon, G. E.; Grancini, G.; Menelaou, C.; Alcocer, M. J. P.; Leijtens, T.; Herz, L. M.; Petrozza, A.; Snaith, H. J., Electron-Hole Diffusion Lengths Exceeding 1 Micrometer in an Organometal Trihalide Perovskite Absorber. *Science* **2013,** *342* (6156), 341-344.

15. Dong, Q.; Fang, Y.; Shao, Y.; Mulligan, P.; Qiu, J.; Cao, L.; Huang, J., Electron-hole diffusion lengths > 175 μm in solution-grown CH₃NH₃PbI₃ single crystals. *Science* **2015,** *347* (6225), 967-970.

16. Frohna, K.; Deshpande, T.; Harter, J.; Peng, W.; Barker, B. A.; Neaton, J. B.; Louie, S. G.; Bakr, O. M.; Hsieh, D.; Bernardi, M., Inversion symmetry and bulk Rashba effect in methylammonium lead iodide perovskite single crystals. *Nature Communications* **2018,** *9* (1), 1829.

17. Whitfield, P. S.; Herron, N.; Guise, W. E.; Page, K.; Cheng, Y. Q.; Milas, I.; Crawford, M. K., Structures, Phase Transitions and Tricritical Behavior of the Hybrid Perovskite Methyl Ammonium Lead Iodide. *Scientific Reports* **2016,** *6* (1), 35685.

18. Tsai, H.; Nie, W.; Blancon, J.-C.; Stoumpos, C. C.; Asadpour, R.; Harutyunyan, B.; Neukirch, A. J.; Verduzco, R.; Crochet, J. J.; Tretiak, S.; Pedesseau, L.; Even, J.; Alam, M. A.; Gupta, G.; Lou, J.; Ajayan, P. M.; Bedzyk, M. J.; Kanatzidis, M. G.; Mohite, A. D., High-efficiency two-dimensional Ruddlesden–Popper perovskite solar cells. *Nature* **2016,** *536* (7616), 312-316.

19. Blancon, J.-C.; Tsai, H.; Nie, W.; Stoumpos, C. C.; Pedesseau, L.; Katan, C.; Kepenekian, M.; Soe, C. M. M.; Appavoo, K.; Sfeir, M. Y.; Tretiak, S.; Ajayan, P. M.; Kanatzidis, M. G.; Even, J.; Crochet, J. J.; Mohite, A. D., Extremely efficient internal exciton dissociation through edge states in layered 2D perovskites. *Science* **2017,** *355* (6331), 1288-1292.

20. Cao, D. H.; Stoumpos, C. C.; Farha, O. K.; Hupp, J. T.; Kanatzidis, M. G., 2D Homologous Perovskites as Light-Absorbing Materials for Solar Cell Applications. *Journal of the American Chemical Society* **2015,** *137* (24), 7843-50.

21. Stoumpos, C. C.; Cao, D. H.; Clark, D. J.; Young, J.; Rondinelli, J. M.; Jang, J. I.; Hupp, J. T.; Kanatzidis, M. G., Ruddlesden–Popper Hybrid Lead Iodide Perovskite 2D Homologous Semiconductors. *Chemistry of Materials* **2016,** *28* (8), 2852-2867.

22. Blancon, J. C.; Stier, A. V.; Tsai, H.; Nie, W.; Stoumpos, C. C.; Traoré, B.; Pedesseau, L.; Kepenekian, M.; Katsutani, F.; Noe, G. T.; Kono, J.; Tretiak, S.; Crooker, S. A.; Katan, C.; Kanatzidis, M. G.; Crochet, J. J.; Even, J.; Mohite, A. D., Scaling law for excitons in 2D perovskite quantum wells. *Nature Communications* **2018,** *9* (1), 2254.

23. Gao, X.; Zhang, X.; Yin, W.; Wang, H.; Hu, Y.; Zhang, Q.; Shi, Z.; Colvin, V. L.; Yu, W. W.; Zhang, Y., Ruddlesden–Popper Perovskites: Synthesis and Optical Properties for Optoelectronic Applications. *Advanced Science* **2019,** *6* (22), 1900941.

24. Liang, C.; Gu, H.; Xia, Y.; Wang, Z.; Liu, X.; Xia, J.; Zuo, S.; Hu, Y.; Gao, X.; Hui, W.; Chao, L.; Niu, T.; Fang, M.; Lu, H.; Dong, H.; Yu, H.; Chen, S.; Ran, X.; Song, L.; Li, B.; Zhang, J.; Peng, Y.; Shao, G.; Wang, J.; Chen, Y.; Xing, G.; Huang, W., Two-dimensional Ruddlesden–Popper layered perovskite solar cells based on phase-pure thin films. *Nature Energy* **2021,** *6* (1), 38-45.

25. Niesner, D.; Wilhelm, M.; Levchuk, I.; Osvet, A.; Shrestha, S.; Batentschuk, M.; Brabec, C.; Fauster, T., Giant Rashba Splitting in CH_{3}NH_{3}PbBr_{3} Organic-Inorganic Perovskite. *Phys Rev Lett* **2016,** *117* (12), 126401.

26. Etienne, T.; Mosconi, E.; De Angelis, F., Dynamical Origin of the Rashba Effect in Organohalide Lead Perovskites: A Key to Suppressed Carrier Recombination in Perovskite Solar Cells? *The Journal of Physical Chemistry Letters* **2016,** *7* (9), 1638-1645.

27. Zhai, Y.; Baniya, S.; Zhang, C.; Li, J.; Haney, P.; Sheng, C.-X.; Ehrenfreund, E.; Vardeny, Z. V., Giant Rashba splitting in 2D organic-inorganic halide perovskites measured by transient spectroscopies. *Science Advances* **2017,** *3* (7), e1700704.

28. Niesner, D.; Hauck, M.; Shrestha, S.; Levchuk, I.; Matt, G. J.; Osvet, A.; Batentschuk, M.; Brabec, C.; Weber, H. B.; Fauster, T., Structural fluctuations cause spin-split states in tetragonal (CH₃NH₃)PbI₃ as evidenced by the circular photogalvanic effect. *Proceedings of the National Academy of Sciences* **2018,** *115* (38), 9509-9514.

29. Pais, A., George Uhlenbeck and the Discovery of Electron Spin. *Physics Today* **1989,** *42* (12), 34-40.

30. Thomas, L. H., The Motion of the Spinning Electron. *Nature* **1926,** *117* (2945), 514-514.

31. Shanavas, K. V.; Popović, Z. S.; Satpathy, S., Theoretical model for Rashba spin-orbit interaction in d electrons. *Physical Review B* **2014,** *90* (16), 165108.

32. Khaetskii, A.; Loss, D.; Glazman, L., Electron spin evolution induced by interaction with nuclei in a quantum dot. *Physical Review B* **2003,** *67* (19), 195329.

33. Geng, R.; Subedi, R. C.; Luong, H. M.; Pham, M. T.; Huang, W.; Li, X.; Hong, K.; Shao, M.; Xiao, K.; Hornak, L. A.; Nguyen, T. D., Effect of Charge Localization on the Effective Hyperfine Interaction in Organic Semiconducting Polymers. *Physical Review Letters* **2018,** *120* (8), 086602.

34. Dresselhaus, G., Spin-Orbit Coupling Effects in Zinc Blende Structures. *Physical Review* **1955,** *100* (2), 580-586.

35. Bychkov, Y. A.; Rashba, E. I., Oscillatory effects and the magnetic susceptibility of carriers in inversion layers. *Journal of Physics C: Solid State Physics* **1984,** *17* (33), 6039-6045.

36. Jana, M. K.; Song, R.; Liu, H.; Khanal, D. R.; Janke, S. M.; Zhao, R.; Liu, C.; Valy Vardeny, Z.; Blum, V.; Mitzi, D. B., Organic-to-inorganic structural chirality transfer in a 2D hybrid perovskite and impact on Rashba-Dresselhaus spin-orbit coupling. *Nature Communications* **2020,** *11* (1), 4699.

37. Kepenekian, M.; Robles, R.; Katan, C.; Sapori, D.; Pedesseau, L.; Even, J., Rashba and Dresselhaus Effects in Hybrid Organic–Inorganic Perovskites: From Basics to Devices. *ACS Nano* **2015,** *9* (12), 11557-11567.

38. Rashba, E. I., Quantum nanostructures in strongly spin-orbit coupled two-dimensional systems. *Physical Review B* **2012,** *86* (12), 125319.

39. Manchon, A.; Koo, H. C.; Nitta, J.; Frolov, S. M.; Duine, R. A., New perspectives for Rashba spin–orbit coupling. *Nature Materials* **2015,** *14*, 871.

40. Mosconi, E.; Etienne, T.; De Angelis, F., Rashba Band Splitting in Organohalide Lead Perovskites: Bulk and Surface Effects. *The Journal of Physical Chemistry Letters* **2017,** *8* (10), 2247-2252.

41. Even, J.; Pedesseau, L.; Jancu, J.-M.; Katan, C., Importance of Spin–Orbit Coupling in Hybrid Organic/Inorganic Perovskites for Photovoltaic Applications. *The Journal of Physical Chemistry Letters* **2013,** *4* (17), 2999-3005.

42. Kepenekian, M.; Even, J., Rashba and Dresselhaus Couplings in Halide Perovskites: Accomplishments and Opportunities for Spintronics and Spin–Orbitronics. *The Journal of Physical Chemistry Letters* **2017,** *8* (14), 3362-3370.

43. Hutter, E. M.; Gélvez-Rueda, M. C.; Osherov, A.; Bulović, V.; Grozema, F. C.; Stranks, S. D.; Savenije, T. J., Direct–indirect character of the bandgap in methylammonium lead iodide perovskite. *Nature Materials* **2016,** *16*, 115.

44. Niesner, D.; Wilhelm, M.; Levchuk, I.; Osvet, A.; Shrestha, S.; Batentschuk, M.; Brabec, C.; Fauster, T., Giant Rashba Splitting in ${\mathrm{CH}}_{3}{\mathrm{NH}}_{3}{\mathrm{PbBr}}_{3}$ Organic-Inorganic Perovskite. *Physical Review Letters* **2016,** *117* (12), 126401.

45. Niesner, D.; Hauck, M.; Shrestha, S.; Levchuk, I.; Matt, G. J.; Osvet, A.; Batentschuk, M.; Brabec, C.; Weber, H. B.; Fauster, T., Structural fluctuations cause spin-split states in tetragonal (CH₃NH₃)PbI₃ as evidenced by the circular photogalvanic effect. **2018,** *115* (38), 9509-9514.

46. Koo, H. C.; Kwon, J. H.; Eom, J.; Chang, J.; Han, S. H.; Johnson, M., Control of Spin Precession in a Spin-Injected Field Effect Transistor. *Science* **2009,** *325* (5947), 1515-1518.

47. Takase, K.; Ashikawa, Y.; Zhang, G.; Tateno, K.; Sasaki, S., Highly gate-tuneable Rashba spin-orbit interaction in a gate-all-around InAs nanowire metal-oxide-semiconductor field-effect transistor. *Scientific Reports* **2017,** *7* (1), 930.

48. Wang, G.; Liu, B. L.; Balocchi, A.; Renucci, P.; Zhu, C. R.; Amand, T.; Fontaine, C.; Marie, X., Gate control of the electron spin-diffusion length in semiconductor quantum wells. *Nature Communications* **2013,** *4* (1), 2372.

49. https://patents.google.com/patent/US3293513A/en.

50. Tang, C. W.; VanSlyke, S. A., Organic electroluminescent diodes. *Applied Physics Letters* **1987,** *51* (12), 913-915.

51. Woon Park, J., 19 - Large-area OLED lighting panels and their applications. In *Organic Light-Emitting Diodes (OLEDs)*, Buckley, A., Ed. Woodhead Publishing: 2013; pp 572-600.

52. Prasad, S., 18 - OLED-based biochemical sensors. In *Organic Light-Emitting Diodes (OLEDs)*, Buckley, A., Ed. Woodhead Publishing: 2013; pp 548-571.

53. Meyer, J.; Görrn, P.; Riedl, T., 17 - Transparent OLED displays. In *Organic Light-Emitting Diodes (OLEDs)*, Buckley, A., Ed. Woodhead Publishing: 2013; pp 512-547.

54. Lääperi, A., 15 - Active matrix, organic light-emitting diodes (AMOLEDs) for displays. In *Organic Light-Emitting Diodes (OLEDs)*, Buckley, A., Ed. Woodhead Publishing: 2013; pp 445-458.

55. Thejo Kalyani, N.; Dhoble, S. J., Organic light emitting diodes: Energy saving lighting technology—A review. *Renewable and Sustainable Energy Reviews* **2012,** *16* (5), 2696-2723.

56. Geng, R.; Daugherty, T. T.; Do, K.; Luong, H. M.; Nguyen, T. D., A review on organic spintronic materials and devices: I. Magnetic field effect on organic light emitting diodes. *Journal of Science: Advanced Materials and Devices* **2016,** *1* (2), 128-140.

57. Hung, L. S.; Tang, C. W.; Mason, M. G., Enhanced electron injection in organic electroluminescence devices using an Al/LiF electrode. *Applied Physics Letters* **1997,** *70* (2), 152-154.

58. Friend, R. H.; Gymer, R. W.; Holmes, A. B.; Burroughes, J. H.; Marks, R. N.; Taliani, C.; Bradley, D. D. C.; Santos, D. A. D.; Brédas, J. L.; Lögdlund, M.; Salaneck, W. R., Electroluminescence in conjugated polymers. *Nature* **1999,** *397* (6715), 121-128.

59. Pope, M.; Swenberg, C. In *Electronic Processes in Organic Crystals and Polymers*, 1999.

60. Hu, B.; Yan, L.; Shao, M., Magnetic-Field Effects in Organic Semiconducting Materials and Devices. *Advanced Materials* **2009,** *21* (14-15), 1500-1516.

61. Huang, Q. F.; Fu, R. T.; Fu, R. L.; Ye, H. J.; George, T. F.; Sun, X., Exciton and excitonic polaron in C60. *Synthetic Metals* **1995,** *70* (1), 1507-1508.

62. Fox, M., *Optical properties of solids / Mark Fox*. Second edition. ed.; Oxford University Press: Oxford [U.K.] ;, 2010.

63. Yang, Z.; Surrente, A.; Galkowski, K.; Bruyant, N.; Maude, D. K.; Haghighirad, A. A.; Snaith, H. J.; Plochocka, P.; Nicholas, R. J., Unraveling the Exciton Binding Energy and the Dielectric Constant in Single-Crystal Methylammonium Lead Triiodide Perovskite. *The Journal of Physical Chemistry Letters* **2017,** *8* (8), 1851-1855.

64. Baranowski, M.; Galkowski, K.; Surrente, A.; Urban, J.; Kłopotowski, Ł.; Maćkowski, S.; Maude, D. K.; Ben Aich, R.; Boujdaria, K.; Chamarro, M.; Testelin, C.; Nayak, P. K.; Dollmann, M.; Snaith, H. J.; Nicholas, R. J.; Plochocka, P., Giant Fine Structure Splitting of the Bright Exciton in a Bulk MAPbBr3 Single Crystal. *Nano letters* **2019,** *19* (10), 7054-7061.

65. Tilchin, J.; Dirin, D. N.; Maikov, G. I.; Sashchiuk, A.; Kovalenko, M. V.; Lifshitz, E., Hydrogen-like Wannier–Mott Excitons in Single Crystal of Methylammonium Lead Bromide Perovskite. *ACS Nano* **2016,** *10* (6), 6363-6371.

66. Frankevich, E. L.; Lymarev, A. A.; Sokolik, I.; Karasz, F. E.; Blumstengel, S.; Baughman, R. H.; Hörhold, H. H., Polaron-pair generation in poly(phenylene vinylenes). *Physical Review B* **1992,** *46* (15), 9320-9324.

67. Niedermeier, U.,

Magnetic field effect in organic light emitting diodes. **2010**.

68. Cho, H.; Jeong, S.-H.; Park, M.-H.; Kim, Y.-H.; Wolf, C.; Lee, C.-L.; Heo, J. H.; Sadhanala, A.; Myoung, N.; Yoo, S.; Im, S. H.; Friend, R. H.; Lee, T.-W., Overcoming the electroluminescence efficiency limitations of perovskite light-emitting diodes. *Science* **2015,** *350* (6265), 1222-1225.

69. Tan, Z.-K.; Moghaddam, R. S.; Lai, M. L.; Docampo, P.; Higler, R.; Deschler, F.; Price, M.; Sadhanala, A.; Pazos, L. M.; Credgington, D.; Hanusch, F.; Bein, T.; Snaith, H. J.; Friend, R. H., Bright light-emitting diodes based on organometal halide perovskite. *Nature nanotechnology* **2014,** *9* (9), 687-692.

70. Lin, K.; Xing, J.; Quan, L. N.; de Arquer, F. P. G.; Gong, X.; Lu, J.; Xie, L.; Zhao, W.; Zhang, D.; Yan, C.; Li, W.; Liu, X.; Lu, Y.; Kirman, J.; Sargent, E. H.; Xiong, Q.; Wei, Z., Perovskite light-emitting diodes with external quantum efficiency exceeding 20 per cent. *Nature* **2018,** *562* (7726), 245-248.

71. Cao, Y.; Wang, N.; Tian, H.; Guo, J.; Wei, Y.; Chen, H.; Miao, Y.; Zou, W.; Pan, K.; He, Y.; Cao, H.; Ke, Y.; Xu, M.; Wang, Y.; Yang, M.; Du, K.; Fu, Z.; Kong, D.; Dai, D.; Jin, Y.; Li, G.; Li, H.; Peng, Q.; Wang, J.; Huang, W., Perovskite light-emitting diodes based on spontaneously formed submicrometre-scale structures. *Nature* **2018,** *562* (7726), 249-253.

72. Zhao, B.; Bai, S.; Kim, V.; Lamboll, R.; Shivanna, R.; Auras, F.; Richter, J. M.; Yang, L.; Dai, L.; Alsari, M.; She, X.-J.; Liang, L.; Zhang, J.; Lilliu, S.; Gao, P.; Snaith, H. J.; Wang, J.; Greenham, N. C.; Friend, R. H.; Di, D., High-efficiency perovskite–polymer bulk heterostructure light-emitting diodes. *Nature Photonics* **2018,** *12* (12), 783-789.

73. Kalinowski, J.; Szmytkowski, J.; Stampor, W., Magnetic hyperfine modulation of charge photogeneration in solid films of Alq3. *Chemical Physics Letters* **2003,** *378* (3), 380-387.

74. Nguyen, T. D.; Hukic-Markosian, G.; Wang, F.; Wojcik, L.; Li, X.-G.; Ehrenfreund, E.; Vardeny, Z. V., Isotope effect in spin response of π-conjugated polymer films and devices. *Nature Materials* **2010,** *9* (4), 345-352.

75. Xiong, Z. H.; Wu, D.; Valy Vardeny, Z.; Shi, J., Giant magnetoresistance in organic spin-valves. *Nature* **2004,** *427* (6977), 821-824.

76. Hu, B.; Wu, Y., Tuning magnetoresistance between positive and negative values in organic semiconductors. *Nature Materials* **2007,** *6* (12), 985-991.

77. Mermer, Ö.; Veeraraghavan, G.; Francis, T. L.; Sheng, Y.; Nguyen, D. T.; Wohlgenannt, M.; Köhler, A.; Al-Suti, M. K.; Khan, M. S., Large magnetoresistance in nonmagnetic $\ensuremath{\pi}$-conjugated semiconductor thin film devices. *Physical Review B* **2005,** *72* (20), 205202.

78. Nguyen, T. D.; Sheng, Y.; Rybicki, J.; Veeraraghavan, G.; Wohlgenannt, M., Magnetoresistance in π-conjugated organic sandwich devices with varying hyperfine and spin–orbit coupling strengths, and varying dopant concentrations. *Journal of Materials Chemistry* **2007,** *17* (19), 1995-2001.

79. Wakasa, M.; Nishizawa, K.; Abe, H.; Kido, G.; Hayashi, H., Magnetic Field Effects Due to the Δg Mechanism upon Chemical Reactions through Radical Pairs under Ultrahigh Fields of up to 30 T. *Journal of the American Chemical Society* **1999,** *121* (39), 9191-9197.

80. Nikiforov, D.; Khachatryan, B.; Tilchin, J.; Lifshitz, E.; Tessler, N.; Ehrenfreund, E., Effect of g-factor anisotropy in the magnetoresponse of organic light-emitting diodes at high magnetic fields. *Physical Review B* **2018,** *98* (23), 235204.

81. Zhang, C.; Sun, D.; Sheng, C. X.; Zhai, Y. X.; Mielczarek, K.; Zakhidov, A.; Vardeny, Z. V., Magnetic field effects in hybrid perovskite devices. *Nat Phys* **2015,** *11* (5), 428-435.

82. Sheng, Y.; Nguyen, T. D.; Veeraraghavan, G.; Mermer, Ö.; Wohlgenannt, M.; Qiu, S.; Scherf, U., Hyperfine interaction and magnetoresistance in organic semiconductors. *Physical Review B* **2006,** *74* (4), 045213.

83. Wang, F. J.; Bässler, H.; Valy Vardeny, Z., Magnetic Field Effects in $\ensuremath{\pi}$-Conjugated Polymer-Fullerene Blends: Evidence for Multiple Components. *Physical Review Letters* **2008,** *101* (23), 236805.

84. Pham, M. T.; Amerling, E.; Luong, H. M.; Pham, H. T.; Larsen, G. K.; Whittaker-Brooks, L.; Nguyen, T. D., Origin of Rashba Spin-Orbit Coupling in 2D and 3D Lead Iodide Perovskites. *Scientific Reports* **2020,** *10* (1), 4964.

85. Yu-Che, H.; Ting, W.; Mingxing, L.; Bin, H., Magneto-Optical Studies on Spin-Dependent Charge Recombination and Dissociation in Perovskite Solar Cells. *Advanced Materials* **2015,** *27* (18), 2899-2906.

86. Wang, J.; Zhang, C.; Liu, H.; McLaughlin, R.; Zhai, Y.; Vardeny, S. R.; Liu, X.; McGill, S.; Semenov, D.; Guo, H.; Tsuchikawa, R.; Deshpande, V. V.; Sun, D.; Vardeny,

Z. V., Spin-optoelectronic devices based on hybrid organic-inorganic trihalide perovskites. *Nature Communications* **2019,** *10* (1), 129.

87. Pan, X.; Liu, H.; Huynh, U.; Vardeny, Z. V., Magneto-electroluminescence response in 2D and 3D hybrid organic–inorganic perovskite light emitting diodes. *The Journal of Chemical Physics* **2020,** *152* (4), 044714.

88. Hsiao, Y.-C.; Wu, T.; Li, M.; Hu, B., Magneto-Optical Studies on Spin-Dependent Charge Recombination and Dissociation in Perovskite Solar Cells. *Advanced Materials* **2015,** *27* (18), 2899-2906.

89. Parker, I. D., Carrier tunneling and device characteristics in polymer light-emitting diodes. *Journal of Applied Physics* **1994,** *75* (3), 1656-1666.

90. Coropceanu, V.; Cornil, J.; da Silva Filho, D. A.; Olivier, Y.; Silbey, R.; Brédas, J.-L., Charge Transport in Organic Semiconductors. *Chemical Reviews* **2007,** *107* (4), 926-952.

91. Cox, M.; Janssen, P.; Zhu, F.; Koopmans, B., Traps and trions as origin of magnetoresistance in organic semiconductors. *Physical Review B* **2013,** *88* (3), 035202.

92. Bloom, F. L.; Wagemans, W.; Kemerink, M.; Koopmans, B., Separating Positive and Negative Magnetoresistance in Organic Semiconductor Devices. *Physical Review Letters* **2007,** *99* (25), 257201.

93. Prigodin, V. N.; Bergeson, J. D.; Lincoln, D. M.; Epstein, A. J., Anomalous room temperature magnetoresistance in organic semiconductors. *Synthetic Metals* **2006,** *156* (9), 757-761.

94. Sheng, Y.; Nguyen, T. D.; Veeraraghavan, G.; Mermer, Ö.; Wohlgenannt, M., Effect of spin-orbit coupling on magnetoresistance in organic semiconductors. *Physical Review B* **2007,** *75* (3), 035202.

95. Subedi, R. C.; Geng, R.; Luong, H. M.; Huang, W.; Li, X.; Hornak, L. A.; Nguyen, T. D., Large magnetoelectric effect in organic ferroelectric copolymer-based multiferroic tunnel junctions. *Applied Physics Letters* **2017,** *110* (5), 053302.

96. Yu, Z.-G., Estimation of the Rashba Strength from Second Harmonic Generation in 2D and 3D Hybrid Organic–Inorganic Perovskites. *The Journal of Physical Chemistry C* **2018,** *122* (51), 29607-29612.

97. Devir-Wolfman, A. H.; Khachatryan, B.; Gautam, B. R.; Tzabary, L.; Keren, A.; Tessler, N.; Vardeny, Z. V.; Ehrenfreund, E., Short-lived charge-transfer excitons in organic photovoltaic cells studied by high-field magneto-photocurrent. *Nature Communications* **2014,** *5* (1), 4529.

98. Onoda-Yamamuro, N.; Matsuo, T.; Suga, H., Dielectric study of CH3NH3PbX3 (X = Cl, Br, I). *Journal of Physics and Chemistry of Solids* **1992,** *53* (7), 935-939.

99. Lin, Q.; Armin, A.; Nagiri, R. C. R.; Burn, P. L.; Meredith, P., Electro-optics of perovskite solar cells. *Nature Photonics* **2014,** *9*, 106.

100. Gundogdu, K., *Efficient triplet exciton generation in hybrid perovskites (Conference Presentation)*. SPIE: 2017; Vol. 10380.

101. Riehl, J. P.; Richardson, F. S., Circularly polarized luminescence spectroscopy. *Chemical Reviews* **1986,** *86* (1), 1-16.

102. Long, G.; Sabatini, R.; Saidaminov, M. I.; Lakhwani, G.; Rasmita, A.; Liu, X.; Sargent, E. H.; Gao, W., Chiral-perovskite optoelectronics. *Nature Reviews Materials* **2020,** *5* (6), 423-439.

103. Luong, H. M.; Ai, B.; Zhao, Y.; Nguyen, T. D., Weak enhanced resonant Faraday rotation in pure cobalt plasmonic lattices: Thickness dependent Faraday rotation studies. *Journal of Magnetism and Magnetic Materials* **2018,** *468*, 79-84.

104. Luong, H. M.; Pham, M. T.; Nguyen, T. D.; Zhao, Y., Enhanced Resonant Faraday Rotation in Multilayer Magnetoplasmonic Nanohole Arrays and Their Sensing Application. *The Journal of Physical Chemistry C* **2019,** *123* (46), 28377-28384.

105. Brewster, J. H., Organic Conformational Analysis and Stereochemistry from Circular Dichroism Spectroscopy by David A. Lightner (University of Nevada) and Jerome E. Gurst (University of West Florida). Wiley-VCH: New York. 2000. xvi + 488 pp. $94.95. ISBN: 0-471-35405-8. *Journal of the American Chemical Society* **2002,** *124* (12), 3186-3187.

106. Polavarapu, P. L., Kramers−Kronig Transformation for Optical Rotatory Dispersion Studies. *The Journal of Physical Chemistry A* **2005,** *109* (32), 7013-7023.

107. Larson, S.; Carlson, D.; Ai, B.; Zhao, Y., The extraordinary optical transmission and sensing properties of Ag/Ti composite nanohole arrays. *Physical Chemistry Chemical Physics* **2019,** *21* (7), 3771-3780.

108. Burschka, J.; Pellet, N.; Moon, S.-J.; Humphry-Baker, R.; Gao, P.; Nazeeruddin, M. K.; Grätzel, M., Sequential deposition as a route to high-performance perovskite-sensitized solar cells. *Nature* **2013,** *499* (7458), 316-319.

109. Brenner, T. M.; Egger, D. A.; Kronik, L.; Hodes, G.; Cahen, D., Hybrid organic—inorganic perovskites: low-cost semiconductors with intriguing charge-transport properties. *Nature Reviews Materials* **2016,** *1* (1), 15007.

110. Baranowski, M.; Plochocka, P., Excitons in Metal-Halide Perovskites. *Advanced Energy Materials* **2020,** *10* (26), 1903659.

111. Stranks, S. D.; Burlakov, V. M.; Leijtens, T.; Ball, J. M.; Goriely, A.; Snaith, H. J., Recombination Kinetics in Organic-Inorganic Perovskites: Excitons, Free Charge, and Subgap States. *Physical Review Applied* **2014,** *2* (3), 034007.

112. Ahn, J.; Lee, E.; Tan, J.; Yang, W.; Kim, B.; Moon, J., A new class of chiral semiconductors: chiral-organic-molecule-incorporating organic–inorganic hybrid perovskites. *Materials Horizons* **2017,** *4* (5), 851-856.

113. Long, G.; Jiang, C.; Sabatini, R.; Yang, Z.; Wei, M.; Quan, L. N.; Liang, Q.; Rasmita, A.; Askerka, M.; Walters, G.; Gong, X.; Xing, J.; Wen, X.; Quintero-Bermudez, R.; Yuan, H.; Xing, G.; Wang, X. R.; Song, D.; Voznyy, O.; Zhang, M.; Hoogland, S.; Gao, W.; Xiong, Q.; Sargent, E. H., Spin control in reduced-dimensional chiral perovskites. *Nature Photonics* **2018,** *12* (9), 528-533.

114. Ma, J.; Fang, C.; Chen, C.; Jin, L.; Wang, J.; Wang, S.; Tang, J.; Li, D., Chiral 2D Perovskites with a High Degree of Circularly Polarized Photoluminescence. *ACS Nano* **2019,** *13* (3), 3659-3665.

115. Dong, Y.; Zhang, Y.; Li, X.; Feng, Y.; Zhang, H.; Xu, J., Chiral Perovskites: Promising Materials toward Next-Generation Optoelectronics. *Small* **2019,** *15* (39), 1902237.

116. Ahn, J.; Ma, S.; Kim, J.-Y.; Kyhm, J.; Yang, W.; Lim, J. A.; Kotov, N. A.; Moon, J., Chiral 2D Organic Inorganic Hybrid Perovskite with Circular Dichroism Tunable Over Wide Wavelength Range. *Journal of the American Chemical Society* **2020,** *142* (9), 4206-4212.

117. Lu, H.; Wang, J.; Xiao, C.; Pan, X.; Chen, X.; Brunecky, R.; Berry, J. J.; Zhu, K.; Beard, M. C.; Vardeny, Z. V., Spin-dependent charge transport through 2D chiral hybrid lead-iodide perovskites. *Science Advances* **2019,** *5* (12), eaay0571.

118. Wang, J.; Fang, C.; Ma, J.; Wang, S.; Jin, L.; Li, W.; Li, D., Aqueous Synthesis of Low-Dimensional Lead Halide Perovskites for Room-Temperature Circularly Polarized Light Emission and Detection. *ACS Nano* **2019,** *13* (8), 9473-9481.

119. Tohgha, U.; Deol, K. K.; Porter, A. G.; Bartko, S. G.; Choi, J. K.; Leonard, B. M.; Varga, K.; Kubelka, J.; Muller, G.; Balaz, M., Ligand Induced Circular Dichroism and Circularly Polarized Luminescence in CdSe Quantum Dots. *ACS Nano* **2013,** *7* (12), 11094-11102.

120. Georgieva, Z. N.; Bloom, B. P.; Ghosh, S.; Waldeck, D. H., Imprinting Chirality onto the Electronic States of Colloidal Perovskite Nanoplatelets. *Advanced Materials* **2018,** *30* (23), 1800097.

121. Cao, T.; Wang, G.; Han, W.; Ye, H.; Zhu, C.; Shi, J.; Niu, Q.; Tan, P.; Wang, E.; Liu, B.; Feng, J., Valley-selective circular dichroism of monolayer molybdenum disulphide. *Nature Communications* **2012,** *3* (1), 887.

122. Rivera, P.; Seyler, K. L.; Yu, H.; Schaibley, J. R.; Yan, J.; Mandrus, D. G.; Yao, W.; Xu, X., Valley-polarized exciton dynamics in a 2D semiconductor heterostructure. *Science* **2016,** *351* (6274), 688-691.

123. Mukhina, M. V.; Maslov, V. G.; Baranov, A. V.; Fedorov, A. V.; Orlova, A. O.; Purcell-Milton, F.; Govan, J.; Gun'ko, Y. K., Intrinsic Chirality of CdSe/ZnS Quantum Dots and Quantum Rods. *Nano Letters* **2015,** *15* (5), 2844-2851.

124. Sercel, P. C.; Vardeny, Z. V.; Efros, A. L., Circular dichroism in non-chiral metal halide perovskites. *Nanoscale* **2020,** *12* (35), 18067-18078.

125. Amerling, E.; Baniya, S.; Lafalce, E.; Blair, S.; Vardeny, Z. V.; Whittaker-Brooks, L., Quantifying Exciton Heterogeneities in Mixed-Phase Organometal Halide Multiple Quantum Wells via Stark Spectroscopy Studies. *ACS Applied Materials & Interfaces* **2020,** *12* (47), 52538-52548.

126. Amerling, E.; Baniya, S.; Lafalce, E.; Zhang, C.; Vardeny, Z. V.; Whittaker-Brooks, L., Electroabsorption Spectroscopy Studies of (C4H9NH3)2PbI4 Organic–Inorganic Hybrid Perovskite Multiple Quantum Wells. *The Journal of Physical Chemistry Letters* **2017,** *8* (18), 4557-4564.

127. Kahmann, S.; Tekelenburg, E. K.; Duim, H.; Kamminga, M. E.; Loi, M. A., Extrinsic nature of the broad photoluminescence in lead iodide-based Ruddlesden–Popper perovskites. *Nature Communications* **2020,** *11* (1), 2344.

128. Wang, R.; Hu, S.; Yang, X.; Yan, X.; Li, H.; Sheng, C., Circularly polarized photoluminescence and Hanle effect measurements of spin relaxation in organic–inorganic hybrid perovskite films. *Journal of Materials Chemistry C* **2018,** *6* (12), 2989-2995.

129. Andersson, L. A., Magnetic Circular Dichroism, Theory. In *Encyclopedia of Spectroscopy and Spectrometry (Third Edition)*, Lindon, J. C.; Tranter, G. E.; Koppenaal, D. W., Eds. Academic Press: Oxford, 2017; pp 660-666.

130. Stephens, P. J., Magnetic Circular Dichroism. *Annual Review of Physical Chemistry* **1974,** *25* (1), 201-232.

131. Liu, X.; Chanana, A.; Huynh, U.; Xue, F.; Haney, P.; Blair, S.; Jiang, X.; Vardeny, Z. V., Circular photogalvanic spectroscopy of Rashba splitting in 2D hybrid organic–inorganic perovskite multiple quantum wells. *Nature Communications* **2020,** *11* (1), 323.

132. Manchon, A.; Koo, H. C.; Nitta, J.; Frolov, S. M.; Duine, R. A., New perspectives for Rashba spin–orbit coupling. *Nature Materials* **2015,** *14* (9), 871-882.

133. Yu, S.; Na, G.; Luo, S.; Rubel, O.; Zhang, L., Rashba band splitting in two-dimensional Ruddlesden–Popper halide perovskites. *Journal of Applied Physics* **2020,** *128* (17), 175101.

134. Yu, Z. G., Effective-mass model and magneto-optical properties in hybrid perovskites. *Scientific Reports* **2016,** *6* (1), 28576.

135. Giovanni, D.; Ma, H.; Chua, J.; Grätzel, M.; Ramesh, R.; Mhaisalkar, S.; Mathews, N.; Sum, T. C., Highly Spin-Polarized Carrier Dynamics and Ultralarge Photoinduced Magnetization in CH3NH3PbI3 Perovskite Thin Films. *Nano letters* **2015,** *15* (3), 1553-1558.

136. Odenthal, P.; Talmadge, W.; Gundlach, N.; Wang, R.; Zhang, C.; Sun, D.; Yu, Z.-G.; Valy Vardeny, Z.; Li, Y. S., Spin-polarized exciton quantum beating in hybrid organic–inorganic perovskites. *Nat Phys* **2017,** *13* (9), 894-899.

137. Wang, J.; Lu, H.; Pan, X.; Xu, J.; Liu, H.; Liu, X.; Khanal, D. R.; Toney, M. F.; Beard, M. C.; Vardeny, Z. V., Spin-Dependent Photovoltaic and Photogalvanic Responses of Optoelectronic Devices Based on Chiral Two-Dimensional Hybrid Organic–Inorganic Perovskites. *ACS Nano* **2020**.

138. Trovatello, C.; Katsch, F.; Borys, N. J.; Selig, M.; Yao, K.; Borrego-Varillas, R.; Scotognella, F.; Kriegel, I.; Yan, A.; Zettl, A.; Schuck, P. J.; Knorr, A.; Cerullo, G.; Conte, S. D., The ultrafast onset of exciton formation in 2D semiconductors. *Nature Communications* **2020,** *11* (1), 5277.

139. Zhai, Y.; Baniya, S.; Zhang, C.; Li, J.; Haney, P.; Sheng, C.-X.; Ehrenfreund, E.; Vardeny, Z. V., Giant Rashba splitting in 2D organic-inorganic halide perovskites measured by transient spectroscopies. *Science Advances* **2017,** *3* (7).

140. Rusydi, A.; Chi, X.; Leng, K.; Li, R.; Yu, X.; Yang, P.; Breese, M.; Loh, K. P., Observation of strong helical excitons and unexpectedly giant Rashba splitting in single crystal two-dimensional Organic-Inorganic Halide Perovskites. Research Square: 2020.

141. Urban, J. M.; Chehade, G.; Dyksik, M.; Menahem, M.; Surrente, A.; Trippé-Allard, G.; Maude, D. K.; Garrot, D.; Yaffe, O.; Deleporte, E.; Plochocka, P.; Baranowski, M., Revealing Excitonic Phonon Coupling in (PEA)2(MA)n−1PbnI3n+1 2D Layered Perovskites. *The Journal of Physical Chemistry Letters* **2020,** *11* (15), 5830-5835.

142. Thouin, F.; Valverde-Chávez, D. A.; Quarti, C.; Cortecchia, D.; Bargigia, I.; Beljonne, D.; Petrozza, A.; Silva, C.; Srimath Kandada, A. R., Phonon coherences reveal the polaronic character of excitons in two-dimensional lead halide perovskites. *Nature Materials* **2019,** *18* (4), 349-356.

143. Han, B.; Gao, X.; Lv, J.; Tang, Z., Magnetic Circular Dichroism in Nanomaterials: New Opportunity in Understanding and Modulation of Excitonic and Plasmonic Resonances. *Advanced Materials* **2020,** *32* (41), 1801491.

144. Hofmann, D. M.; Oettinger, K.; Efros, A. L.; Meyer, B. K., Magnetic-circular-dichroism study of heavy- and light-hole g factorsin

${\mathrm{In}}_{\mathrm{x}}$${\mathrm{Ga}}_{1\mathrm{\ensuremath{-}}\mathrm{x}}$As/InP quantum wells. *Physical Review B* **1997,** *55* (15), 9924-9928.

145. Ben-Moshe, A.; Teitelboim, A.; Oron, D.; Markovich, G., Probing the Interaction of Quantum Dots with Chiral Capping Molecules Using Circular Dichroism Spectroscopy. *Nano letters* **2016,** *16* (12), 7467-7473.

146. Chen, T.-P.; Lin, J.-X.; Lin, C.-C.; Lin, C.-Y.; Ke, W.-C.; Wang, D.-Y.; Hsu, H.-S.; Chen, C.-C.; Chen, C.-W., Strong Excitonic Magneto-Optic Effects in Two-Dimensional Organic–Inorganic Hybrid Perovskites. *ACS Applied Materials & Interfaces* **2021,** *13* (8), 10279-10286.

147. Kawamura, Y.; Mashiyama, H.; Hasebe, K., Structural Study on Cubic–Tetragonal Transition of CH3NH3PbI3. *Journal of the Physical Society of Japan* **2002,** *71* (7), 1694-1697.

148. Blöchl, P. E., Projector augmented-wave method. *Physical Review B* **1994,** *50* (24), 17953-17979.

149. Kresse, G. Ab-initio Molekular Dynamik für flüssige Metalle. Wien, 1993.

150. Kresse, G.; Furthmüller, J., Efficiency of ab-initio total energy calculations for metals and semiconductors using a plane-wave basis set. *Computational Materials Science* **1996,** *6* (1), 15-50.

151. Kresse, G.; Furthmüller, J., Efficient iterative schemes for ab initio total-energy calculations using a plane-wave basis set. *Physical Review B* **1996,** *54* (16), 11169-11186.

152. Kresse, G.; Hafner, J., Ab initio molecular dynamics for liquid metals. *Physical Review B* **1993,** *47* (1), 558-561.

153. Perdew, J. P.; Burke, K.; Ernzerhof, M., Generalized Gradient Approximation Made Simple. *Physical Review Letters* **1996,** *77* (18), 3865-3868.

154. Grimme, S., Semiempirical GGA-type density functional constructed with a long-range dispersion correction. *Journal of Computational Chemistry* **2006,** *27* (15), 1787-1799.

155. Huan, T. D.; Tuoc, V. N.; Minh, N. V., Layered structures of organic/inorganic hybrid halide perovskites. *Physical Review B* **2016,** *93* (9), 094105.

156. Berman, P. R., Optical Faraday rotation. *American Journal of Physics* **2010,** *78* (3), 270-276.

157. Miura, N., 2.08 - Magneto-Spectroscopy of Semiconductors. In *Comprehensive Semiconductor Science and Technology*, Bhattacharya, P.; Fornari, R.; Kamimura, H., Eds. Elsevier: Amsterdam, 2011; pp 256-342.

158. Stephen, M. J.; Lidard, A. B., The Faraday effect in semiconductors. *Journal of Physics and Chemistry of Solids* **1959,** *9* (1), 43-47.

159. Crooker, S. A.; Awschalom, D. D.; Baumberg, J. J.; Flack, F.; Samarth, N., Optical spin resonance and transverse spin relaxation in magnetic semiconductor quantum wells. *Physical Review B* **1997,** *56* (12), 7574-7588.

160. Jones, R. C., A New Calculus for the Treatment of Optical SystemsI. Description and Discussion of the Calculus. *J. Opt. Soc. Am.* **1941,** *31* (7), 488-493.

161. Villaverde, A. B.; Donatti, D. A.; Bozinis, D. G., Terbium gallium garnet Verdet constant measurements with pulsed magnetic field. *Journal of Physics C: Solid State Physics* **1978,** *11* (12), L495-L498.

162. Barnes, N. P.; Petway, L. B., Variation of the Verdet constant with temperature of terbium gallium garnet. *J. Opt. Soc. Am. B* **1992,** *9* (10), 1912-1915.

163. Sabatini, R. P.; Liao, C.; Bernardi, S.; Mao, W.; Rahme, M. S.; Widmer-Cooper, A.; Bach, U.; Huang, S.; Ho-Baillie, A. W. Y.; Lakhwani, G., Solution-Processed Faraday Rotators Using Single Crystal Lead Halide Perovskites. *Advanced Science* **2020,** *7* (7), 1902950.

164. Jena, A. K.; Kulkarni, A.; Miyasaka, T., Halide Perovskite Photovoltaics: Background, Status, and Future Prospects. *Chemical Reviews* **2019,** *119* (5), 3036-3103.

165. NREL Efficiency Chart, T. p. i. c. o. t. N. R. E. L., Golden, CO, available online: https://www.nrel.gov/pv/assets/pdfs/best-research-cell-efficiencies.20190802.pdf, accessed on 07 Aug 2019.

166. Pazos-Outón, L. M.; Xiao, T. P.; Yablonovitch, E., Fundamental Efficiency Limit of Lead Iodide Perovskite Solar Cells. *The Journal of Physical Chemistry Letters* **2018,** *9* (7), 1703-1711.

167. Shockley, W.; Queisser, H. J., Detailed Balance Limit of Efficiency of p-n Junction Solar Cells. *Journal of Applied Physics* **1961,** *32* (3), 510-519.

168. Rao, A.; Friend, R. H., Harnessing singlet exciton fission to break the Shockley–Queisser limit. *Nature Reviews Materials* **2017,** *2* (11), 17063.

169. Einzinger, M.; Wu, T.; Kompalla, J. F.; Smith, H. L.; Perkinson, C. F.; Nienhaus, L.; Wieghold, S.; Congreve, D. N.; Kahn, A.; Bawendi, M. G.; Baldo, M. A., Sensitization of silicon by singlet exciton fission in tetracene. *Nature* **2019,** *571* (7763), 90-94.

170. Moffatt, J. E.; Tsiminis, G.; Klantsataya, E.; de Prinse, T. J.; Ottaway, D.; Spooner, N. A., A practical review of shorter than excitation wavelength light emission processes. *Applied Spectroscopy Reviews* **2020,** *55* (4), 327-349.

171. Zhou, J.; Liu, Q.; Feng, W.; Sun, Y.; Li, F., Upconversion Luminescent Materials: Advances and Applications. *Chemical Reviews* **2015,** *115* (1), 395-465.

172. Nienhaus, L.; Correa-Baena, J.-P.; Wieghold, S.; Einzinger, M.; Lin, T.-A.; Shulenberger, K. E.; Klein, N. D.; Wu, M.; Bulović, V.; Buonassisi, T.; Baldo, M. A.; Bawendi, M. G., Triplet-Sensitization by Lead Halide Perovskite Thin Films for Near-Infrared-to-Visible Upconversion. *ACS Energy Letters* **2019,** *4* (4), 888-895.

173. Guo, D.; Ma, L.; Zhou, Z.; Lin, D.; Wang, C.; Zhao, X.; Zhang, F.; Zhang, J.; Nie, Z., Charge transfer dynamics in a singlet fission organic molecule and organometal perovskite bilayer structure. *Journal of Materials Chemistry A* **2020,** *8* (11), 5572-5579.

174. Baluschev, S.; Miteva, T.; Yakutkin, V.; Nelles, G.; Yasuda, A.; Wegner, G., Up-Conversion Fluorescence: Noncoherent Excitation by Sunlight. *Physical Review Letters* **2006,** *97* (14), 143903.

175. Cheng, Y. Y.; Khoury, T.; Clady, R. G. C. R.; Tayebjee, M. J. Y.; Ekins-Daukes, N. J.; Crossley, M. J.; Schmidt, T. W., On the efficiency limit of triplet–triplet annihilation for photochemical upconversion. *Physical Chemistry Chemical Physics* **2010,** *12* (1), 66-71.

176. Park, N.-G., Perovskite solar cells: an emerging photovoltaic technology. *Materials Today* **2015,** *18* (2), 65-72.

177. Roldán-Carmona, C.; Malinkiewicz, O.; Betancur, R.; Longo, G.; Momblona, C.; Jaramillo, F.; Camacho, L.; Bolink, H. J., High efficiency single-junction semitransparent perovskite solar cells. *Energy & Environmental Science* **2014,** *7* (9), 2968-2973.

178. Dong, Q.; Fang, Y.; Shao, Y.; Mulligan, P.; Qiu, J.; Cao, L.; Huang, J., Electron-hole diffusion lengths > 175 μm in solution-grown CH₃NH₃PbI₃ single crystals. *Science* **2015,** *347* (6225), 967-970.

179. Herz, L. M., Charge-Carrier Mobilities in Metal Halide Perovskites: Fundamental Mechanisms and Limits. *ACS Energy Letters* **2017,** *2* (7), 1539-1548.

180. Ehrenfreund, E.; Vardeny, Z. V., Effects of Magnetic Field on Conductance and Electroluminescence in Organic Devices. *Israel Journal of Chemistry* **2012,** *52* (6), 552-562.

181. Ma, L.; Zhang, K.; Kloc, C.; Sun, H.; Michel-Beyerle, M. E.; Gurzadyan, G. G., Singlet fission in rubrene single crystal: direct observation by femtosecond pump–probe spectroscopy. *Physical Chemistry Chemical Physics* **2012,** *14* (23), 8307-8312.

182. Ji, G.; Zheng, G.; Zhao, B.; Song, F.; Zhang, X.; Shen, K.; Yang, Y.; Xiong, Y.; Gao, X.; Cao, L.; Qi, D.-C., Interfacial electronic structures revealed at the rubrene/CH3NH3PbI3 interface. *Physical Chemistry Chemical Physics* **2017,** *19* (9), 6546-6553.

183. Pandey, A. K., Highly efficient spin-conversion effect leading to energy up-converted electroluminescence in singlet fission photovoltaics. *Scientific Reports* **2015,** *5* (1), 7787.

184. Zhu, T.; Yuan, L.; Zhao, Y.; Zhou, M.; Wan, Y.; Mei, J.; Huang, L., Highly mobile charge-transfer excitons in two-dimensional WS₂/tetracene heterostructures. *Science Advances* **2018,** *4* (1), eaao3104.

185. Patterson, A. L., The Scherrer Formula for X-Ray Particle Size Determination. *Physical Review* **1939,** *56* (10), 978-982.

186. Liu, H.; Yan, F.; Li, W.; Lee, C.-S.; Chu, B.; Chen, Y.; Li, X.; Han, L.; Su, Z.; Zhu, J.; Kong, X.; Zhang, L.; Luo, Y., Up-conversion luminescence of crystalline rubrene without any sensitizers. *Organic Electronics* **2010,** *11* (5), 946-950.

187. Leguy, A. M. A.; Azarhoosh, P.; Alonso, M. I.; Campoy-Quiles, M.; Weber, O. J.; Yao, J.; Bryant, D.; Weller, M. T.; Nelson, J.; Walsh, A.; van Schilfgaarde, M.; Barnes, P. R. F., Experimental and theoretical optical properties of methylammonium lead halide perovskites. *Nanoscale* **2016,** *8* (12), 6317-6327.

188. Irkhin, P.; Ryasnyanskiy, A.; Koehler, M.; Biaggio, I., Absorption and photoluminescence spectroscopy of rubrene single crystals. *Physical Review B* **2012,** *86* (8), 085143.

189. Gupta, S.; Adhikari, A.; Mandal, A. K.; Bhattacharyya, K.; Ramamurthy, V., Ultrafast Singlet–Singlet Energy Transfer between an Acceptor Electrostatically Attached to the Walls of an Organic Capsule and the Enclosed Donor. *The Journal of Physical Chemistry C* **2011,** *115* (19), 9593-9600.

190. Zhang, C.; Sun, D.; Sheng, C. X.; Zhai, Y. X.; Mielczarek, K.; Zakhidov, A.; Vardeny, Z. V., Magnetic field effects in hybrid perovskite devices. *Nature Physics* **2015,** *11* (5), 427-434.

191. Merrifield, R. E., Theory of Magnetic Field Effects on the Mutual Annihilation of Triplet Excitons. *The Journal of Chemical Physics* **1968,** *48* (9), 4318-4319.

192. Merrifield, R. E.; Avakian, P.; Groff, R. P., Fission of singlet excitons into pairs of triplet excitons in tetracene crystals. *Chemical Physics Letters* **1969,** *3* (3), 155-157.

193. Tarasov, V. V.; Zoriniants, G. E.; Shushin, A. I.; Triebel, M. M., The role of spin-lattice relaxation in magnetic field effects on the luminescence of amorphous and polycrystalline rubrene films. *Chemical Physics Letters* **1997,** *267* (1), 58-64.

194. Murphy, C. B.; Zhang, Y.; Troxler, T.; Ferry, V.; Martin, J. J.; Jones, W. E., Probing Förster and Dexter Energy-Transfer Mechanisms in Fluorescent Conjugated Polymer Chemosensors. *The Journal of Physical Chemistry B* **2004,** *108* (5), 1537-1543.

195. Desai, P.; Shakya, P.; Kreouzis, T.; Gillin, W. P., Magnetoresistance in organic light-emitting diode structures under illumination. *Physical Review B* **2007,** *76* (23), 235202.

196. Thompson, N. J.; Hontz, E.; Congreve, D. N.; Bahlke, M. E.; Reineke, S.; Van Voorhis, T.; Baldo, M. A., Nanostructured Singlet Fission Photovoltaics Subject to Triplet-Charge Annihilation. *Advanced Materials* **2014,** *26* (9), 1366-1371.

197. Dyakonov, M. I.; Perel, V. I., Current-induced spin orientation of electrons in semiconductors. *Physics Letters A* **1971,** *35* (6), 459-460.

198. D'Yakonov, M. I.; Perel', V. I., Possibility of Orienting Electron Spins with Current. *Soviet Journal of Experimental and Theoretical Physics Letters* **1971,** *13*, 467.

199. Wunderlich, J.; Kaestner, B.; Sinova, J.; Jungwirth, T., Experimental Observation of the Spin-Hall Effect in a Two-Dimensional Spin-Orbit Coupled Semiconductor System. *Physical Review Letters* **2005,** *94* (4), 047204.

200. Dyakonov, M. I. In *Spin Hall Effect*, Proc.SPIE, 2008.